

ABSTRACT

Title of dissertation: MUCIN-MEDIATED AND INTERFERON-DRIVEN
DEFENSE MECHANISMS AGAINST INFLUENZA VIRUS
INFECTION IN HUMAN AIRWAY EPITHELIUM

Ethan Beck Iverson, Doctor of Philosophy 2022

Dissertation directed by: Assistant Professor, Margaret A. Scull,
Department of Cell Biology and Molecular Genetics

The human airway epithelium represents the primary site of infection for many respiratory viruses, including influenza A virus (IAV). To safeguard this tissue and maintain the functionality of the lung, humans possess a two-layer, extracellular, mucus barrier composed predominantly of individual proteins termed mucins. Additionally, underlying epithelial cells produce interferons upon virus detection that promote the establishment of a local antiviral state through autocrine and paracrine signaling. However, despite these protective measures, IAV continues to cause significant annual morbidity and mortality across the globe. Therefore, we sought to further investigate how specific mucin molecules interact with IAV, and how interferon drives intrinsic antiviral defense in the context of a human airway epithelial (HAE) culture system. By utilizing fluorescently-labeled influenza virus particles we further elucidate the adhesive interactions between mucus and influenza virus while also detailing, for the first time, real-time IAV diffusivity within patient-derived mucus samples. These results reveal that the polymeric structure of mucus greatly influences the mobility of IAV within human secreted mucus. Additionally, we investigate the interaction between influenza virus and tethered mucin 1 (MUC1), finding that MUC1 expression is enhanced by virus-driven inflammation and interferon

signaling. Moreover, by establishing a genetically-tractable airway epithelial model, we detail the protective role MUC1 plays in preventing the initial establishment and spread of influenza virus in HAE. Specifically, we find that the loss of MUC1 significantly enhances IAV uptake and spread. Finally, we observe that the directionality of IFN exposure at airway epithelial surfaces impacts the magnitude of protection against IAV and SARS-CoV-2. We then detail the cellular composition of our HAE culture system and define a shared IFN response profile across all HAE component cell types as well as cell type-specific interferon stimulated genes. Together our work provides novel insight into the innate and intrinsic anti-viral properties of the human airway epithelium.

MUCIN-MEDIATED AND INTERFERON-DRIVEN DEFENSE MECHANISMS AGAINST
INFLUENZA VIRUS INFECTION IN HUMAN AIRWAY EPITHELIUM

by

Ethan Beck Iverson

Dissertation submitted to the Faculty of the Graduated School of the
University of Maryland, College Park in partial fulfillment
of the requirements for the degree of Doctor of Philosophy
2022

Advisory Committee:

Assistant Professor Margaret A. Scull, Chair
Professor Jeffrey DeStefano
Professor Xiaoping Zhu
Assistant Professor Gregg A. Duncan
Senior Investigator Kim Green

© Copyright by
Ethan Iverson
2022

Dedication

This dissertation is dedicated to my parents, Pat and Judy, my wife, Stephanie, and my advisor, Dr. Margaret Scull. All of you have stood by my side and helped me grow, often with excessive patience. I cannot express my gratitude to you all enough.

Acknowledgements

I would like to thank all the current and former members of the Scull lab, especially Kira, Monty, Talita, Eva, and Maxinne. I also want to welcome the next generation of Scull lab members: Jeff and Maria. I hope that your time in this lab is as rich and rewarding for you as it was for me. I would also like to give special acknowledgement to the Duncan lab, and particularly Daniel Song. Together, Scull Island and Greggland are an unstoppable force of mucus research.

I would also like to thank the members of my dissertation committee, namely Dr. Jeffery DeStefano, Dr. Gregg Duncan, Dr. Kim Green, and Dr. Xiaoping Zhu. Thank you for helping me navigate this process and for all your guidance.

I would also like to thank the sources of funding which has made this research possible: R01 HL151840 awarded to Dr. Margaret A. Scull; R21 AI149180 awarded to Drs. Margaret A. Scull and Brad R. Rosenberg; R21 AI142050 awarded to Drs. Margaret A. Scull and Gregg A. Duncan; and the NIH Institutional Training Grant T32 AI125186A.

Table of Contents

Dedication	ii
Acknowledgements	iii
Table of Contents	iv
List of Tables	viii
List of Figures.....	ix
List of Abbreviation	x
Chapter 1 : Introduction	1
1.1 Respiratory Tract Structure and Function.....	1
1.2 Cell Types of the Respiratory Epithelium.....	3
1.3 Innate Defenses of the Respiratory Tract.....	4
1.3.1 Secreted Mucins.....	6
1.3.2 Tethered Mucins.....	7
1.3.3 Mucociliary Clearance	9
1.3.4 Antiviral Responses of the Respiratory Tract.....	10
1.4 An In Vitro Model of Human Airway Epithelium at Air-Liquid Interface.....	12
1.5 Influenza Virus Biology.....	14
1.5.1 Classification	14
1.5.2 Clinical Relevance and Impact.....	15
1.5.3 Viral Tropism	16
1.5.4 Virion Structure.....	17
1.6 Influenza A Virus Life Cycle	18
1.6.1 Attachment and Entry	18
1.6.2 Early Infection Activities.....	20
1.6.3 Particle Assembly and Egress	21
Chapter 2 : Materials and Methods.....	23
2.1 Chapter 3: Diffusion and Interactions of Influenza Virus with Secreted Mucus	23
2.1.1 Immortalized Cell Culture	23
2.1.2 Influenza Virus Rescue.....	23
2.1.3 Viral Titration by Plaque Assay	24
2.1.4 Influenza Virus Labeling and Nanoparticle Preparation.....	25
2.1.5 Neuraminidase Assay.....	25
2.1.6 Human Mucus Collection.....	26
2.1.7 Synthetic Mucus Hydrogel Preparation.....	27

2.1.8 Fluorescence Video Microscopy	27
2.1.9 Multiple Particle Tracking (MPT) Analysis	28
2.1.10 Statistics and Reproducibility	29
2.2 Chapter 4: Membrane-Tethered Mucin 1 is Stimulated by Interferon and Virus Infection in Multiple Cell Types and Inhibits Influenza A Virus Infection in Human Airway Epithelium	29
2.2.1 Immortalized Cell Culture	29
2.2.2 Primary Human Macrophage Cultures	30
2.2.3 Human Airway Epithelial Cells	30
2.2.4 Influenza Viruses and Mutant Cloning	31
2.2.5 Influenza Virus Rescue and Sucrose Gradient Purification	32
2.2.6 Influenza Virus Biotinylation	33
2.2.7 Plaque Assay	34
2.2.8 Influenza Virus Infection of Human Airway Epithelium	34
2.2.9 Unwashed HAE Infection Timecourse	34
2.2.10 Influenza Virus Kinetic Entry Assay	35
2.2.11 Culture Stimulation Experiments	35
2.2.12 HAE Culture Histology and Immunohistochemistry Preparations	36
2.2.13 <i>En Face</i> Immunofluorescent Staining of HAE Cultures	37
2.2.14 Primary and Secondary Antibodies	37
2.2.15 MUC1 Immunoprecipitation	39
2.2.16 MUC1 ELISA	40
2.2.17 RT-qPCR	41
2.2.18 Western Blot	42
2.2.19 Transmission Electron Microscopy and Immunostaining	43
2.2.20 CRISPR gRNA Design	44
2.2.21 Lentiviral Transduction	45
2.2.22 Mutagenesis Assay and Sequencing	46
2.2.23 Software Used and Statistical Analysis	46
2.3 Chapter 5: Interferon Responses in HAE and Impact on Viral Infection Dynamics	47
2.3.1 Immortalized Cell Culture	47
2.3.2 Influenza and SARS-CoV-2 Viruses Used	47
2.3.3 Viral Titration by Plaque Assay	48
2.3.4 Human Airway Epithelial Cells	49

2.3.5 Infection of Human Airway Epithelium	49
2.3.6 HAE Culture Histology and Immunohistochemistry Preparations	50
2.3.7 <i>En Face</i> Immunofluorescent Staining of HAE Cultures	51
2.3.8 Flow Cytometry.....	51
2.3.9 Primary and Secondary Antibodies.....	51
2.3.10 IFN β and IFN λ 1/ λ 3 ELISA	53
2.3.11 Dextran Permeability Assay	54
2.3.12 Culture Stimulation Experiments.....	54
2.3.13 Dissociation of HAE for Single-Cell RNA Sequencing.....	55
2.3.14 Data Processing	55
2.3.15 Cluster Annotation	57
Chapter 3 : Diffusion and Interactions of Influenza Virus with Secreted Mucus.....	58
3.1.1 Abstract	59
3.1.2 Introduction.....	59
3.1.3 Fluorescent Labeling and Tracking of IAV in Human Mucus Samples	61
3.1.4 Effect of Neuraminidase Inhibition on IAV Diffusion Through Human Mucus	64
3.1.5 Impact of Cross-linking on IAV Diffusion in Human and Synthetic Mucus	65
3.1.6 Impact of Mucus Composition on IAV Diffusion and Establishing a Synthetic Mucus Array	68
3.1.7 Discussion	69
Chapter 4 : Membrane-Tethered Mucin 1 is Stimulated by Interferon and Virus Infection in Multiple Cell Types and Inhibits Influenza A Virus Infection in Human Airway Epithelium	73
4.1.1 Abstract	74
4.1.2 Introduction.....	75
4.1.3 The IAV Hemagglutinin Protein Binds MUC1 Isolated from HAE Apical Secretions and Co-Localizes with MUC1 During Infection	77
4.1.4 IAV Replication in HAE is Not Associated with an Increase in Soluble MUC181	77
4.1.5 Cell-Associated MUC1 Levels are Upregulated During IAV Infection and After Interferon Treatment.....	82
4.1.6 Soluble Factors Secreted by HAE During IAV Infection Upregulate MUC1 on Primary Human Monocyte-Derived Macrophages	87
4.1.7 Generation of HAE Cultures Lacking MUC1	88
4.1.8 IAV Challenge in HAE Lacking MUC1 Reveals Altered Infection Dynamics...	90
4.1.9 Discussion	94
Chapter 5 : Interferon Responses in HAE and Impact on Viral Infection Dynamics.....	100

5.1.1 Abstract	101
5.1.2 Introduction.....	102
5.1.3 Polarization of IFN Secretion and IFN Receptor Distribution in HAE.....	105
5.1.4 Apical and Basolateral Application of Type I and Type III IFN is Protective Against IAV and SARS2	106
5.1.5 HAE Is Composed of Diverse Cell Types Consistent with Airway Epithelium <i>In Vivo</i>	109
5.1.6 Differences in the Magnitude of the ISG Response in Apical vs. Basolateral Stimulation are More Pronounced for IFN β than IFN λ	111
5.1.7 The HAE IFN Response Induces a Shared ISG Program and Cell Type- specific ISGs	113
5.1.8 Cell Type-specificity of CD38 and CXCL10 is Retained on the Protein Level in the Context of Both Apical and Basolateral IFN Stimulation and During Infection .	116
5.1.9 Discussion	119
Chapter 6 : Conclusion	121
Chapter 7 : Appendices	127
References	138

List of Tables

Table 2.1: Primary, Secondary, and Isotype Antibody Probes Used in Chapter 4.

Table 2.2: RT-qPCR Target Primers from Chapter 4.

Table 2.3: Primary, Secondary, and Isotype Antibody Probes Used in Chapter 5.

List of Figures

- Figure 1.1.** The Human Respiratory Tree
Figure 1.2. The Two-Layer Mucin Barrier
Figure 1.3. HAE Cultures at Air-Liquid Interface
Figure 1.4. Structure of the Influenza A Virus
Figure 1.5. Influenza A Virus Replication and Coding Schematic
Figure 3.1. Fluorescent Labeling and Tracking of IAV in Mucus
Figure 3.2. Impact of Neuraminidase Inhibition on IAV Diffusivity
Figure 3.3. Disruption of Mucus Microstructure Enhances IAV Diffusivity
Figure 3.4. Investigation of Mucus Composition on IAV Diffusivity with a Synthetic Mucus Array
Figure 4.1. IAV Hemagglutinin and IAV Bind HAE-Derived MUC1 and Co-localize During Infection
Figure 4.2. IAV Replication in HAE is not Associated with an Increase in Soluble MUC1
Figure 4.3. Cell-associated MUC1 Levels are Upregulated During IAV Infection and Interferon Treatment
Figure 4.4. Type I IFN and IAV Broadly Upregulate MUC1 Expression Across HAE
Figure 4.5. Primary Human Monocyte-Derived Macrophages Upregulate MUC1 in Response to IFN and Soluble Factors Produced From IAV-infected HAE
Figure 4.6. Establishment and Characterization of Immortalized HAE Depleted for MUC1
Figure 4.7. Infection in HAE Lacking MUC1 with Multiple IAV Strains Reveals Enhanced Viral Spread
Figure 4.8. HAE Lacking MUC1 Exhibit Rapid IAV Uptake
Figure 5.1. HAE are Permissive to IAV and Exhibit Asymmetrical IFN Receptor Expression and IFN Secretion
Figure 5.2. IFN Stimulation of HAE from Apical and Basolateral Sources is Protective Against IAV and SARS-CoV-2
Figure 5.3. The Cellular Composition Profile of HAE
Figure 5.4. The Basolateral Application of Type I IFN Induces Stronger ISG Expression in Four HAE Cell Types
Figure 5.5. The Significance of ISG Upregulation Following Basolateral Type I IFN Exposure and Cell-Type Specific ISG Expression
Figure 5.6. CXCL10 and CD38 Protein Expression Matches Transcriptomic Data and SARS-CoV-2 Induces CD38 Expression in Ciliated Cells

List of Abbreviation

CBF	Cilia beat frequency
CO ₂	Carbon dioxide
CT	Cytoplasmic tail
DAMP	Damage-associated molecular patterns
ED	Extracellular domain
IAV	Influenza A virus
HA	Hemagglutinin
HAE	Human airway epithelium
HE	Hemagglutinin esterase
IFN	Interferon
ILI	Influenza-like illness
ISG	Interferon-stimulated gene
M1	Matrix protein 1
M2	Matrix protein 2
MCC	Mucociliary clearance
N	Nucleocapsid (SARS-CoV-2)
NA	Neuraminidase
NAI	Neuraminidase inhibitor

NLR	NOD-like receptor
NP	Nucleocapsid protein (influenza virus)
O ₂	Oxygen
PAMP	Pathogen-associated molecular pattern
PCL	Periciliary layer
PS-NP	Polystyrene nanoparticle
RLR	RIG-I-like receptor
SARS-CoV-2	Severe acute respiratory syndrome coronavirus 2
TLR	Toll-like receptor
TNF α	Tumor necrosis factor α
vRNA	Viral RNA
vRNP	Viral ribonucleoprotein

Chapter 1 : Introduction

This chapter features adaptations from a published article [1] which is licensed under a Creative Commons Attribution 4.0 International License. The images or other third-party material in this article are included in the article's Creative Commons license, unless indicated otherwise in a credit line to the material. To view a copy of this license, visit <http://creativecommons.org/licenses/by/4.0/>.

1.1 Respiratory Tract Structure and Function

Owing to the high metabolic demand of multicellular eukaryotic organisms, oxidative phosphorylation is a fundamental requirement for human life [2,3]. Unlike carbon metabolic substrates, oxygen (in the form of O_2) cannot be efficiently stored; thus, the respiratory system must provide constant access to oxygen proportional to its instantaneous needs [2]. In humans, inhalation begins with gas transport through the nasal cavity. Here, the nasal turbinates create airflow vortices which cause inhaled particulate to impact the mucosa, reducing particulate deposition in the more sensitive lower airways [4]. Air is subsequently piped through the first and largest of the conducting airways, the trachea [2,5] (**Fig. 1.1**). Bifurcation of the trachea yields two main bronchi, each of which leads to the separate lobes of the lung and ultimately, to the acinar airways. Both the conducting and acinar airways undergo regular, patterned branching which is characterized by further airway narrowing as well as an exponentially increasing airway surface area [2,5–7]. The beginning of the acinar airways increasingly terminates into the fundamental sites of gas exchange: the alveoli [2,5]. Inhaled O_2 must diffuse into the

alveolar spaces and eventually the bloodstream, where it is scavenged by hemoglobin and systemically transported as needed [2,5]. The result is a dynamically flexible organ extensively perfused with blood through direct circulatory contact and a massive surface area of epithelium that is in constant environmental contact.

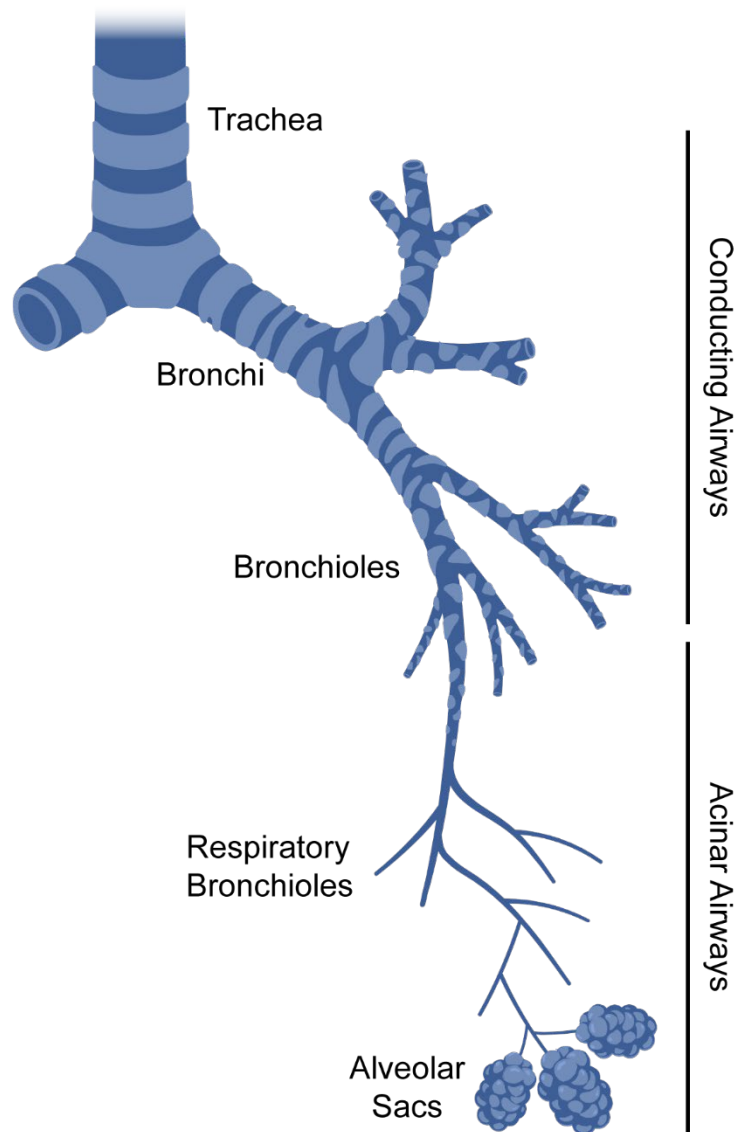


Figure 1.1. The Human Respiratory Tree. Cutaway diagram of the human respiratory tree with the airway labeled by morphological breakpoints. Created with BioRender.com.

1.2 Cell Types of the Respiratory Epithelium

The hierarchy of the human airway epithelium (HAE) begins with basal cells which are the ultimate progenitors for the superficial pseudostratified epithelial cells [8,9]. Basal cells are more abundant in the upper airways and trachea, becoming rarer in the distal regions of the lung. Upon detection of epithelial damage, basal cells rapidly migrate to sites of damage to maintain the barrier functionality of the epithelium [8,9]. Additionally, basal cells adopt a faster replicative phenotype by differentiation into intermediate basal cells. These intermediate or parabasal cells can directly differentiate into rare cell components of the respiratory epithelium as well as club cells [9]. Like basal cells, club cells also possess multipotent differentiation potential which are capable of self-renewal and differentiation into goblet (discussed in section 1.3.1) and ciliated cells (discussed in section 1.3.3). Together, club, goblet, and ciliated cells comprise the large majority of the pseudostratified epithelium of HAE [8,10]. Unlike goblet and ciliated cells, however, club cells are mainly present in the terminal bronchioles and are essentially absent in the proximal airways [11]. As the primary non-mucous secretory cells, club cells secrete the major components of the distal airway surface liquid, including surfactants [12] to help regulate airway hydration. They also aid in maintenance of a quiescent, non-inflammatory state among the HAE by secretion of SCGB1A1 (i.e. CCSP and CC10) liquid [9,13] and the processing of toxic inhaled xenobiotic compounds [11]. However, to ensure proper air-surface liquid balance and hydration in both proximal and distal airways, ionocytes are critical to maintaining proper luminal ion balance [47]. Ionocytes are a recently discovered cell type and are a rare component of the superficial HAE, deriving directly from parabasal cells [8]. Together these cell types enable for the proper function, protection, and regeneration of the HAE.

1.3 Innate Defenses of the Respiratory Tract

In humans the respiratory process involves inhaling over 10,000 liters of air containing an estimated minimum of 5×10^{10} particles in a single day [4]. Thus, mechanisms to protect the underlying epithelium from offensive environmental particulate and pathogens and clear inhaled material are essential to preserve lung function. One such mechanism is the formation of a two-layer, extracellular physical and chemical mucosal barrier consisting of a secreted mucus gel and underlying periciliary layer (PCL) [4,14,15] (**Fig. 1.2**).

In the upper airways, where impaction by larger particulate is more common and the surface area of the respiratory tract is minimal [2,4], the secreted mucus layer is relatively thick. Further down the respiratory tree, the estimated thickness of the secreted mucus raft progressively decreases concomitantly with the decreased abundance and size of secretory glands [4,16]. Underneath this secreted mucus raft, the PCL is formed by the protrusion of cilia from ciliated cells into the airway luminal space [14,17,18]. Originally assumed to be a thin and watery layer because of artefactual imaging techniques, it is now understood that the PCL glycocalyx is very dense [14]. This dense glycocalyx is itself protective of the underlying epithelium as it can sterically exclude particles as small as 40 nm [14,15,19] with the microvilli further blocking penetration of particles as small as 18 nm [15]. Importantly, both the secreted mucus gel and PCL are composed, in large part, of individual glycoproteins termed mucins which are either released into the airway from dedicated secretory cells or tethered to the cell surface, respectively [17,20]. Despite the unifying presence of mucin-like domains, mucins possess unique domains and expression profiles which allow for non-redundant functionality and localization critical to the respiratory mucosa.

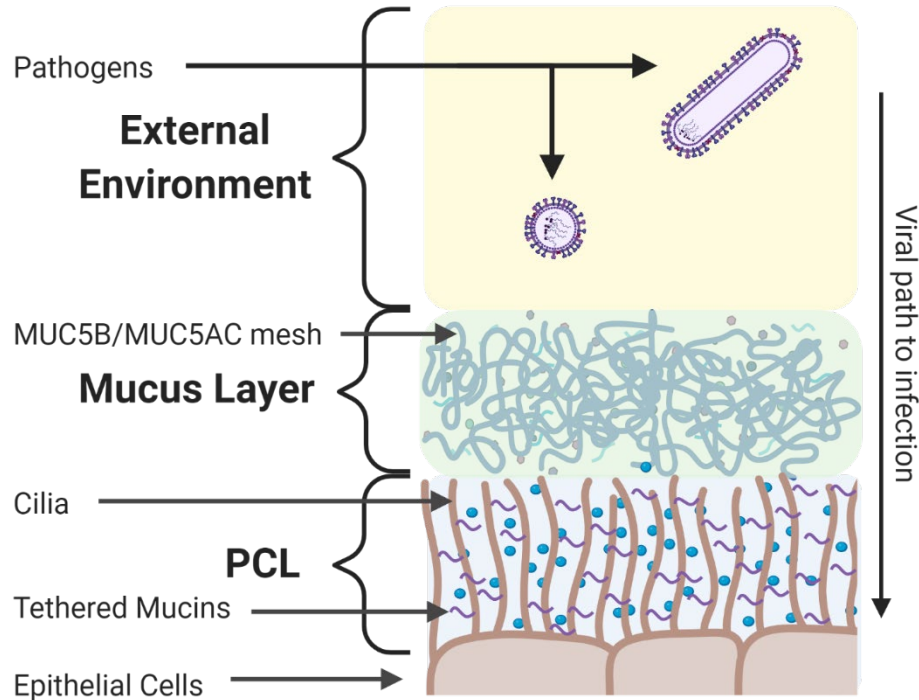


Figure 1.2. The Two-Layer Mucin Barrier. Cross-sectional view of the airway lumen with indicated features of the air-surface liquid. Once in the airway lumen, incoming pathogens (indicated here by influenza virus) must traverse the mucus layer gel (green) before accessing the periciliary layer (light blue). Modified from [1]. Created with BioRender.com.

1.3.1 Secreted Mucins

The major secreted mucins of the respiratory tract are MUC5B and MUC5AC which together comprise roughly 90% of all mucins within the secreted mucin layer [17]. Other secreted mucins make up a minority of total secretions and play uncertain roles, such as MUC7 which, in contrast to MUC5B and MUC5AC, does not polymerize [20].

Secreted mucins are predominantly released by submucosal secretory glands located within the sinuses, nasal passage, and trachea [4,16]. Submucosal gland secretions are primarily composed of MUC5B in contrast to superficial epithelial goblet and club cell secretions which contain both MUC5B and MUC5AC [4,16,21] with an increasing relative abundance of MUC5AC in the more distal airways [16,21]. Outside of

submucosal glands, goblet cells are mostly restricted to the larger conducting airways and secrete a mix of both MUC5B and MUC5AC [20,22]. Additionally, in contrast to MUC5B, expression of MUC5AC is highly modulated by inflammatory and mechanical stimuli [23–25].

Mucins are released via exocytosis and subsequent formation of the mucus gel is reliant on proper luminal biochemistry and polymeric interactions. MUC5B, for instance, forms intracellular granules through multimeric N- and C-terminal interactions which densely pack these bulky molecules prior to exocytosis [21,26]. Upon release, the ionic composition of the airway lumen leads to unpackaging and multimeric linearization [26–28] which can also be viewed as “plumes” protruding from the epithelium [15]. Additionally, MUC5B and MUC5AC possess cysteine rich domains which leads to their extensive cross-linking and the formation of a porous mucin gel [21,27,29,30]. The porous nature of the secreted mucin gel contributes to its ability to protect the underlying epithelium through pathogen entrapment by size exclusion and other adhesive interactions [29–31], while MUC5B and MUC5AC content can impact the viscoelastic properties of the resultant mucus gel.

1.3.2 Tethered Mucins

Transmembrane-anchored or ‘tethered’ mucins decorate the epithelial cell apical surface and, as such, provide a platform on which the secreted mucin raft can rest and interact with cilia [14,15,17,19].

The most abundant tethered mucins in the human airway are MUC1, MUC4, MUC16, and to a lesser extent MUC20; however, other tethered mucins are also present with poorly understood functions [15,17,20]. The expression of these tethered mucins

varies according to location within the respiratory tract and cell type [17]. MUC1 expression levels, for example, are higher in the bronchiolar epithelium relative to the main bronchus or trachea [17] but can also be found in some submucosal gland cells [15]. MUC4 predominates in the nasal passage and larger conducting airways, including the main bronchi [10,17], but is absent from submucosal glands [15]. In tracheal-derived HAE cultures, MUC1 and MUC4, are both highly expressed on ciliated cells. However, MUC1 localizes preferentially to the microvilli while MUC4 can be found on ciliary shafts [15,17]. By contrast, MUC16 expression is restricted to goblet cells and may be secreted along with MUC5B [15].

While principally cell-associated, the extracellular domain (ED) of these mucins can be shed into the airway through autocatalytic and proteolytic-targeted cleavage domains upstream of their transmembrane domains [15,17,32]. Despite the presence of such cleavage domains, these tethered mucins likely require enzymatic dissociation or undefined mechanisms to fully liberate the extracellular domain from the transmembrane domains [17,32–35]. Nonetheless, MUC1, MUC4, and MUC16 have been shown to comprise a minor (~10%), but significant, fraction of total mucin content of sputum [17] though they are not known to be gel-forming.

In addition to the bulky ED typical of tethered mucins, MUC1, MUC4, and MUC16 all feature a cytoplasmic tail (CT); the CT of each individual mucin is highly conserved, but variation in CT length and sequence between mucins suggests unique functions [17,36]. MUC1 features the largest CT which also has the most well-described phosphorylation profile and interaction partners involved in signal transduction [17,37,38]. However, the CT of all three mucins can translocate to the nucleus [39–43], altogether supporting important functions outside its canonical representation among the PCL.

1.3.3 Mucociliary Clearance

As noted above, polymerization of secreted mucins forms a mucin gel or “raft” above the epithelium of the conducting airways in which inhaled particulate is embedded and trapped [4,14,44]. Even if the vast majority of this particulate was inert and subsequently exhaled, particulate cannot be allowed to accumulate indefinitely. Thus, to maintain the health and functionality of the airways the active removal of embedded particulate is critical.

Clearance of embedded particulate within the respiratory mucosa is achieved through successive power and recovery strokes of cilia that penetrate slightly into the overlying secreted mucin layer. This phenomenon of mucociliary clearance (MCC) [20,45,46] moves the secreted mucin raft (roughly 40-70 $\mu\text{m} / \text{s}$) [47–49] along with any embedded particulate from the lower lung towards the esophagus and ultimately towards neutralization in the stomach [14,18,50]. Both the cilia beat frequency (CBF) and the structural properties of the secreted mucin gel are primary factors dictating MCC rate [51]. The mucus raft exhibits both fluid-like (i.e., viscous modulus) and solid-like (i.e., elastic modulus) behavior, a combination referred to as viscoelasticity. The viscoelastic properties of the mucus gel vary based on the content of MUC5B and MUC5AC [52,53], as epitomized in airway dysfunction such as asthma, COPD, and cystic fibrosis [28,44,52,54]. Therefore the relative abundance of MUC5AC [16,44,52] may be critical for the modulation of steady-state MCC as well as during stressful conditions where MUC5AC expression is increased. Importantly, the ability for this gel to be deformed yet recover its shape in combination with the patterned and coordinated ciliary action allows for very rapid and efficient transport by ciliary action [51,55,56]. In addition to the secreted mucin raft, the PCL fluid is also transported by ciliary action at roughly the same rate [46,48], though this might rely on the existence of a mucin raft to transport [57]. Additionally, some tethered

mucins have domains capable of interacting with the gel-forming mucins, lending credence to the idea that this facilitates MCC in some way [17,58].

The two-mucin barrier system which gives rise to MCC relies on the functional differences between secreted and tethered mucins. However, both classes of mucins possess a tandem repeat domain rich in serine and threonine, allowing for extensive O-linked glycosylation [17,20,27]. Indeed, such extensive glycosylation leads to steric constraints that impart a simple rod-like (i.e. “pipe-cleaner” conformation) structure and can contribute to as much as 50-90% of the overall molecular weight of the mucin [17]. This glycosylation also contributes to the highly hydrophilic nature of mucins, as well as to the lubrication properties which facilitate MCC even with extensive contact between the two mucin layers [4].

1.3.4 Antiviral Responses of the Respiratory Tract

Despite this robust extracellular mucosal barrier, pathogens do still manage to access the airway epithelium. Importantly, these cells can directly sense pathogen-associated molecular patterns (PAMPs) through pattern recognition receptors (PRRs) such as Toll-like receptors (TLRs), RIG-I like receptors (RLRs), and NOD-like receptors (NLRs) [59]. In viral contexts, PAMPs include viral glycoproteins, cytosolic DNA, endosomal RNA, and various RNA species associated with intermediate replication products [59–61]. Moreover, responses to pathogenic insult can also be greatly affected by coincident detection of damage-associated molecular patterns (DAMPs) which represent host cell components that directly indicate tissue or cell death [60,62,63].

The ultimate consequence of PAMP or DAMP detection is the activation of two primary signal cascades axes leading to the production of both inflammatory cytokines

and interferons (IFN) [60,61]. These soluble mediators are secreted to prime immune cells for eventual recruitment to the site of infection and simultaneously blunt epithelial permissivity to viral infection, respectively [59]. Interferon acts as both an autocrine and paracrine signal and dissemination of IFN as well as other cytokines throughout the local microenvironment is greatly influenced by interactions with neighboring cells and the extracellular matrix [61].

Three classes of IFNs have been described that utilize different heterodimeric receptors to trigger activation of JAK/STAT signaling pathway components. Type I (e.g. IFN α and IFN β) and type III interferons (i.e. IFN λ) have well-described impacts on viral replication mediated through the induction of hundreds of interferon stimulated genes (ISGs) including many direct anti-viral effector proteins [64]. Importantly, IFN-induced signaling also amplifies IFN expression in a positive feedback loop which (at least initially) serves to reinforce the antiviral response [64,65]. While nearly all cells in the human body are capable of a type I IFN response [64], the epithelium of the respiratory tract can also secrete and respond to type III IFN [66]. Type I and type III IFN responses have been shown to play an important role during respiratory viral infection [64,65] and efforts have been made to understand the unique contribution of type I vs type III IFN to infection. Notably, type I IFN and type III IFN have different induction kinetics [66–68] and downstream ISG upregulation [65–67]. Other ISGs upregulated by type I and III IFN are various chemokines, cytokines, and inflammatory markers [64,68].

1.4 An In Vitro Model of Human Airway Epithelium at Air-Liquid Interface

The lung is a complex and dynamic tissue characterized by different anatomical zones comprising different cell types, a temperature gradient, and the continuous forces exerted by mechanical clearance mechanisms and tidal breathing. As a mucosal tissue, the airway epithelium also evolved a physical and chemical extracellular barrier that promotes normal tissue homeostasis and neutralizes pathogens. While immortalized cell lines have historically been the workhorse of viral research, they lack critical aspects of the airway microenvironment at both the cellular and extracellular level. While no model system is perfect, Transwell cultures of airway epithelium at air–liquid interface (ALI) represents a powerful tractable system to dissect the mechanisms of infection in a near-native context (**Fig. 1.3**).

Transwell culturing systems maintained at ALI with proper differentiation media allow for pseudostratified epithelial growth and formation of a mucosal barrier [8,15,69,70]. Transwell systems traditionally utilize cells derived from normal tissue samples including adult basal stem cells (i.e., primary cells) [71–76] and more recently, human pluripotent stem cells (hPSC) [77–80]. Primary cells can be acquired directly through epithelial brushing or tissue digestion from human and animal model sources, after which cell suspensions can be frozen down for future use or, like hPSC, expanded in normal 2D cell culture format [71–76]. Basal progenitor cells are then transferred to extracellular matrix-coated Transwell membranes and maintained in submerged conditions until the cells reach confluence. Finally, media is removed from the apical chamber to begin the differentiation process into a polarized epithelium over several weeks (**Fig. 1.3**).

Importantly, ALI cultures have been shown to recapitulate the morphology and physiology of the upper conducting airways of the normal human respiratory epithelium, including rare cell populations found *in vivo* [8,15,69,70]. Notably, *in vitro* HAE cultures

are frequently observed to have lower CBF (~4-6 Hz) [52,81,82] though some do better recapitulate the higher values observed *in vivo* [83,84]. Additionally, as models of airway disease, they can recapitulate major clinical features of cystic fibrosis (CF) [28,85–88], asthma [89–93], and chronic obstructive pulmonary disease (COPD) [90,94,95].

One limitation of primary cell-derived ALI cultures is that differentiation capacity of these cells is lost progressively upon expansion in traditional 2D cell culture settings. Fresh primary cells must be acquired, and cell stocks from individual donors bought commercially can be exhausted. Despite this, media supplemented with a Rho-kinase inhibitor can enhance cell proliferation and viability prior to differentiation [96,97]. These systems are not only cost-saving, but allow a larger window for genetic manipulation, selection, and cryopreservation of larger stocks. The establishment of an immortalized basal cell line (termed BSCi-NS1.1 cells) which is capable of differentiation up to passage thirty has extended this limit even further [98]. Primary cell-derived ALI cultures have proven to be genetically tractable systems for knockdown (e.g., shRNA) or knockout (e.g., CRISPR/Cas9 targeting) of desired genes with [99,100] or without [101] extending cellular differentiation capacity limits.

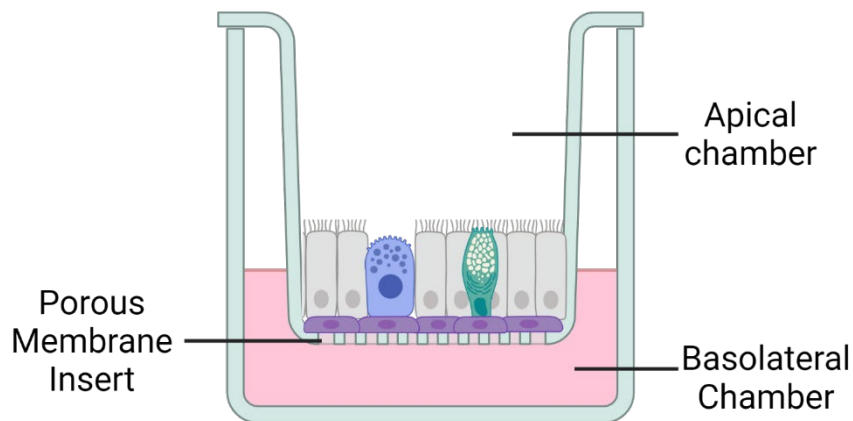


Figure 1.3. HAE Cultures at Air-Liquid Interface. Mature HAE grown at ALI for 4-6 weeks. Transwell inserts have porous membrane allowing for nutrient uptake from the basolateral chamber, where the insert is housed. The apical compartment of the Transwell, assuming robust cell-cell contacts, remains open to the air once the differentiation stage has been achieved (post-airlift). Created with BioRender.com

1.5 Influenza Virus Biology

1.5.1 Classification

Influenza viruses belong to the family *Orthomyxoviridae* [102]. Within this family are the mammalian-infecting genres of *Alphainfluenzavirus*, *Betainfluenzavirus*, *Gammainfluenzavirus*, and *Deltainfluenzavirus* where each contains the archetypal type A through type D influenza virus species [102]. Additionally, the *Orthomyxoviridae* also includes the genres *Isavirus*, *Quaranjavirus*, and *Thogotovirus* whose lesser-studied members infect the respiratory tissue of amphibians and fish [103,104], thus supporting the existence of an evolutionary conserved and ancient group of vertebrate-infecting viruses [103].

The influenza virus genome is composed of single-stranded RNA which is complementary to a translatable product (i.e. “negative” stranded) [105–108], and as such is a Class V member of the Baltimore classification scheme [109]. Additionally, the

genome is comprised of either seven (i.e. type C and D influenza viruses) or eight segments (i.e. type A and B influenza viruses) depending on the coding strategy [103,107].

1.5.2 Clinical Relevance and Impact

Influenza viruses type A (IAV), B, and C infect humans regularly [110–115], resulting in a high seasonal morbidity and mortality for types A and B in particular [115–117]. In the US, this amounts to an average of about 22,000-25,000 deaths annually [118]; however, in the 2017-2018 season this was estimated to be double this seasonal average at 52,000 [119]. Globally, estimates for influenza virus mortality range from 291,000-645,000 with significant variation season-to-season [117]. In addition to seasonal epidemics, influenza A virus is known to cause sporadic pandemics, with evidence of it having caused six of the last seven respiratory virus pandemics [120–125].

Mortality estimates for influenza in the intervening pandemic waves have always exceeded subsequent years for the homotypic circulating strain [126], though these are sometimes mild overall [127,128]. The most devastating of influenza virus pandemics being the 1918 pandemic with an estimated number of US deaths being in excess of 1.2 million [129] and global mortality estimates ranging from 21.5 million to 50 million [130]. By comparison, the first-year impact on all-cause death incidence rate in New York City of the 1918 pandemic wave rivals that of the 2019 SARS-CoV-2 pandemic wave of 2020 [131] and greatly exceeds disease-adjusted life-years lost [129].

The primary clinical course of disease for both type A and B influenza viruses is similar and characterized by the classic rapid onset of fever, coryza, cough, headache, malaise, and respiratory tract inflammation [132]. Notably, influenza-like illness (ILI) can be caused by a diverse array of both bacterial and (more prominently) viral agents, though

ILI and especially medically-attended ILI is predominantly caused by type A and B influenza viruses [132–135]. Influenza C is also capable of causing seasonal epidemics; however, it is not thought to be as clinically relevant or seasonally abundant [113,136] and rare cases of severe disease are mostly restricted to children [113,137]. Additionally, bacterial superinfection and subsequent (or concurrent) pneumonia represents an intrinsic pathology of influenza virus infection which most influenza-associated deaths are associated with [138–141]; however, the relationship between influenza and pneumonia is complex and varied depending on pandemic or epidemic strain characteristics as well as host co-morbidities [138,142–144].

1.5.3 Viral Tropism

The host diversity among type A influenza virus is significant and includes avian, swine, equine, mustilid, canine, and feline hosts [120,121,145–151]. Notably, epizootic and zoonotic spillovers are common, leading to interspecies diversity flux [152–154], particularly with respect to wild waterfowl migratory patterns [154].

In all of these species, as in humans, influenza viruses target the respiratory epithelium with the notable exception of avian viruses which target the gastrointestinal epithelium [103]. Influenza type A and B utilize the surface glycoprotein hemagglutinin (HA) to mediate interactions with sialic acid-linked glycan moieties on surface-expressed host proteins to facilitate endosomal uptake [155–158]. In addition, the neuraminidase (NA) glycoprotein facilitates destruction of the receptor moiety to both ensure the productive release of nascent budding virions as well as destroy non-productive or decoy attachment sites [115,159,160]. Together, the receptor binding and destroying activities represent critical influences on both host species tropism as well as host cell tropism [161–165].

1.5.4 Virion Structure

Influenza A virus (**Fig. 1.4A**) possesses a membrane envelope studded with protruding glycoproteins HA and NA [166–168] as well as the viroporin matrix protein 2 (M2) [169]. While it is well characterized that influenza A virions adopt an “ovoid” or “spherical” shape in addition to longer filamentous forms [168,170–172], influenza B and C also exhibit similar particle pleomorphism [173,174].

Internal to the influenza A virus envelope is a layer of matrix protein 1 (M1) in contact with the membrane envelope and cytoplasmic domains of the glycoproteins [175–179]. Interactions between M2 and M1 facilitate recruitment of the nucleocapsid protein (NP) [179–182] which decorates internal stretches of the genomic viral RNA (vRNA). The terminal ends of the vRNA are bound by the heterotrimeric replicase complex, composed of the polymerase subunits PB1, PB2, and PA [183], which, together with NP-studded vRNA, comprise the viral ribonucleoprotein (vRNP) [183–185].

Regardless of genome composition (i.e. either seven or eight segments), influenza viruses predominantly package eight vRNPs, termed the “7+1” arrangement [186–189]. Terminal regions of both the 5’ and 3’ portions of each segment comprise packaging signals to ensure incorporation into the 7+1 bundle and inclusion in nascent budding particles [190,191] (**Fig. 1.5A**). Influenza A virions contain at most one of each unique segment and are believed to package all eight segments with high efficiency [192]. Longer, filamentous virions do not contain additional genomic copies or other electron-dense structures [175,176,193].

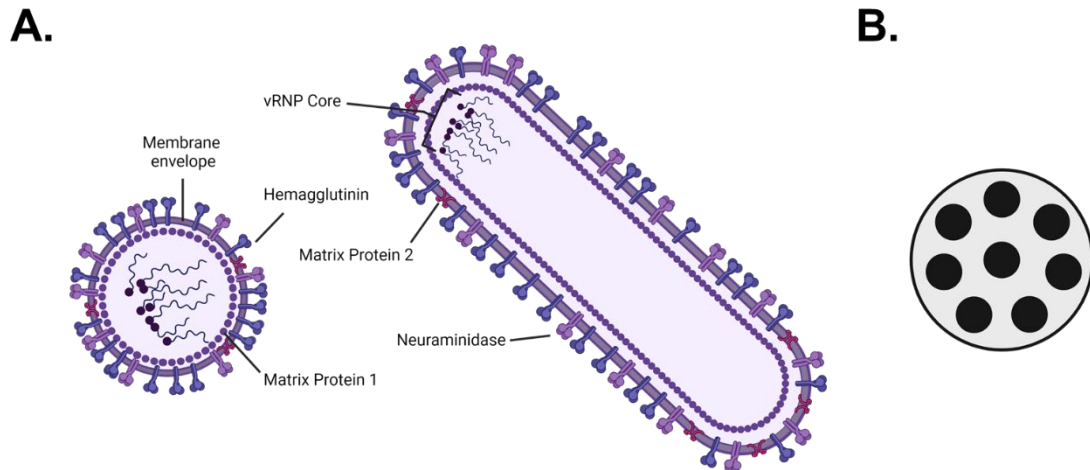


Figure 1.4. Structure of the Influenza A Virus. (A) Spherical (left) and filamentous (right) morphologies of influenza A virus. Glycoproteins and matrix protein 2 channel stud the membrane envelope which is in contact with a layer of matrix protein 1. (B) Eight vRNP arranged in the “7+1” pattern are either central to (in the case of spherical particles) or at one end (in the case of filamentous particles) of the virion. Spherical particles are roughly 100-120 nm in diameter while filamentous particles are 80-100 nm across their short axis. Created with BioRender.com

1.6 Influenza A Virus Life Cycle

1.6.1 Attachment and Entry

Influenza A viruses initiate infection by interacting with various forms of sialic acid (e.g. *N*-acetylneuraminic acid) moieties terminating O- and N-linked glycans as well as glycosphingolipids through the lectin activity of HA [155,157,158,194]. The second carbon of the sialic acid can be attached to a penultimate galactose at either the third or sixth carbon, creating an α 2,3- or α 2,6-linkage [155]. While both α 2,3- and α 2,6-linked sialic acid are present throughout the human respiratory tract [195], recognition of α 2,6 sialic acid is a critical determinant in zoonotic spillover and adaption to and transmission among human hosts [196–198].

Additionally, sialic acids present in high quantities on secreted mucins represent decoy attachment sites that can prevent productive infection [160,199–201]. To combat this, NA receptor destruction activity is in balance with HA activity [163,164], freeing virions where they would otherwise be trapped [160,200]. NA is also important in the early steps of virion attachment and entry, as its inhibition leads to reduced virion uptake and therefore loss of productive infection [202,203]. The lower affinity for sialic acid by HA relative to NA [204] combined with more abundant inclusion of HA in released virions [176,177,205] can create a Brownian ‘ratchet’ effect of sequential release and reattachment or gliding along a planar membrane [202,205].

Once in contact with the constituents of a cellular membrane, the relatively low-affinity HA interactions provide a multivalent scaffolding to cluster membrane glycoproteins and glycosphingolipids [206] and the activity of NA allows for increased mobility within the plasma membrane plane until endocytosis can be achieved [202,205]. Uptake of influenza A virus is thought to be induced by the multivalent interactions with host glycoprotein and glycosphingolipids that trigger endocytosis [207–209]. The precise uptake pathway depends on the virion morphology, with filamentous virions necessitating uptake through macropinocytosis [210] while spherical particles can be taken up through macropinocytosis as well as clathrin- and caveolin-dependent routes with little bias [210,211].

While the exact identity of the endocytic vesicle might vary depending on the initial entry routes, productive infection with influenza A virus-laden vesicles requires acidified trafficking towards the lysosome and a perinuclear fate [212,213]. Vesicle acidification triggers conformational changes in HA that lead to fusion peptide invasion of the endosomal membrane [156,214,215] and, eventually, pore formation through viral-vesicle membrane fusion [216–218]. Concomitantly, the viroporin M2 allows for the efflux of

cations alongside the influx of protons to acidify and destabilize M1 contacts [219,220] allowing for the discrete uncoating step that leads to vRNP release into the cytosol [221–223].

1.6.2 Early Infection Activities

Upon uncoating, vRNPs are imported to the nucleus through recruitment of importin- α and importin- β [223,224]. Having gained access to the nucleus, vRNPs associate with RNA Pol II [225] where the cap-snatching activity of the polymerase holoenzyme allows for the initiation of primer-dependent viral transcription [226,227] (**Fig. 1.5A**). Translation of viral mRNA can occur selectively over host transcripts and potentially independently of eIF4E [228–232]. The production of host shutoff proteins NS1 and PA-X together prevent the export and cause the selective degradation host transcripts, further enhancing the selective production of viral protein [233,234]. Accumulation of replicase proteins (i.e. PB1, PB2, PA, NP) leads to the promotion of the genomic replication intermediate known as complementary RNA (cRNA) to further produce vRNA and subsequently mRNA products [185] (**Fig. 1.5A**).

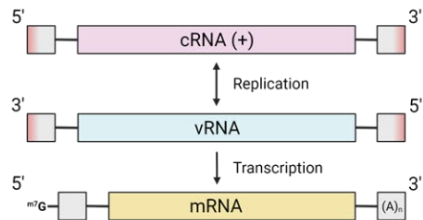
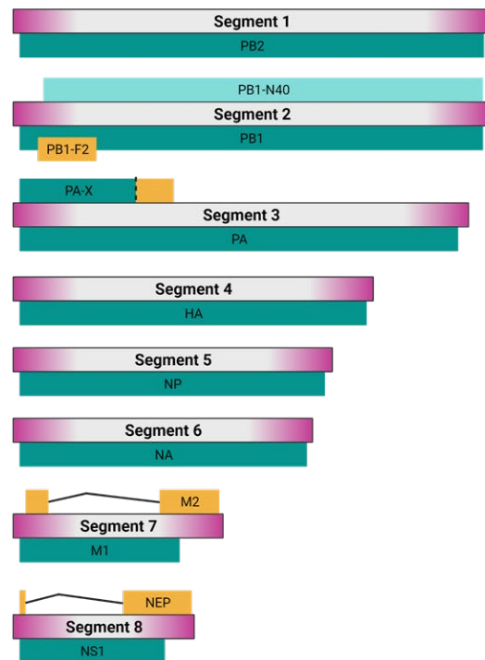
A.**B.**

Figure 1.5. Influenza A Virus Replication and Coding Schematic. (A) Influenza A virus genomic segments (vRNA) are transcribed into a translatable product (mRNA) through a 7-methylguanosine cap (m^7G) derived from a nascent host transcript. This viral mRNA represents a 10-12 nucleotide region of host-derived RNA (5' gray box) and the coding regions of the vRNA, lacking the terminal 5' and 3' non-coding regions (gray boxes with red highlights) which contain the universal polymerase promoter ("panhandle", red highlights). Complementary anti-genomes (cRNA) are produced through a primer-independent process and contain a 1:1 complement of the vRNA segment. (B) The influenza A virus coding scheme in order of segment number (determined by size). Each segment contains a packaging signal (purple highlights) which extends from the universal promoter into the coding sequence of each segment. The main protein products of each segment are shown as a green ORF as well as various conserved ancillary protein products. PB1-N40 represents an in-frame truncated product of leaky scanning. Out of frame or spliced products are shown in yellow. PB1-F2 is an out-of-frame product of leaky scanning. PA-X is resultant from a frameshift after normal PA translation initiation. M2 and NEP are splicing products of segment 7 and segment 8, respectively. Created with BioRender.com

1.6.3 Particle Assembly and Egress

The membrane proteins (i.e. HA, NA, M2) traffic to the plasma membrane where they self-organize in 'budozones', coalescing lipid rafts into larger 'barge' scaffolds

[179,180,235,236]. Independently, M1 traffics to the nucleus where it associates with vRNPs, masking their nuclear import signals, and, in conjunction with NEP, facilitates vRNP export through the CRM1 export pathway [191,237]. Outside the nucleus, vRNP condense into phase-separated organelles with Rab11 which traffic to, or directly interact with, the assembled budzone barges [238–241].

At some point in transit towards the plasma membrane and particle budding, vRNPs are capable of inter-segment interactions and organization through RNA:RNA interactions spooled out between NP oligomerization [193,242,243] (**Fig. 1.5B**). Soluble virions exhibit high rates of including eight total vRNP [188,189,244] as well as highly efficient inclusion of unique vRNP representative of each genomic segment [192], implying an acyclic tree-like network of irreversible associations [245].

As the trafficking of vRNPs to the plasma membrane can seemingly be achieved redundantly on either microtubule or actin mediated transport [246], it is unclear to what extent the budding process requires actin or microtubule networks. A functional actin network is required for filamentous virion formation generally and efficient spherical particle release [247,248]. However, actin destabilization causes budding defects that phenocopy functional loss of Rab11 [249] and M2 [250]. Thus the extent to which active motor or cytoskeletal involvement is required during the budding and membrane deformation process itself as opposed to budzone organization and viral protein trafficking is unclear [246]. In any case, while it is unclear how the budding process is initiated mechanistically, it stringently selects for a proper 7+1 arrangement after contact with the viral budzone, even in the absence of eight unique segments [188,189].

Virion budding terminates with membrane scission mediated by M2 clustering along the induced negative membrane curvature rather than active processes which often utilize ESCRT complexes [250]. As the filamentous phenotype is tightly associated with

segment 7 products (i.e. M1 and M2), it is thought that stable incorporation of an M1 helix as well as subsequent destabilization by M2 is one main mechanism of influenza pleomorphy [176,181,250,251]. Fully formed and detached virions are additionally kept from tethering and aggregating to other nascent virions by NA enzymatic activity [159] where they can be dispersed to subsequently begin the influenza virus replication cycle anew.

Chapter 2 : Materials and Methods

2.1 Chapter 3: Diffusion and Interactions of Influenza Virus with Secreted Mucus

2.1.1 Immortalized Cell Culture

MDCK cells were a generous gift from Dr. Wendy Barclay (Imperial College London). They were maintained at 37°C and 5% CO₂ in high-glucose DMEM (#11-965-092, Gibco), supplemented with 10% fetal bovine serum (Genclone) and passaged at 100% confluence with 0.25% trypsin-EDTA (25200-072, Gibco). HEK293T cells were purchased through ATCC (#CRL-11268 and were maintained at 37°C and 5% CO₂ in high-glucose DMEM, supplemented with 10% fetal bovine serum. HEK293T were passaged at 80-90% confluence with 0.05% trypsin-EDTA (25300-062, Gibco). Both cell lines were routinely tested for the presence of mycoplasma.

2.1.2 Influenza Virus Rescue

The reverse genetics systems for A/Puerto Rico/8/1934 (H1N1; PR8) was a generous gift from Dr. Adolfo Garcia-Sastre (Icahn School of Medicine at Mount Sinai). The reverse genetic plasmids for PR8 (utilizing the pDZ backbone) were validated using

the primer 5' GTG TGT CCT GGG GTT GAC CA 3'. Infectious stocks of PR8 were produced by plasmid transfection in 293T cells and subsequent co-culture with Madin-Darby Canine Kidney (MDCK) cells [252]. Amplification of rescued viruses was carried out with an infection (0.01 MOI) of confluent MDCK monolayers in the presence of 1.5 µg / mL of TPCK Trypsin supplemented serum free high-glucose DMEM was allowed to proceed 72 hours or until at most 25% of cells remained adherent. Sodium bicarbonate (NaHCO₃) was added as needed to maintain neutral pH and the supernatant was clarified with a 1,000 g spin at 4°C for 15 minutes.

Clarified virus-laden supernatant was concentrated and purified at 4°C through 20% sucrose (solubilized in NTE buffer; 100 mM NaCl, 10 mM Tris [pH 7.4], 1 mM EDTA) layered on a 50% sucrose NTE cushion by centrifugation at 100,000 g (25,000 RPM, SW-41Ti; calculated relative to the bottom of the bucket) for 2 hours. Virus at the interface was collected, mixed thoroughly by pipetting and vortexing, and then aliquoted for storage at -80°C. Once frozen, an aliquot was used to determine virus titer by plaque assay on MDCK cells.

2.1.3 Viral Titration by Plaque Assay

For the titration of PR8, monolayers of MDCK cells were grown to confluence in 12 well plates. On the day of inoculation, these wells were washed with PBS prior to addition of 100 µL of viral inoculum diluted in a ten-fold dilution scheme using serum free DMEM as the matrix. During inoculation, the plates were returned to 37°C with periodic agitation for one hour. After the incubation step, the inoculum was aspirated and replaced with 0.8% molten agar in DMEM/F-12 (#12400024, Gibco) and 1.5 µg / mL TPCK trypsin (#20233, Thermo Scientific). After solidification of the overlay medium, plates were inverted and returned to incubation at 37°C for 72 hours prior to counting plaques by eye.

2.1.4 Influenza Virus Labeling and Nanoparticle Preparation

Sucrose purified PR8 was labeled with a lipophilic dye, 1,1'-dioctadecyl-3,3,3'-tetramethylindocarbocyanine perchlorate (Dil; 1:100, #D282, Invitrogen) as described in [160]. Briefly, Dil was added to viral aliquots at room temperature and vortexed for 30 seconds. The labeled virions were then purified and concentrated via hemadsorption to chicken red blood cells [253]. Final Dil-labeled IAV stocks were aliquoted and stored at -80°C . Each aliquot underwent a maximum of two freeze thaws. This strain exhibits a primarily spherical morphology and diameter of roughly 120 nm. Dil-labeled virus stocks were counter-stained with polyclonal anti-influenza virus H1 (H0) HA PR8 antibody (#NR-3148; antiserum, goat; BEI Resources, NIAID, NIH). Carboxylate modified fluorescent PS nanoparticles (PS-NP; #F8888, Life Technologies) with a diameter of 100 nm were coated with a high surface density of polyethylene glycol (PEG) via a carboxyl-amine linkage using 5-kDa methoxy PEG-amine (#PSB-332, Creative PEGWorks) as previously reported [254]. The NanoBrook Omni (Brookhaven Instruments) was used to conduct dynamic light scattering (DLS) experiments to determine particle size distribution and surface charge. We confirmed the formation of a dense PEG coating on PS-NP based on its measured zeta potential of 0.04 ± 0.71 mV (mean and standard deviation).

2.1.5 Neuraminidase Assay

The neuraminidase activity was tested using the NA-Fluor Neuraminidase Assay Kit (#4457091, Life Technologies) following the manufacturer's instructions. Fluorescence intensity was measured using a Spark Multimode Plate Reader (Tecan). A standard curve for 4-Methylumbelliferone (4-MU(SS), #M1381-25G, Sigma-Aldrich) was then generated and the fluorescence signal of 18,000 relative fluorescent units (RFU) corresponding to

20 μ M 4-MU(SS) was chosen to normalize NA activity. The neuraminidase assay kit was also used to perform a neuraminidase inhibition assay using the neuraminidase inhibitor zanamivir (#15123, Cayman Chemical). IAV neuraminidase inhibition was tested using a 1:16 dilution of IAV and varying the concentration of zanamivir from 0.01 nM to 10 μ M. In accordance with manufacturer instructions, IAV was incubated with zanamivir for 30 min before the NA-Fluor substrate was added. The reaction was incubated for 1 h at 37°C before fluorescence intensity was measured.

2.1.6 Human Mucus Collection

Human mucus was collected under an IRB-approved protocol at the University of Maryland Medical Center (UMMC; Protocol #: HP-00080047). Samples were collected by the endotracheal tube (ET) method, as previously described [254]. ET were collected from 10 donors after intubation as a part of general anesthesia at UMMC. The data presented here are from 6 male and 3 female subjects with mean age of 66 ± 12 years (note: demographic data not available for 1 patient). All adults undergoing non-cardiothoracic surgery and under general anesthesia were eligible for the study. Given we were collecting a surgical waste product (endotracheal tubes), recruitment of participants was not required as the study was exempt from informed consent. In order to collect mucus from ET, the last approximately 10 cm of the tubes were cut, including the balloon cuff, and placed in a 50 mL centrifuge tube. The ET tube was suspended in the tube with a syringe needle and was then spun at 220 g for 30 s, yielding 100–300 μ L of mucus. Mucus with visible blood contamination was not included in the analysis. Samples were stored at -80°C immediately after collection and thawed (up to 3x) prior to use for experiments.

2.1.7 Synthetic Mucus Hydrogel Preparation

Using a previously established method [255], synthetic mucus hydrogels were prepared using 2% bovine submaxillary mucin (BSM, #M3895, Sigma-Aldrich) and varying percentages of a 10 kDa thiolated 4-arm polyethylene glycol (PEG-4SH, #4arm-SH-10K, Laysan Bio Inc.) used as a thiosulfate crosslinker. The mucin and PEG-4SH crosslinker were combined in a physiological buffer (154 mM NaCl, 3 mM CaCl₂, and 15 mM NaH₂PO₄ at pH 7.4) and mixed for 2 hours. The cross-linking solution was prepared separately in buffer directly before mixing with mucin solution. To initiate gelation, equal volume aliquots of each solution were mixed and equilibrated for 21 hours at room temperature. After synthetic mucus gels were fully formed, Dil-labeled IAV and/or nanoparticles were added prior to fluorescence video microscopy experiments. There were n = 3 gels tested for each cross-linking percentage, with a total of n ≥ 100 particles per condition.

2.1.8 Fluorescence Video Microscopy

Samples were prepared for imaging by placing a vacuum grease coated O-ring on microscope cover glass. The sample was then applied to the center of the well and sealed with a coverslip. Samples were allowed to stabilize for 30 minutes at room temperature prior to imaging. Slides were imaged using Zeiss LSM 800 inverted microscope with a 63x water-immersion objective. For each sample, 10 s videos were recorded at 33.3 frames per second. For all experiments, 1 µL of Dil-labeled IAV (3×10^9 PFU / mL) and 1 µL of PEG-coated nanoparticles were added to 20 µL thawed human mucus in the center of the slide well and stirred with a pipette tip prior to imaging. After equilibration and initial imaging, samples were incubated for 15 minutes at 37°C and then imaged. For IAV with neuraminidase inhibitor (NAI) in human mucus, 1 µL of IAV labeled with Dil was mixed

with 1 μL of zanamivir and allowed to equilibrate for 10 minutes. The IAV and NAI mixture was then combined with 100 nm PS-NP and added to 20 μL of human mucus. The final concentration of NAI in the mucus sample with the IAV was 10 μM . For freeze-thaw testing, IAV was added to 20 μL of different aliquots of the same human mucus sample after 0, 1, 2, and 3 freeze-thaw cycles. For mucus treated with dithiothreitol, 1 μL of 115 mM DTT was added directly to the mucus sample, yielding a final concentration of 5 mM. On average, 137 IAV particles and 246 PS-NP were tracked per sample tested. In rare cases, a minimum of 10 IAV particles were tracked.

2.1.9 Multiple Particle Tracking (MPT) Analysis

Acquired fluorescence microscopy videos were processed using a previously developed MATLAB (The MathWorks, Natick, MA) based analysis code to isolate and track imaged particles [256–258]. For each video, the mean squared displacement (MSD) was calculated as $\langle \text{MSD}(\tau) \rangle = \langle (x^2 + y^2) \rangle$, for each particle. The MSD values of the particles were then used to determine the average α value for each sample, calculated as $\alpha = (\Delta \log \text{MSD}(\tau)) / (\Delta \log(\tau))$. All experimental data were verified to have an average α value with $0 < \alpha \leq 1$, indicative of sub-diffusive particle motion. Due to the nature of MPT, PS-NP and IAV were tracked for a maximum of 10 s due to their motion out of the focal plane. To minimize the dynamic and static error in our measurements [256–258], a lag time of 1 s was used as a representative value for comparison between conditions. The MSD values for PS-NP were then used to calculate the microrheological properties of the samples tested using the generalized Stokes-Einstein relation [259], defined as $G(s) = 2k_B T / (\pi a s \langle \Delta r^2(s) \rangle)$ gives the viscoelastic spectrum where $k_B T$ is the thermal energy, a is the radius, and s is the complex Laplace frequency [254]. The complex modulus is calculated by $G^*(\omega) = G'(\omega) + G''(i\omega)$ where $i\omega$ is used in place of s , i is a complex number,

and ω is the frequency [254]. From this equation, the pore size (ξ) can be estimated as $\xi = (kBT/G')^{1/3}$ and the complex microviscosity (η^*) can be calculated as $\eta^* = (G^*(\omega))/(\omega)$ [254]. The effective diffusivity (D) was calculated for each individual particle using the MSD values as $MSD = 4D\tau$ [260]. The average effective diffusivity for each sample was then used to calculate the estimated diffusion time (t), using the equation $t = L^2/(2D)$, where L is the thickness of the mucus layer [261]. For the estimated diffusion time, a physiological thickness of 7 μm was used for the calculations.

2.1.10 Statistics and Reproducibility

The number of patient samples used in our study were based on the number available for collection during the study. Studies in synthetic hydrogels were performed in triplicate. For each sample and treatment, PS-NP and IAV particles from at least $n = 3$ microscopy videos were tracked and pooled for analysis. Differences in measured parameters were calculated using either non-parametric two-tailed Mann-Whitney test or non-parametric Kruskal-Wallis test and Dunn's test for multiple comparisons. The resulting p-values were considered significant if $p < 0.05$. Data were statistically analyzed using GraphPad Prism 9 (GraphPad Software, San Diego, CA).

2.2 Chapter 4: Membrane-Tethered Mucin 1 is Stimulated by Interferon and

Virus Infection in Multiple Cell Types and Inhibits Influenza A Virus

Infection in Human Airway Epithelium

2.2.1 Immortalized Cell Culture

MDCK cells were a generous gift from Dr. Wendy Barclay (Imperial College London). They were maintained at 37°C and 5% CO₂ in high-glucose DMEM (#11-965-

092, Gibco), supplemented with 10% fetal bovine serum (Genclone) and passaged at 100% confluence with 0.25% trypsin-EDTA (#25200-072, Gibco). HEK293T and A549 cells were both purchased through ATCC (#CRL-11268 and #CCL-185). Both HEK293T and A549 cell lines were maintained at 37°C and 5% CO₂ in high-glucose DMEM, supplemented with 10% fetal bovine serum and passaged at 80-90% confluence with 0.05% trypsin-EDTA (#25300-062, Gibco). All cell lines were routinely tested for the presence of mycoplasma.

2.2.2 Primary Human Macrophage Cultures

Peripheral blood was collected from healthy volunteers, and mononuclear cells were separated by Ficoll-Hypaque density gradient centrifugation. Monocytes were isolated by adherence to plastic and then cultured for one week in X-VIVO 15 serum-free medium (#BE02-060Q, Lonza, Inc.) with 20 ng / mL recombinant human GM-CSF (#300-03, Peprotech). Media containing GM-CSF was replenished 4 days after initial culture. Prior to stimulation, GM-CSF-containing media was removed and replaced with X-VIVO 15 media supplemented with 5% fetal bovine serum. For HAE media stimulations, ALI media (comprising additional 25% volume) was added to X-VIVO 15 media supplemented with 5% FBS at 24 and 48 hours prior to lysate collection. All studies on human monocyte-derived macrophages were approved by the University of Maryland Institutional Review Board and formal written consent was obtained where necessary.

2.2.3 Human Airway Epithelial Cells

Human airway tracheobronchial epithelial cells isolated from airway specimens from donors without underlying lung disease were provided by Lonza, Inc. The immortalized HAE line BCI-NS1.1 was kindly provided by Drs. Matthew Walters and

Ronald Crystal of the Department of Genetic Medicine, Weill Cornell Medical College, NY [98]. Both primary cells derived from single patient sources and BCI-NS1.1 airway epithelial cells were first expanded on plastic in Pneumacult-Ex or Pneumacult-Ex Plus medium (#05008 or #05040, StemCell Technologies). Airway cells were then seeded (3.3×10^4 cells / well for StemCell media; 5×10^4 cells / well for Lonza or Spirovision media) on rat-tail collagen type 1-coated permeable Transwell membrane supports (#3470, 6.5 mm, Corning, Inc.) and differentiated in Pneumacult-ALI medium (#05001, StemCell Technologies) or custom ALI media (Spirovision, UNC Marsico Lung Institute) with provision of an air-liquid interface for approximately 6 weeks to form polarized cultures that resemble *in vivo* pseudostratified mucociliary epithelium. All cell cultures were maintained at 37°C with 5% CO₂.

2.2.4 Influenza Viruses and Mutant Cloning

The reverse genetics systems for A/Puerto Rico/8/1934 (H1N1; PR8), A/Udorn/307/72 (H3N2; Udorn), and A/Perth/16/09 (H3N2) [262], were generous gifts from Drs. Adolfo Garcia-Sastre (Icahn School of Medicine at Mount Sinai), Robert Lamb (Northwestern University), and Jesse Bloom (Fred Hutchinson Cancer Research Center), respectively. Reverse genetics plasmids for viruses utilizing the pDZ backbone (i.e. PR8 and Perth/16) were validated using the primer 5' GTG TGT CCT GGG GTT GAC CA 3'. Reverse genetics helper plasmids for Udorn (pHW2000) and segment-specific plasmids (pHH21) were verified using pPoll reverse primer 5' ATG GTG GCG TTT TTG GGG ACA 3'. Live A/California/04/09 (H1N1) virus was purchased from BEI Resources (NR-13658), total RNA was extracted (#74104, Qiagen) from clarified viral supernatant per the manufacturer's instructions, processed into cDNA (#18080092, Invitrogen), and each segment's identity validated using segment-specific forward and reverse primers as previously described [263]. To produce Udorn viruses with altered SA-binding, HA

mutations E206D (E190D; H1 numbering) and L242Q / S244G (L226Q / S228G; H1 numbering) were introduced into the A/Udorn/307/72 reverse genetics system. Specifically, E206D was achieved through digestion of the segment 4 plasmid with HindIII and XbaI to insert a gBlock (segment 4 nucleotides 332-757) containing the GAA to GAU transversion which is predicted to be codon optimized for both canines and humans. For both L242Q and S244G, the segment 4 plasmid was digested with XbaI and XhoI to insert a gBlock (segment 4 nucleotides 712-1327). Specifically, L242Q was achieved through CTG to CAA double mutation rather than the single and human codon preferred CAG transversion as a greater barrier to reversion mutation. S244G was achieved through AGT to GGA double mutation to avoid GC/CG dinucleotide bias and avoid codon bias in both canine and human hosts.

2.2.5 Influenza Virus Rescue and Sucrose Gradient Purification

For viruses derived directly from reverse genetics systems, infectious virus stocks were produced by plasmid transfection in 293T cells and subsequent co-culture with Madin-Darby Canine Kidney (MDCK) cells [252]. Notably, Udorn E190D and L226Q/S228G mutant virus stocks were sequenced after rescue to ensure retention of the introduced nucleotide changes. Amplification of rescued viruses was carried out with an infection (0.01 or 0.001 MOI) of confluent MDCK monolayers in the presence of 1.5 µg / mL of TPCK Trypsin supplemented serum free high-glucose DMEM was allowed to proceed 72 hours or until at most 25% of cells remained adherent. Sodium bicarbonate (NaHCO₃) was added as needed to maintain neutral pH and the supernatant was clarified with a 1,000 g spin at 4°C for 15 minutes.

Clarified virus-laden supernatant was concentrated and purified at 4°C through 20% sucrose (solubilized in NTE buffer; 100 mM NaCl, 10 mM Tris [pH 7.4], 1 mM EDTA)

layered on a 50% sucrose NTE cushion by centrifugation at 100,000 g (25,000 RPM, SW-41Ti; calculated relative to the bottom of the bucket) for 2 hours. Virus at the interface was collected, mixed thoroughly by pipetting and vortexing, and then aliquoted for storage at -80°C. Once frozen, an aliquot was used to determine virus titer by plaque assay on MDCK cells.

2.2.6 Influenza Virus Biotinylation

Sucrose purified A/Udorn/307/72 (4.7×10^7 PFU / mL) was dialyzed against 0.1 M carbonate (NaHCO_3) and 100 mM NaCl reaction buffer. EZ-Link NHS-Biotin (#20217, Thermo Scientific) was freshly solubilized in DMSO before addition to virus in the reaction buffer at 1 μM . The virus-biotin mixture was incubated on ice for 20 minutes with gentle shaking before doubling of the biotin conjugate concentration to 2 μM . After a further 20 minutes, the reaction was quenched with the addition of chilled 50 mM glycine for 10 minutes. Labeled virus was then dialyzed overnight against PBS before being aliquoted and infectivity subsequently analyzed by plaque assay. To confirm biotinylation, samples were separated on an SDS-PAGE and visualized by Western blot as described in section 2.2.18 with the following modifications: First, water was added to replace the sample reducing agent. Second, the membrane was blocked with SuperBlock (#37515, Thermo Scientific) for 1 hour at room temperature instead of 5% milk in TBST. To confirm labeled virus retained infectivity and tropism for both ciliated and non-ciliated cells on HAE cultures, 25 μL of labeled virus was allowed to adsorb for two hours prior to inoculum removal. The infection was allowed to proceed for 24 hours prior to culture fixation and staining for both viral antigen and ciliated cell markers as described in the microscopy section.

2.2.7 Plaque Assay

Monolayers of MDCK cells were grown to confluence in 12 well plates. On the day of inoculation, these wells were washed with PBS prior to addition of 100 μ L of viral inoculum diluted in a ten-fold dilution scheme using serum free DMEM as the matrix. During inoculation, the plates were returned to 37°C with periodic agitation for one hour. After the incubation step, the inoculum was aspirated and replaced with 0.8% molten agar in DMEM/F-12 (#12400024, Gibco) and 1.5 μ g / mL TPCK trypsin (#20233, Thermo Scientific). After solidification of the overlay medium, plates were inverted and returned to incubation at 37°C for 72 hours prior to counting plaques by eye.

2.2.8 Influenza Virus Infection of Human Airway Epithelium

For IAV infection of unmodified HAE, cultures were washed with PBS for 15 minutes at 37°C to remove apical secretions and supplied with fresh basolateral medium prior to inoculation with sucrose-purified virus diluted in PBS to achieved indicated PFU in a final volume of 50 μ L. Inoculum was applied to the apical surface of HAE for 2 hours at 37°C. Following incubation, viral inocula were removed, and cultures were washed once with PBS for 10 minutes to remove unbound virus. At specific time points post-inoculation, progeny virus was harvested at indicated times by performing apical washes with 50 μ L of PBS for 30 min at 37°C and stored at -80°C prior to analysis.

2.2.9 Unwashed HAE Infection Timecourse

For infection in unmodified HAE, the methods in section 2.1.7 were followed. To better mimic natural infection for time course infections in CRISPR/Cas9-modified, BCI-NS1.1-derived HAE, cultures were washed with PBS for 30 minutes at 37°C then incubated for 7 days to allow recovery of the secreted mucus layer prior to inoculation. In

these experiments, sucrose-purified viruses were diluted to 500 PFU (approximate MOI of 0.01) in 10 μ L PBS and inocula were not removed. For all experiments, progeny virus was harvested at indicated times by performing apical washes with 50 μ L of PBS for 30 min at 37°C and stored at -80°C prior to analysis. To measure cytotoxicity, LDH in apical washes was measured with CytoTox 96 (Promega #G1780) according to the manufacturer's instructions.

2.2.10 Influenza Virus Kinetic Entry Assay

For the analysis of influenza virus entry kinetics in non-targeting control and MUC1 KO cultures, cultures were left unwashed for 7 days but otherwise maintained as normal. Then, 5,000 PFU (approximately an MOI of 0.1) of A/Udorn/307/72 was applied apically in a 30 μ L volume for the indicated time prior to inoculation removal. Immediately following inoculation removal, apical and basolateral compartments were replaced with PBS and standard ALI media, respectively, supplemented with 1,250 nM of the neuraminidase inhibitor zanamivir. The cultures were then returned for incubation at 37°C until 12 hpi at which point they were fixed and processed for viral antigen staining *en face* as described in section 2.1.9.

2.2.11 Culture Stimulation Experiments

Unless specified elsewhere, recombinant human IFN β (1 nM, #11415-1, PBL Assay Science), IFN λ 3 (10 nM, #11730-1, PBL Assay Science), Ruxolitinib (2 μ M, #S1378, SelleckChem), and DMSO (ATCC) were applied to cell culture media or to indicated chambers of HAE cultures. TNF α (20 ng / mL, #210-TA, R&D Systems) was applied apically to HAE cultures. Apical stimulations or vehicle treatment of HAE cultures

was performed in a volume of 30 μ L PBS. For experiments with primary macrophage cultures, IFN β (1 nM), IFN λ 3 (10 nM), TNF α (20 ng / mL), low molecular weight Poly(I:C) (10 μ g / mL, #k-picw, InvivoGen), and LPS (100 ng / mL *E. coli* K12, #k-eklps, Invivogen) with IFN γ (20 ng / mL, #285-IF, R&D Systems) were supplemented into X-VIVO 15 media and 5% fetal bovine serum at indicated time points prior to lysis.

2.2.12 HAE Culture Histology and Immunohistochemistry Preparations

HAE cultures were fixed in 4% paraformaldehyde overnight prior to paraffin embedding and sectioning at either the Marsico Lung Institute Histology Core (Chapel Hill, NC) or the New York University Experimental Pathology Research Laboratory (New York, NY). Five micron-thick sections on slides were deparaffinized with xylene and rehydrated through gradient ethanol washes into distilled water. For all stains except those utilizing rH3-Fc probes, heat antigen retrieval was performed as follows: citrate buffer (2.94 g / L), pH 6.0, with 0.05% Tween-20 was heated to 98°C to boil deparaffinized slides for 15 minutes. After cooling the slides and washing in water, the normal IHC staining protocol was resumed. Slides were blocked with 3% BSA in PBS supplemented with 1 mM CaCl₂ and 1 mM MgCl₂ (PBS++). Primary antibodies were diluted in 1% BSA / PBS++ and incubated with the sample overnight at room temperature. Slides were then washed with PBS++ and secondary antibodies (also diluted in 1% BSA / PBS++) added for one hour at room temperature. Slides were then stained with Hoechst 33342 Solution (1:1,000, #H3570, Thermo Scientific) for 5 minutes at room temperature, washed a final time with PBS++, and coverslips mounted with Vectashield antifade mounting solution (#H-1000, Vector Laboratories).

2.2.13 *En Face* Immunofluorescent Staining of HAE Cultures

To prepare HAE cultures for *en face* IF staining, cultures were fixed in 4% paraformaldehyde for 20 minutes, washed with PBS++, permeabilized with 2.5% Triton X-100 in PBS++ for 15 minutes, and blocked with 3% BSA in PBS++ for one hour, all at room temperature. The IF antibody staining procedure was the same as for IHC except that overnight incubation steps were carried out at 4°C.

2.2.14 Primary and Secondary Antibodies

Antibodies and dilutions used were as follows:

Table 2.1: Primary, Secondary, and Isotype Antibody Probes Used in Chapter 4:

Target	Clone	Source	Catalog #	Dilution	Application
Primary probes					
Acetylated alpha tubulin	6-11B-1	Abcam	ab24610	1:2,000	IHC
Acetylated alpha tubulin AlexaFluor-647	6-11B-1	Santa Cruz	sc-23950 AF647	1:100	IHC; IF
anti-Actin-HRP	AC-15	Sigma-Aldrich	A3854	1:35,000	WB
MUC1-CT	MH1, CT2	Invitrogen	MA5-11202	1:150; 1:50; 1:10,000	IHC; IF; WB
MUC1-ED	B27.29	gift from Fujirebio	N/A	5 µg / mL; 5 µg / mL;	IHC; IF; WB; EM

		Diagnostics Inc		1.9 µg / mL; 2.04 µg / mL	
MUC16	X325	Abcam	ab10033	1:1,000; 1:5,000	IHC; WB
MUC4	1G8	Santa Cruz	sc-33654	1:100; 1:1,000	IHC; WB
rH3-Fc	N/A	gift from Drs. Ian Jones and Silvia Loureiro (University of Reading)	N/A	1 µg; 1 µg	IHC; WB
MX1	N2C2	GeneTex	GTX110256	1:10,000	WB
Influenza virus NP	A1 and A3	Sigma-Aldrich	MAB8251	1:100	IF
Secondary probes					
anti-Armenian hamster IgG AlexaFluor-647	N/A	Abcam	ab173004	1:500	IHC; IF
anti-Human IgG Fc	N/A	Invitrogen	31125	1 µg	IHC
Anti-Human IgG Fc-HRP	N/A	Invitrogen	A18829	1:10,000	WB
anti-Goat IgG AlexaFluor-488	N/A	Invitrogen	A-11055	1:500	IF

anti-mouse IgG AlexaFluor-488	N/A	Invitrogen	A-11001	1:500	IHC; IF
anti-rabbit IgG AlexaFluor-647	N/A	ThermoFisher	A31573	4.0 ug/mL	If
anti-mouse IgG HRP	N/A	Santa Cruz	Sc-516102	1:10,000	WB
anti-Armenian Hamster IgG HRP	N/A	Invitrogen	PA1-32045	1:10,000	WB
Streptavidin- HRP	N/A	Invitrogen	434323	1:10,000	WB

MUC1-CT was utilized to accommodate the use of other mouse antibodies in concurrent staining. Images were acquired with a Zeiss Axio Observer 3 Inverted fluorescence microscope equipped with a Zeiss AxioCam 503 mono camera and Zen imaging software.

2.2.15 MUC1 Immunoprecipitation

MUC1 antibody (235 µg, clone B27.29, a gift from Fujirebio Diagnostics Inc.) was conjugated to aldehyde / sulfate latex beads (six drops, #A37384, Invitrogen) through constant rotation at room temperature for 2 hours. Following incubation with anti-MUC1 antibody and subsequent washing with PBS, beads were incubated with 1 M glycine and 0.5% bovine serum albumin (BSA) at room temperature for 30 minutes without agitation to coat any remaining exposed area and prevent non-specific binding of protein during immunoprecipitation. HAE apical secretions (100 µL of PBS culture wash) were pre-

treated with triton-X (final concentration = 0.1%) before mixing with anti-MUC1-conjugated beads. Following overnight incubation at 4°C with constant inversion, the beads were washed twice with PBS and then resuspended in tris-glycine SDS-PAGE sample buffer (#LC2676, Invitrogen) and sample reducing agent (#NP0009, Invitrogen) with unbound lysate serving as a control. Samples were vortexed and heated to 95°C for 5 minutes before loading into a 4-20% tris-glycine SDS-PAGE gel in triplicate (#XP04202BOX, Invitrogen) for electrophoresis. For blotting, membranes were blocked with 5% milk and tris-buffered saline (167.8 mM Tris-HCl; 32.0 mM Trizma base, 1.5 M NaCl) with 0.1% Tween-20 (TBS-T) before incubating with one of the following primary antibodies in parallel (anti-MUC1 (clone B27.29; 1:5,000), recombinant H3-Fc (a gift from Drs. Ian Jones and Silvia Loureiro, University of Reading; 1µg), or anti-MUC16 (clone X325, 1:5,000). Recombinant hemagglutinin proteins were generated by infection of insect cells with a recombinant baculovirus expressing the protein as previously described [264]. Blots were then probed with the secondary antibody corresponding to the primary probe (anti-mouse IgGk-HRP (#sc-516102, Santa Cruz, 1:10,000); anti-human IgG Fc-HRP (#A18829, Invitrogen, 1:10,000) prior to reaction with SuperSignal West Dura substrate (#34075, Thermo Scientific) and imaging on the iBright 1500 (Thermo Fisher) machine.

2.2.16 MUC1 ELISA

Soluble MUC1 was quantified by ELISA (#EHMUC1, Invitrogen) according to the manufacturer's protocol. To collect HAE samples prior to analysis, 50 µL phosphate-buffered saline (PBS) was applied to the apical chamber and incubated for 30 minutes at 37°C. Prior to experimentation in A549 adenocarcinoma human alveolar basal epithelial cells, regular growth media (high-glucose DMEM (#11-965-092, Gibco) supplemented

with 10% fetal bovine serum (Genclone) was replaced with serum-free DMEM (#11-965-092, Gibco). HAE culture washes and A549 culture supernatants were stored at -80°C prior to analysis. Total soluble MUC1 was calculated based on concentration determined by ELISA and total volume collected.

The MUC1 ELISA (#EHMUC1, Invitrogen) was also adapted to assess MUC1 binding by biotinylated influenza virus. The standard curve and HAE lysate diluted in Diluent B (25 µg) were incubated in the wells at room temperature for 2.5 hours without agitation. Afterwards, the plate was transferred to ice with sample removal and washing with pre-chilled wash buffer. All subsequent washing steps were carried out with pre-chilled washing buffer. Pre-chilled biotin conjugate, virus biotinylated with 1 µM EZ-Link NHS-Biotin (diluted 1:10 in Diluent B), and biotinylated virus and neutralizing antibody (anti-Hong Kong/68 goat antiserum (#NR-3118, BEI Resources), 1:1,250) was added to the plate for 1 hour on ice. Biotin conjugate and biotinylated virus were removed, the plate washed, and pre-chilled streptavidin-HRP added to the plate for 45 minutes on ice. After removing the streptavidin-HRP and washing, the plate was taken off ice and allowed to equilibrate to room temperature for 15 minutes and UV-sterilized in a closed BSC. Finally, TMB substrate was added to the plate and the reaction allowed to incubate for 30 minutes in the dark at room temperature prior to the addition of stop solution and sample reading on a Labsystems Multiskan Ascent plate reader.

2.2.17 RT-qPCR

Total RNA was extracted using a RNeasy Mini Kit (#74106, Qiagen) according to the manufacturer's instructions. cDNA was prepared separately with SuperScript III (#18080044, Invitrogen) per manufacturer's random hexamer protocol. For qPCR,

reactions were carried out using LightCycler 480 SYBR Green I mastermix (#04707516001, Roche) and a Roche LightCycler 480 Instrument II at the manufacturer recommended settings. Gene targets and primers are listed in Table 2.X.

Table 2.2: RT-qPCR Target Primers from Chapter 4.

Gene Target	Forward Primer (5' to 3')	Reverse Primer (5' to 3')
MUC1	Proprietary (#QT00015379, Qiagen)	Proprietary (#QT00015379, Qiagen)
HPRT1	Proprietary (#QT00059066, Qiagen)	Proprietary (#QT00059066, Qiagen)
MX1 (ENSG00000157601)	GTT TCC GAA GTG GAC ATC GCA	CTG CAC AGG TTG TTC TCA GC
IL-8 (ENSG00000169429)	GAA TGG GTT TGC TAG AAT GTG ATA	CAG ACT AGG GTT GCC AGA TTT AAC

2.2.18 Western Blot

Protein lysate was collected with RIPA buffer (#10191-284, VWR Life Science) supplemented with 2X protease inhibitors (#A32955, Thermo Scientific). Protein concentration was quantified by BCA assay (#23225, Thermo Scientific), loaded equivalently in each lane (ranging from 4-20 µg between experiments) and run on a 4-20% Tris-Glycine gel (#XPO4205BOX, Invitrogen) under reducing conditions. Protein was transferred to a PVDF membrane (10600030, Cytiva) and blocked with 5% (w/v) fat free milk protein in TBS-T at room temperature. Unconjugated primary antibody incubations were done in the presence of blocking protein and TBS-T overnight at 4°C. Antibody details are listed in **Table 2.1**. After washing in TBS-T, membranes were probed with secondary antibodies for one hour at room temperature in blocking buffer with rocking.

Imaging was performed with chemiluminescent SuperSignal Dura or Femto reagent (Thermo Scientific) on an iBright 1500 (ThermoFisher). Densitometry in Figure

4.3 and Figure 4.5 was performed using ImageJ analysis of select band intensity (MUC1-CT or MUC1-ED where indicated) relative to same-sample actin band intensity. Within an experimental replicate, results of individual samples were then normalized to the samples indicated (represented by normalization value of 1.0). MUC1-CT antibodies were used preferentially for Western blot densitometry in HAE due to the smaller size and lack of glycosylation on this part of the mucin. MUC1-ED antibodies were used for densitometry analysis of MUC1 in PMD macrophage experiments as MUC1 expression is significantly lower than that of HAE. The MUC1-ED directed antibody detects a repeated epitope in the VNTR region of MUC1 that enhances sensitivity.

2.2.19 Transmission Electron Microscopy and Immunostaining

For transmission electron microscopy detection of virus and MUC1, two protocols were used. In the first, HAE cultures were washed and 4.7×10^6 PFU (approximately an MOI of 94) sucrose-purified A/Udorn/307/72 was allowed to adsorb for one hour at 37°C followed by transfer of the cultures to 4°C for all subsequent steps up to fixation. In the second, HAE cultures were washed and 5×10^5 PFU (approximately an MOI of 10) of dialyzed, sucrose-purified A/Udorn/307/72 was allowed to adsorb for 2 hours at. Virus inoculum was removed and cultures were blocked with 10% (v/v) normal donkey serum for one hour. Anti-MUC1-ED B27.29 (2.04 ug / mL) and anti-Hong Kong/68 goat antiserum (#NR-3118, BEI Resources) was added in the presence of blocking serum overnight. Cultures were washed with PBS++ to remove primary antibodies before addition of 18 nm-gold conjugated anti-mouse (#115-215-166, Jackson ImmunoResearch Laboratories, Inc. 1:10) and 6 nm-gold conjugated anti-goat (#705-195-147, Jackson ImmunoResearch Laboratories, Inc., 1:20) in blocking solution for one hour. Secondary antibodies were removed, cultures washed and subsequently fixed in 2% glutaraldehyde in 0.1M

cacodylate buffer for one hour at room temperature. Following a further washing step in 0.1 M cacodylate buffer, a secondary fixation step using 1% OsO₄ and 1% K₃Fe(CN)₆ in 0.1M cacodylate buffer was performed for one hour. A final wash of 0.1M cacodylate buffer was performed before post-fixation treatment with 2% uranyl acetate solution in dsH₂O for one hour. Cultures were then dehydrated in increasing concentrations of ethanol. Finally, cultures were infiltrated with 100% propylene oxide and subsequently increasing ratios of Spurr's Resin up to the final embedding step of 100% Spurr's Resin. Cultures were then imaged at 80kV on the Hitachi HT7700 Transmission Electron Microscope at the Laboratory for Biological Ultrastructure at the University of Maryland.

2.2.20 CRISPR gRNA Design

To select regions for CRISPR/Cas9-mediated knockout, MUC1 (ENSG00000185499) was analyzed using Ensembl [25]. Guide RNA sites were selected based on favorable targeting, Doench, and Xu scores. Putative guides were ordered from IDT with flanking restriction sites for cloning into the plentiCRISPRv2 backbone [265] with eGFP replacing puromycin selection. The final guide targets region 155,187,791 – 155,187,813 on chromosome 1 with WTSI Genome Editing ID of 915343298. To generate negative control gRNA sequences with no matching sequence in the genome (non-targeting control), we generated 10,000 random sequences of 20 nucleotides and analyzed these candidates using BLAST [266] to characterize their match percent identity against the hg19 reference genome. We chose the gRNAs sequence with the least match percent identity i.e. lowest probability of a sequence match in the genome, as the negative controls. To improve the confidence of our hits, we repeated this process at a wide

range of coverage thresholds (99-70%) and chose top-ranked candidates consistently ranked among top ones (average rank). We used the following control sequence, which was validated as described above: (5' - CGA CTA CCA GAG CTA ACT CA - 3').

2.2.21 Lentiviral Transduction

Lentiviral stocks were generated by co-transfection of 1 µg plentiCRISPRv2 (a gift from Dr. Feng Zhang (Addgene plasmid #52961; <http://n2t.net/addgene:52961>; RRID:Addgene_52961)), 0.2 µg pCMV-VSV-G (a gift from Dr. Bob Weinberg (Addgene plasmid #8454; <http://n2t.net/addgene:8454>; RRID:Addgene_8454)) [267], and 0.7 µg psPAX2 (a gift from Dr. Didier Trono (Addgene plasmid #12260; <http://n2t.net/addgene:12260>; RRID:Addgene_12260)) into HEK293T cells with XtremeGENE HP (#6366244001, Roche) in OptiMEM (#31985062, Invitrogen) per manufacturer's protocol. Lentivirus-laden supernatant was collected and replaced at 24-hour intervals up to 72 hours, pooled, and filtered to remove viable cells and debris.

For target cell transduction, lentivirus-containing supernatant was applied to BCi-NS1.1 (kindly provided by Drs. Matthew Walters and Ronald Crystal (Weill Cornell Medical College); maintained as HAE above, [98]) at 40-60% confluence with a final concentration of 20 mM HEPES (#15630080, Gibco) and 4 µg / mL Polybrene (#AB01643, American Bio). Cells were then centrifuged (1,000 *g* for one hour at 37°C) and incubated at 37°C overnight. The inoculum was removed and replaced with fresh growth media. At 60-80% confluence cells were passaged and expanded prior to being sorted for eGFP expression compared to untransduced control cells. Sorted transduced cells were frozen down for later use.

2.2.22 Mutagenesis Assay and Sequencing

DNA from undifferentiated and freshly-sorted BCI-NS1.1 were extracted per the manufacturer's protocol with QuickExtract DNA Extraction Solution (#QE09050, Epicentre). Afterwards, 5 µL of extracted DNA was used for PCR amplification with EnGen Mutation Detection Kit (#E3321S, New England BioLabs) and MUC1-specific primers (Forward: 5' – AGC ACT TCT CCC CAG TTG TC 3'; Reverse: 5' - CAG GGA CTG CAC TCA CCA AG 3') corresponding to an 862 base pair fragment spanning positions 5217-6078 on the MUC1 (Ensembl: ENSG00000185499) sequence. Annealing was carried out at 68°C while all other steps were to the specifications suggested by the manufacturer. This PCR product was the basis for the heteroduplex and endonuclease cleavage assay, both performed per the manufacturer's recommendations, before being analyzed by agarose gel electrophoresis and UV-illuminated through SYBR Safe DNA Gel Stain (#S33102, Invitrogen).

For Sanger sequencing and editing analysis, DNA from differentiated cultures was extracted in 300 µL of QuickExtract solution per the manufacturer's protocol. Afterwards, 5 µL of this solution was used for PCR with the EnGen polymerase mix as described above. This reaction was then cleaned up by column purification (#T1030S, Monarch PCR & DNA Cleanup Kit) and Sanger sequenced (Genewiz). The resulting .abi files were then submitted to ICE Analysis (Synthego).

2.2.23 Software Used and Statistical Analysis

FIJI [268] was used to quantify fluorescence intensity in IF experiments and band intensity of indicated Western blot developments. Statistical analyses were performed using native GraphPad Prism 8 software. Specifically, the non-parametric Mann-Whitney

U test was used to test for statistical significance. Results with a value for $p < 0.05$ were considered statistically significant.

2.3 Chapter 5: Interferon Responses in HAE and Impact on Viral Infection

Dynamics

2.3.1 Immortalized Cell Culture

MDCK cells were a generous gift from Dr. Wendy Barclay (Imperial College London). They were maintained at 37°C and 5% CO₂ in high-glucose DMEM (#11-965-092, Gibco), supplemented with 10% fetal bovine serum (Genclone) and passaged at 100% confluence with 0.25% trypsin-EDTA (25200-072, Gibco). HEK293T cells were purchased through ATCC (#CRL-11268). HEK293T cells were maintained at 37°C and 5% CO₂ in high-glucose DMEM supplemented with 10% fetal bovine serum and passaged at 80-90% confluence with 0.05% trypsin-EDTA (#25300-062, Gibco). Vero-E6 cells (#CRL-1586, ATCC) were maintained in DMEM (#10-017-CV, Corning) supplemented with 10% FBS and 1% Penicillin Streptomycin (#15-140-122, Fisher Scientific). All cell lines were routinely tested for the presence of mycoplasma.

2.3.2 Influenza and SARS-CoV-2 Viruses Used

The reverse genetics systems for A/Puerto Rico/8/1934 (H1N1; PR8) was a generous gift from Dr. Adolfo Garcia-Sastre (Icahn School of Medicine at Mount Sinai). The reverse genetic plasmids for PR8 (utilizing the pDZ backbone) were validated using the primer 5' GTG TGT CCT GGG GTT GAC CA 3'. Infectious stocks of PR8 were produced by plasmid transfection in 293T cells and subsequent co-culture with Madin-Darby Canine Kidney (MDCK) cells [252]. Amplification of rescued viruses was carried out with an infection (0.01 MOI) of confluent MDCK monolayers in the presence of 1.5 µg /

mL of TPCK Trypsin supplemented serum free high-glucose DMEM was allowed to proceed 72 hours or until at most 25% of cells remained adherent. Sodium bicarbonate (NaHCO_3) was added as needed to maintain neutral pH and the supernatant was clarified with a 1,000 g spin at 4°C for 15 minutes.

Clarified virus-laden supernatant was concentrated and purified at 4°C through 20% sucrose (solubilized in NTE buffer; 100 mM NaCl, 10 mM Tris [pH 7.4], 1 mM EDTA) layered on a 50% sucrose NTE cushion by centrifugation at 100,000 g (25,000 RPM, SW-41Ti; calculated relative to the bottom of the bucket) for 2 hours. Virus at the interface was collected, mixed thoroughly by pipetting and vortexing, and then aliquoted for storage at -80°C. Once frozen, an aliquot was used to determine virus titer by plaque assay on MDCK cells.

All SARS-CoV-2 propagations and experiments were performed in a Biosafety Level 3 facility at Icahn School of Medicine at Mount Sinai in compliance with institutional protocols and federal guidelines. The WA1/2020 SARS-CoV-2 isolate from BEI (#NR-52281) was propagated on passage 2 Vero-E6 cells in DMEM supplemented with 2% FBS. The fourth passage amplification of this stock was concentrated with 100 kDa MWCO Amicon filters (#UFC910024, Millipore Sigma) by centrifugation at 8,000 g for 15 minutes and subsequently supplemented with 50 mM HEPES (#15630080, Gibco).

2.3.3 Viral Titration by Plaque Assay

For the titration of PR8, monolayers of MDCK cells were grown to confluence in 12 well plates. On the day of inoculation, these wells were washed with PBS prior to addition of 100 μL of viral inoculum diluted in a ten-fold dilution scheme using serum free DMEM as the matrix. During inoculation, the plates were returned to 37°C with periodic agitation for one hour. After the incubation step, the inoculum was aspirated and replaced

with 0.8% molten agar in DMEM/F-12 (#12400024, Gibco) and 1.5 µg / mL TPCK trypsin (#20233, Thermo Scientific). After solidification of the overlay medium, plates were inverted and returned to incubation at 37°C for 72 hours prior to counting plaques by eye.

For the titration of SARS-CoV-2, Vero-E6 cells were grown to confluence in 6-well plates. Virus was subsequently inoculated in each well through sequential dilution. Briefly, inoculum was applied to Vero-E6 for one hour at 37°C with gentle rocking every 10 minutes prior to removal and replacement with overlay medium containing Avicel. Plaques were visualized and counted after three days.

2.3.4 Human Airway Epithelial Cells

Human airway tracheobronchial epithelial cells isolated from airway specimens from donors without underlying lung disease were provided by Lonza, Inc. Primary cells derived from single patient sources were first expanded on plastic in Pneumacult-Ex or Pneumacult-Ex Plus medium (#05008 or #05040, StemCell Technologies). Airway cells were then seeded (3.3×10^4 cells / well for StemCell media; 5×10^4 cells / well for Lonza or Spirovision media) on rat-tail collagen type 1-coated permeable Transwell membrane supports (#3470, 6.5 mm, Corning, Inc.) and differentiated in Pneumacult-ALI medium (#05001, StemCell Technologies) or custom ALI media (Spirovision, UNC Marsico Lung Institute) with provision of an air-liquid interface for approximately 6 weeks to form polarized cultures that resemble *in vivo* pseudostratified mucociliary epithelium. All cell cultures were maintained at 37°C with 5% CO₂.

2.3.5 Infection of Human Airway Epithelium

For IAV infection of HAE, cultures were washed with PBS for 15 minutes at 37°C to remove apical secretions and supplied with fresh basolateral medium prior to

inoculation with sucrose-purified virus diluted in PBS to achieved indicated PFU in a final volume of 50 μ L. Inoculum was applied to the apical surface of HAE for 2 hours at 37°C. Following incubation, viral inocula were removed, and cultures were washed once with PBS for 10 minutes to remove unbound virus. At specific time points post-inoculation, progeny virus was harvested at indicated times by performing apical washes with 50 μ L of PBS for 30 min at 37°C and stored at -80°C prior to analysis.

For SARS-CoV-2 infection of HAE were washed with PBS as in the IAV infection protocol and inoculated with 1×10^6 PFU (approximate MOI of 20) SARS-CoV-2 in a volume of 12.5 μ L viral growth medium after Amicon column concentration. Mock infected cultures received 12.5 μ L of viral growth medium from uninfected Vero-E6 cells. Infections were allowed to proceed until the indicated time points at 37°C. After which, cultures were washed with PBS and submerged in 30 mL formalin (approximately equivalent to 4% paraformaldehyde) for 24 hours at room temperature and subsequently moved to 4°C for another 24 hours. Afterwards, cultures were gently washed with PBS and stored at 4°C prior to microscopy analysis.

2.3.6 HAE Culture Histology and Immunohistochemistry Preparations

HAE cultures were fixed in 4% paraformaldehyde overnight prior to paraffin embedding and sectioning at either the Marsico Lung Institute Histology Core (Chapel Hill, NC) or the New York University Experimental Pathology Research Laboratory (New York, NY). Five micron-thick sections on slides were deparaffinized with xylene and rehydrated through gradient ethanol washes into distilled water. Slides were blocked with 3% BSA in PBS supplemented with 1 mM CaCl_2 and 1 mM MgCl_2 (PBS++). Primary antibodies were diluted in 1% BSA / PBS++ and incubated with the sample overnight at room temperature. Slides were then washed with PBS++ and secondary antibodies (also diluted in 1% BSA

/ PBS++) added for one hour at room temperature. Slides were then stained with Hoechst 33342 Solution (1:1,000, #H3570, Thermo Scientific) for 5 minutes at room temperature and subsequently washed a final time with PBS++, and coverslips mounted with Vectashield antifade mounting solution (#H-1000, Vector Laboratories).

2.3.7 *En Face* Immunofluorescent Staining of HAE Cultures

To prepare HAE cultures for *en face* IF staining, cultures were fixed in 4% paraformaldehyde for 20 minutes, washed with PBS++, permeabilized with 2.5% Triton X-100 in PBS++ for 15 minutes, and blocked with 3% BSA in PBS++ for 1 hour, all at room temperature. The IF antibody staining procedure was the same as for IHC except that overnight incubation steps were carried out at 4°C.

2.3.8 Flow Cytometry

After treatment with IFN, cultures were dissociated as in section 2.4.12 up until the cells are pelleted. Cell pellets are then resuspended in BD cytofix/cytoperm (#554714, BD) per manufacturing instructions. Samples were suspended in flow cytometry running buffer (0.1% BSA / 10 mM HEPES / PBS) and stained with antibodies listed in 2.4.8. All data was acquired using a FACSCanto II and processed with FACSDiva and FlowJo software.

2.3.9 Primary and Secondary Antibodies

Antibodies and dilutions used were as follows:

Table 2.3: Primary, Secondary, and Isotype Antibody Probes Used in Chapter 5:

Target	Clone	Source	Catalog #	Dilution	Application
--------	-------	--------	-----------	----------	-------------

Primary probes					
Acetylated alpha tubulin	6-11B-1	Abcam	Ab24610	1:2000	IHC
Acetylated alpha tubulin AlexaFluor-647	6-11B-1	Santa Cruz	sc-23950 AF647	1:100	IF
IFNAR1	N/A	Abcam	ab62693	1 µg / mL	IHC; WB
IFNAR2	N/A	Abcam	ab56070	1 µg / mL	IHC; WB
IFNLR1 / II28Ra	N/A	Abcam	ab224395	1.5 µg / mL	IHC; WB
IL10R2 / II10Rb	N/A	Abcam	ab106282	1:583	IHC; WB
Influenza virus NP	A1 and A3	Sigma-Aldrich	MAB8251	1:100; 1:100	IF; FC
SARS-CoV-2 N	1C7	gift from Dr. Thomas Moran (Icahn School of Medicine at Mount Sinai)		1:500	IF
KRT5	EP1601Y	Abcam	ab193895	500µg/mL	FC
CXCL10	6D4/D6/G2	BD Biosciences	555049	200µg/mL	FC
MX1	C-1	Santa Cruz	sc166412	200µg/mL	FC
CD38	HIT2	Invitrogen	12-0389-42	5µg/mL	IHC; FC
Secondary probes					

anti-Goat IgG AlexaFluor-488		Invitrogen	A-11055	1:500	IF
anti-mouse IgG AlexaFluor-488		Invitrogen	A-11001	1:500	IHC; IF; FC
anti-rabbit IgG AlexaFluor-647		ThermoFisher	A31573	4.0 ug/mL	IHC; IF
anti-mouse IgG2b	7E10G10	Abcam	ab170192	1:500	IF; FC
Isotype probes					
Rabbit IgG AlexaFluor-647	DA1E	Cell Signaling Technology	2985S	100 ug/mL	FC
Mouse IgG2a κ	G155-178	BD Biosciences	554648	200 ug/mL	FC
Mouse IgG1 κ	P3.6.2.8.1	Invitrogen	12-4714-82	200 ug/mL	FC

Images were acquired with a Zeiss Axio Observer 3 Inverted fluorescence microscope equipped with a Zeiss AxioCam 503 mono camera and Zen imaging software.

2.3.10 IFN β and IFN λ 1/ λ 3 ELISA

At 24 or 48 hpi, apical washes and basolateral medium was recovered from HAE cultures and stored at -80°C prior to analysis. IFN β (#41415-1, VeriKine-HS Human Interferon Beta ELISA Kit, PBL) and IFN λ 1 and λ 3 protein levels were assayed by (#DY1598B-05, DuoSet Human IL29/IL28) per manufacturer's instructions. Plates were read in MTX Lab Systems Multiskan Ascent Plate Reader.

2.3.11 Dextran Permeability Assay

Test conditions included collagen-coated transwells without cells or differentiated HAE on collagen-coated transwells with or without 0.5M EDTA (1:200, #15575020, Invitrogen). The apical surface of HAE cultures was washed with PBS prior to the start of the experiment. Samples were then subjected to either 1 mg / mL 20kDa Dextran-FITC (#46944, Sigma Aldrich) or vehicle on either the apical surface (100 μ L PBS) or the basolateral chamber (500 μ L) custom ALI media (Spirovention, UNC Marsico Lung Institute) and were incubated for 24 hours at 37°C. After incubation, media and PBS were collected and assayed for wavelength 520nm absorbance in a MTX Lab Systems Multiskan Ascent Plate Reader alongside standard curve. Data are expressed as a percent of total Dextran-FITC applied that was detected in each compartment after incubation.

2.3.12 Culture Stimulation Experiments

Unless specified elsewhere, recombinant human IFN β (1 nM, #11415-1, PBL Assay Science), IFN λ 3 (10 nM, #11730-1, PBL Assay Science), were applied to cell culture media or to indicated chambers of HAE cultures. Apical stimulations or vehicle treatment of HAE cultures was performed in a volume of 30 μ L PBS.

For IAV challenge of HAE cultures following IFN stimulation, the stimulation was removed, the HAE was washed briefly with PBS, and then infected with 500 PFU of A/Puerto Rico/8/34 (approximate MOI of 0.01). For SARS-CoV-2 challenge of HAE cultures, both pre- and post-treatment cultures received either treatment or vehicle apical conditions 24 hours prior to the infection time point (approximate MOI of 20). All apical treatments were removed, cultures were briefly washed for 10 minutes with PBS, and then virus or mock conditions were added. At the subsequent post-treatment time point, all cultures received mock or IFN treatments as with the pre-treatment time point.

2.3.13 Dissociation of HAE for Single-Cell RNA Sequencing

To dissociate HAE cultures for single-cell analyses, the cultures are transferred to a new plate containing TrypLE dissociative reagent (#12604013, Gibco) supplemented with 10 μ M of the RHO kinase inhibitor, Y-27632 (#SCM075, Sigma-Aldrich). Another 150 μ L of this dissociation solution was applied apically, and the cultures were returned to incubation at 37°C and monitored every 5 minutes. Once the apical morphology of the cultures began to change (by the appearance of ridges or increasingly spherical rather than cobblestone cell-cell junction morphology) the apical solution was pipetted up and down on the culture surface several times. This was collected and transferred to a conical containing HBSS (#14175-095, Gibco) supplemented with 15% FBS (#1500-500, Seradigm). Fresh dissociative was applied apically, pipetted up and down, and transferred to the trypsin neutralization solution on two-minute intervals until the entire culture was removed from the Transwell. These suspended cells were passed through a 10 μ m filter (#431001050, PluriSelect) and pelleted at 500 g for 3 minutes. Cells were then resuspended in their normal basolateral media supplemented with 10 μ M Y-27632 and viability (>90%) was assessed for downstream sequencing application.

2.3.14 Data Processing

Sequence data were mapped and quantified in custom pipeline by Jorg Calis, based on previous work [269,270]. The resulting gene by cell matrix is used for analysis. Gene by cell matrices were converted to Seurat objects and analysis continued using Seurat [271,272] and associated pipelines. Only genes that were found in at least 3 cells were included in Seurat objects. Similarly, only cells that had counts mapped to at least 50 genes were included in Seurat objects. Upon initial data exploration of each individual

Seurat object, cells were filtered using a maximum nUMI cutoff of 5000 and a minimum nUMI cutoff of 750. Percent mitochondrial expression was defined as the fraction of UMI for each cell that mapped to genes found on the mitochondrial DNA (annotated with "MT" prefix). High loads of mitochondrial genes captured suggest mitochondrial membrane permeability, a sign of cell stress or death. Cells with percent mitochondrial gene expression above 30% were filtered from final Seurat objects.

DoubletFinder [273] was used to detect and remove putative doublets. DoubletFinder requires individual Seurat objects for each dataset to process. Therefore, individual Seurat objects were processed one at a time. A basic Seurat pipeline using 30 PCA dimensions was used to establish Seurat clusters for DoubletFinder. Filtering proceeded using a conservative homotypic doublet fraction of 0.15. After UMI, percent mitochondrial expression, and doublet filtering, SCTransform was used for dimensional reduction of each Seurat object. A percent mitochondrial expression regression was included in the SCTransform dimensional reduction.

Seurat label transfer [272] is a tool that uses a weighted vote classifier to annotate individual cells using the identities of a previously clustered and annotated reference. Similar to Seurat integration, label transfer relies on anchors derived from L2-normalized canonical correlation vectors which is highly efficient at identifying conserved gene correlation patterns despite batch or technological differences between datasets. 10X single-cell data from the human lung cell atlas (HCLA, [274]) was previously clustered and annotated to create a reference dataset to aid in identifying cells derived from or related to cells of the human lung. In this analysis, a subset reference was used that included cell types associated with the upper airway (tracheobronchial). HCLA label transfer annotations are intended to be a guide for annotating clusters, but not the 'final word'.

Individual sample datasets were integrated via Seurat using SCTransform dimensions [272].

The integrated samples were clustered using 30 principal components and default settings. This first round of clustering is for more subtle QC filtering. Previous data exploration demonstrated that clustering often revealed groups of low-quality cells such as cells with very low nUMI counts (likely empty droplets that were missed during previous filtering steps or captured nuclei) or cells with very high stress signatures. Resulting clusters with low UMI and/or defined by stress signature (as described in [275]) were excluded from further analysis. “Final” clustering was performed at a resolution of 0.8.

2.3.15 Cluster Annotation

We proceed by annotating the clusters using a multistep, supervised approach. Cluster annotation is also guided by HCLA classifications. First, we evaluate "major cell groups" by expression of established marker genes: Ciliated cells (*FOXJ1*, *CAPS*); Basal cells (*KRT5*, *TP63*); Secretory cells (*MUC5B*, *BPIFA1*); Club cells (*SCGB1A1*); Ionocytes (*CFTR*, *ASCL3*); Neuroendocrine cells (*CALCA*, *CHGA*, *ASCL1*).

Within each major cell group, we identified genes that distinguish subclusters. Next, we annotated subclusters as indicated and, where appropriate (e.g. with limited biologically significant differences in gene expression), merged subclusters. Next, we compared this to HCLA classifications as well as assess and address any discrepancies. Finally, we evaluated and annotated any remaining clusters that may not fit within major cell groups.

For differential gene expression testing of each IFN in each cell type, asking which genes were induced by IFN relative to mock. We used edgeR [276], with modifications for single cell RNA-Seq data [277].

Chapter 3 : Diffusion and Interactions of Influenza Virus with Secreted Mucus

Logan Kaler¹, Ethan Iverson², Shahed Bader¹, Daniel Song¹, Margaret A. Scull¹, and Gregg A. Duncan²

¹ Fischell Department of Bioengineering, University of Maryland, College Park, MD, USA.

² Department of Cell Biology & Molecular Genetics, Maryland Pathogen Research Institute, University of Maryland, College Park, MD, USA.

Corresponding author

Email address: gaduncan@umd.edu

This chapter features text and adaptations from a published article [278] which is licensed under a Creative Commons Attribution 4.0 International License. To view a copy of this license, visit <http://creativecommons.org/licenses/by/4.0/>.

My contribution to this work was in producing labeled IAV, measuring any effects on the titer by the labeling procedure, measuring impacts of DTT on IAV infectivity, and contributions to writing and editing the published manuscript. Additionally, I helped in the conceptual design and initial quality control with the synthetic-mucus array platform.

3.1.1 Abstract

Mucus in the lung plays an essential role as a barrier to infection by viral pathogens such as influenza A virus (IAV). Previous work determined mucin-associated sialic acid acts as a decoy receptor for IAV hemagglutinin (HA) binding and the sialic-acid cleaving enzyme, neuraminidase (NA), facilitates virus passage through mucus. However, it has yet to be fully addressed how the physical structure of the mucus gel influences its barrier function and its ability to trap viruses via glycan mediated interactions to prevent infection. To address this, IAV and nanoparticle diffusion in human airway mucus and mucin-based hydrogels is quantified using fluorescence video microscopy. We find the mobility of IAV in mucus is significantly influenced by the mesh structure of the gel and in contrast to prior reports, these effects likely influence virus passage through mucus gels to a greater extent than HA and NA activity. In addition, an analytical approach is developed to estimate the binding affinity of IAV to the mucus meshwork, yielding dissociation constants in the mM range, indicative of weak IAV-mucus binding. Our results provide important insights on how the adhesive and physical barrier properties of mucus influence the dissemination of IAV within the lung microenvironment.

3.1.2 Introduction

To establish infection, IAV must transit through the extracellular secreted mucus barrier to access underlying epithelial cells. While mostly water, the primary solid constituents to secreted mucus are proteins termed mucins which feature extensive

glycosylation of sialic acid [21,27,279]. As IAV interacts with sialic acid on cellular surfaces to mediate uptake, the presence of sialic acid among mucus has been observed to be capable of neutralizing incoming particles through adhesive interactions [160,201,280].

Despite this protective adhesive effect, the mucus-laden upper respiratory tract represents a robust site for the transmission of IAV [281,282], implying this protective barrier can be at least partially overcome. Indeed, mucus helps stabilize IAV on inanimate surfaces [283–285] and the mucus-containing secretions of HAE cultures stabilize IAV in aerosol particulate [286]. The nature of these adhesive interactions with sialic acid moieties is principally mediated by viral HA [279,280]. However, viral NA contains sialidase activity to destroy these receptors and is necessary to help mobilize at least some incoming particles that might otherwise be unable to penetrate the mucus barrier [160,201] and whose inhibition predicts susceptibility to neutralization by mucus [160,201,287].

In addition to adhesive interactions, secreted mucus forms a hydrogel with restrictive pores due to extensive polymeric crosslinking [21,30]. Previous work has shown that the crosslinked nature of secreted mucus can vary by mucus concentration and oxidative state [254,288,289], leading to smaller local pore sizes [290]. Recently work has reinforced the role of NA in liberating and maintaining IAV particle diffusivity in secreted mucus gels [200,201] and even particle tracking with swine IAV in porcine mucus [160]. Critically, these studies often lack real-time resolution of the diffusion of IAV within mucus or direct microstructural measurements of the mucus itself. These, microstructural analysis rely on the use of particle tracking microrheology, whereby muco-inert fluorescent nanoparticle trajectory is watched in real-time and derived mathematically [255].

Here we expand on previous observations and utilize fluorescent labeling of IAV along with muco-inert polystyrene beads to simultaneously track the real-time diffusion of

IAV in clinical mucus samples while also measuring the microstructural properties of that same sample. We also utilize a synthetic mucus model to further explore the ultrastructure of mucus on IAV diffusion and establish a tunable system for parallel, modular investigation of mucus composition on nanoparticle and viral diffusivity. Together, our data further reveal the physical barrier properties of mucus that influence the diffusion of IAV within secreted mucus, finding that the degree of mucus cross-linking plays a significant role.

3.1.3 Fluorescent Labeling and Tracking of IAV in Human Mucus Samples

To visualize individual IAV particles, we first combined a sucrose-purified stock of the common laboratory strain A/Puerto Rico/8/34 (H1N1) with the lipophilic dye, 1,1'-dioctadecyl-3,3,3',3'-tetramethylindocarbocyanine perchlorate (Dil) (**Fig. 3.1A**). To isolate Dil-labeled virions and remove unbound dye, we added chicken red blood cells to the virus and dye solution and utilized low-speed centrifugation to pellet the newly formed virus-red blood cell complexes. The supernatant (containing free dye) was removed, and Dil-labeled virus was subsequently recovered from the surface of red blood cells by resuspending the pellet in PBS and allowing the solution to warm, releasing viruses back into solution. Red blood cells were subsequently removed from the final prep through another round of centrifugation (**Fig. 3.1A**). To confirm the presence of Dil-positive IAV, we stained for the presence of exposed viral antigen, hemagglutinin (HA), on a portion of the pelleted virus-red blood cell mixture, revealing the presence of viral antigen- and Dil-double positive particles deemed to be authentic labeled virus (**Fig. 3.1B**). Dynamic light scattering analysis of the eluted, red blood cell-free Dil-labeled viral stock revealed a single peak centered slightly above 100 nm (**Fig. 3.1C**), a value consistent with the diameter of spherical IAV virions, indicating that the labeled stock was largely in-tact and not

aggregated [175]. Finally, we confirmed that the incorporation of Dil within the viral membrane did not impact viral infectivity (**Fig. 3.1D**).

We next applied the Dil-labeled IAV along with 100 nm fluorescent polystyrene nanoparticles (PS-NP) in clinical mucus samples recovered from endotracheal tubes [254]. The PS-NP are coated with poly-ethylene glycol, so as to have no adhesive interactions with secreted mucus. Because of their known size and muco-inert properties, tracking of PS-NP allows for the measurement of the mucus microstructure *in situ* [256]. By utilizing NP of similar size to IAV, we could assess the microrheological properties of the mucus samples as well as measure the diffusivity of IAV within the same sample concomitantly. Examples of individual particle transit traces are shown in **Fig. 3.1E**. From these traces we calculated a measure of particle diffusivity (**Fig. 3.1F**), known as the mean-square displacement (MSD). While we saw sample to sample heterogeneity based on the patient of origin, the overall diffusivity of IAV was not significantly different from the comparably sized PS-NP (**Fig. 3.1F**). We additionally calculated the theoretical time whereby inhaled particulate would be cleared by MCC based on the average diffusivity of the PS-NP and IAV, setting a cutoff of clearance by MCC at 30 minutes. With this cutoff, the MSD value for both PS-NP and IAV predicts that most samples would be cleared prior to transiting through the average secreted mucus gel height (**Fig. 3.1F**). Together these data heterogeneous nature of patient mucus samples and their impact on AV diffusivity.

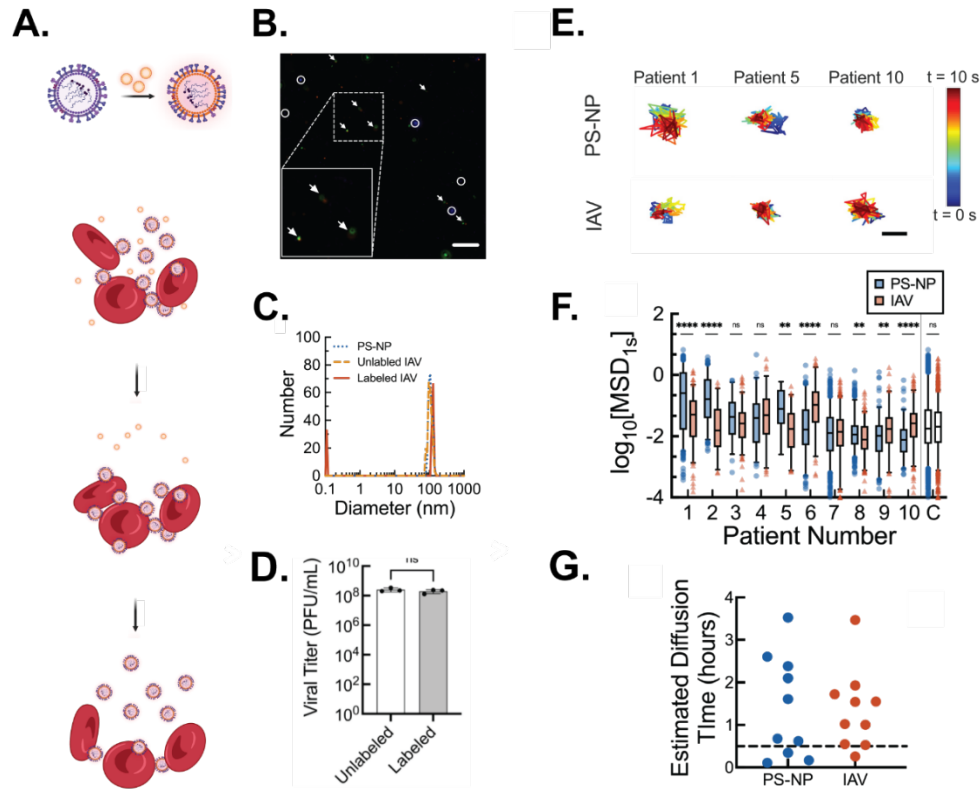


Figure 3.1. Fluorescent Labeling and Tracking of IAV in Mucus. (A) Lipophilic dye (represented by orange micelles), Dil, is incorporated into spherical IAV (A/PR/8/34) by vortexing. Subsequent hemadsorption and recovery of virions allows for the removal of unbound dye precipitates. (B) Immunostaining Dil-labeled IAV for viral antigen (hemagglutinin, green) alongside Dil fluorescence (orange). Arrows denote co-staining of green and orange channels. Circles indicate 100 nm PS-NP. Scale bar = 10 μ m. (C) Measured hydrodynamic diameter for muco-inert PS-NP (dotted blue), unlabeled IAV (dashed orange), and Dil-labeled IAV (solid red). (D) Viral titer of labeled IAV as determined by plaque assay in mock and Dil labeled conditions as indicated. Error bars indicate standard deviation. (E) Representative trajectories of polyethylene glycol (PEG) coated 100 nm polystyrene nanoparticles (PS-NP) and IAV diffusion in mucus. Traces show 10 seconds of motion with a color scale to indicate time. Scale bar = 0.2 μ m. (F) Box-and-whisker plots of log-based 10 of MSD at $\tau = 1$ s ($\log_{10}\text{MSD}$) PS-NP (blue circles) and IAV (red triangles) in mucus samples collected from 10 individual patients are shown. The combined data set for all samples tested—C—is also shown. Patients are numbered in descending order according to the median MSD of PS-NP particles in each sample. (G) Estimated diffusion time calculated from the average effective diffusivity (D) for PS-NP (blue) and IAV (red) particles to diffuse through a 7 μ m thick mucus layer. Dotted line at 30 min (0.5 hours) indicates cutoff to avoid removal due mucociliary clearance. Whiskers are drawn down to the 5th percentile, up to the 95th percentile, and the outliers are shown as points. Data sets ($n = 10$ patient samples) statistically analyzed with two-tailed Mann-Whitney test: ns = not significant; $p > 0.05$, $*p < 0.05$, $**p < 0.01$, $***p < 0.001$, $****p < 0.0001$.

3.1.4 Effect of Neuraminidase Inhibition on IAV Diffusion Through Human Mucus

Previous studies have shown the loss of NA activity can lead to immobilization within mucus gels [160,200]. It is presumed that the sialidase activity of NA is necessary to maintain IAV diffusion in a secreted mucus gel, whereby its loss leads to entrapment through HA-mucin adhesive interactions. Thus, we next sought investigate the adhesive interactions between IAV and secreted mucus as it impacts IAV diffusivity. We first validated the amount of neuraminidase inhibitor (NAI) needed to completely inactivate IAV NA (**S. Fig. 3.1**). PS-NP and IAV were then incubated with NAI prior to addition to mucus samples, achieving a final zanamivir concentration of 10 μ M previously deemed inhibitory. In analyzing IAV diffusivity, example trajectory traces can be seen in **Fig. 3.2A**. Unexpectedly, for some patient samples the pore size (ξ) as determined by PS-NP tracking was significantly altered in the presence of NAI, concomitant with changes in MSD values (**S. Fig. 3.2**). In other samples, the pore size was not significantly different (**Fig. 3.2B**), but an increased diffusivity was observed in one (patient 9) but not another (patient 5) sample (**Fig. 3.2C**). Together the possibility of mucus structural alterations due to NAI complicate straightforward interpretations about the adhesive interactions between IAV and mucus as a function of NA activity.

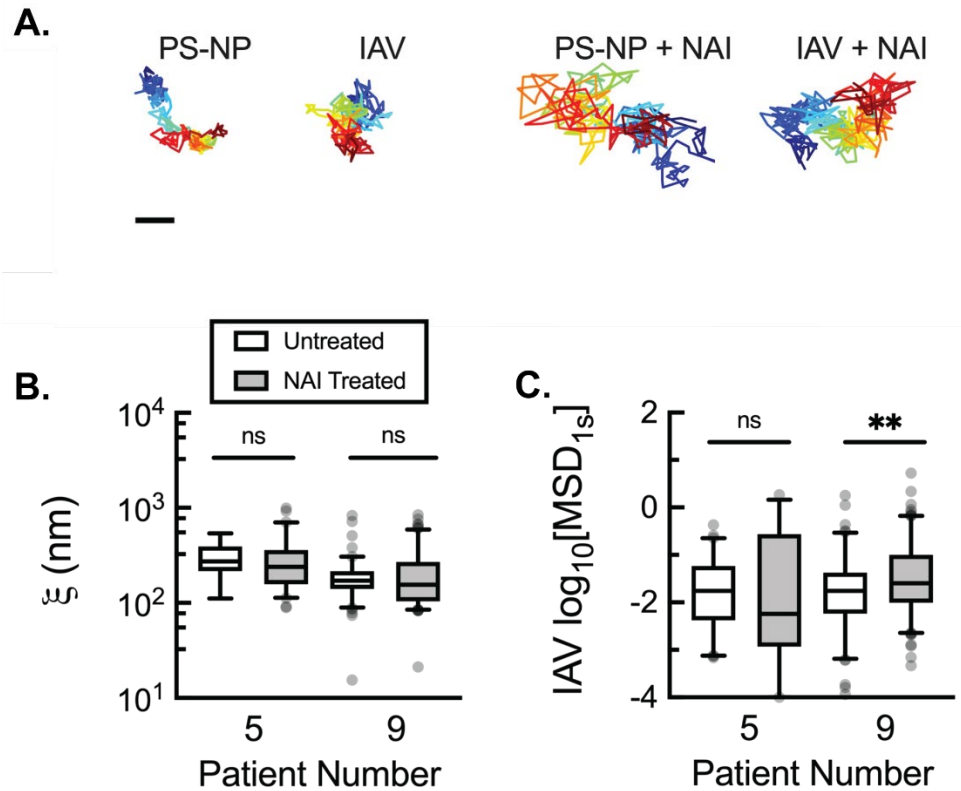


Figure 3.2. Impact of Neuraminidase Inhibition on IAV Diffusivity. (A) Representative trajectories of PS-NP and IAV untreated and treated with NAI in human mucus. Scale bar = 0.2 μm . (B) Calculated pore size (ξ) in untreated (white) and NA inhibitor (NAI) treated (zanamivir; 10 μM final concentration; grey) based on PS-NP diffusion in human mucus. (C) Measured $\log_{10}[\text{MSD}_{1s}]$ for IAV diffusion in untreated and NAI treated human mucus. Data sets ($n = 2$ patient samples) statistically analyzed with two-tailed Mann-Whitney test: ns = not significant; $p > 0.05$, * $p < 0.05$, ** $p < 0.01$.

3.1.5 Impact of Cross-linking on IAV Diffusion in Human and Synthetic Mucus

To better explore the impact of mucus pore size on IAV diffusivity, we next used the reducing agent dithiothreitol (DTT). Disulfide bonds form the basis of many polymeric crosslinking interactions between secreted mucus which can restrict particle transit through the mucus layer [21] and so the use of a reducing agent could be employed to significantly change the pore size and potentially diffusivity of IAV. We first confirmed that 5 mM concentration of DTT necessary to disrupt the mucus microstructure does not

impact IAV infectivity (**S. Fig. 3.3**). Example trace trajectories are shown in (**Fig. 3.3A**), and further analysis revealed a significantly increased pore size (**Fig. 3.3B**) concomitant with increased IAV diffusivity (**Fig. 3.3C**).

While we've shown that the disruption of crosslinking bonds between mucins can lead to larger pore sizes, we next employed a synthetic mucus system which uses thiolated PEG molecules (PEG-4SH) to facilitate disulfide linkages within purified bovine submaxillary mucin [255]. Using this approach, we are able to adjust the degree of crosslinking by increasing the amount of PEG-4SH while maintaining the total mucin concentration and sialic acid constant, removing patient sample variability. We found dramatically reduced pore sizes as PEG-4SH concentrations were increased (**Fig. 3.3D**) and moreover that this was associated with significantly reduced IAV diffusivity (**Fig. 3.3E**). Moreover, a strong association when comparing the median IAV particle diffusivity and the median pore size of each sample was seen (**S. Fig. 3.4**). Together these results demonstrate the large impact mucin pore size has on the diffusivity of IAV.

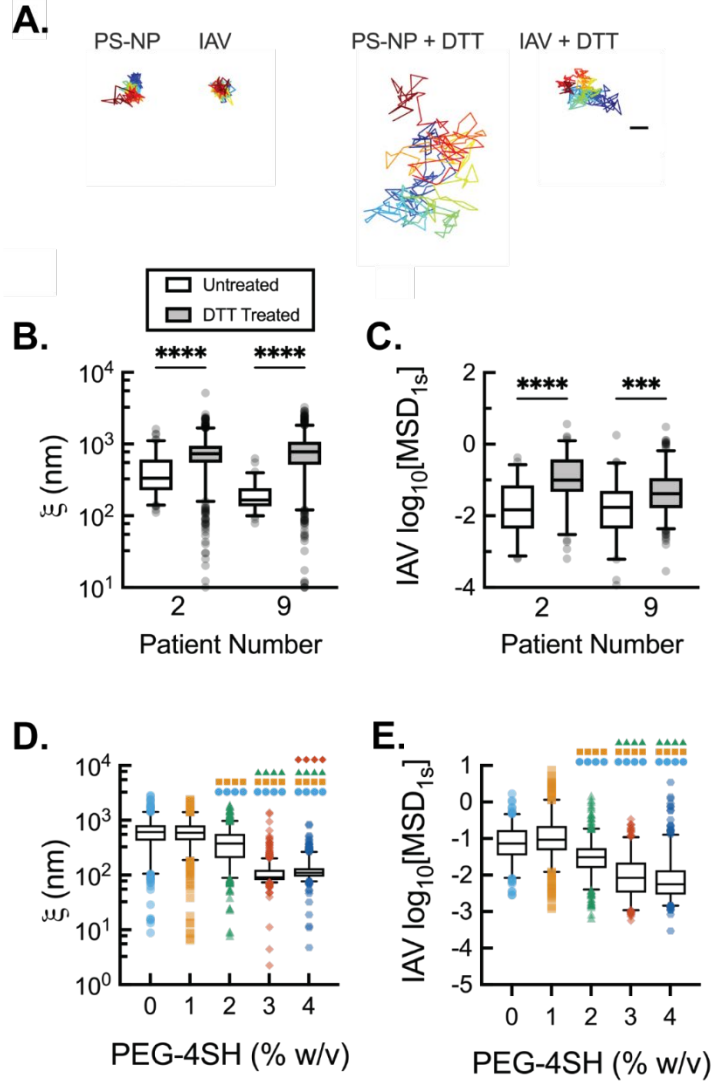


Figure 3.3. Disruption of Mucus Microstructure Enhances IAV Diffusivity. (A) Representative trajectories of PS-NP and IAV diffusion in mucus with and without DTT treatment. Scale bar = 0.2 μm . (B) Calculated mucus gel pore size (ξ) based on PS-NP diffusion in untreated (white) and DTT treated (grey) mucus (5 mM final concentration). (C) Measured $\log_{10}\text{MSD}_{1s}$ for IAV in untreated and DTT-treated mucus. (D) Calculated mucus gel pore size (ξ) based on PS-NP diffusion in synthetic mucus. (E) Measured $\log_{10}\text{MSD}_{1s}$ for IAV in synthetic mucus. Whiskers are drawn down to the 5th percentile, up to the 95th percentile, and outliers are plotted as points. For (A-C), Data sets ($n = 2$ patient samples) statistically analyzed with two-tailed Mann-Whitney test: ns = not significant; $p > 0.05$, $*p < 0.05$, $**p < 0.01$, $***p < 0.001$, $****p < 0.0001$. For (D) and (E), data sets ($n = 3$ synthetic hydrogels per group) statistically analyzed with Kruskal-Wallis test and Dunn's test for multiple comparisons: $*p < 0.05$, $**p < 0.01$, $***p < 0.001$, $****p < 0.0001$. Color and symbol indicative of comparison group: 0%, light blue circles; 1%, orange squares; 2%, green triangles; 3%, red diamonds; 4%, dark blue hexagons.

3.1.6 Impact of Mucus Composition on IAV Diffusion and Establishing a Synthetic Mucus Array

While we have shown that DTT can consistently impact the pore size of patient mucus samples, the impact of NAI was variable and unpredictable, confounding direct interpretations on the impact of NAI regarding IAV diffusivity. By contrast, the use of synthetic gel surrogates allowed for the tunable manipulation of crosslinking within bovine derived mucus. However, the use of bovine submaxillary mucus represents a MUC5B-like mucin, whereas human respiratory mucus is comprised of variable amounts of both MUC5B and MUC5AC [16]. Indeed, IAV diffusivity varies depending on the ratio of bovine submaxillary mucus (MUC5B) to porcine gastric mucus (MUC5AC) (**Fig. 3.4A,B**) and the fraction of highly mobile labeled IAV varies by composition as well (**Fig. 3.4C**). To expand on our findings on the impact of secreted mucus composition we further developed the rational design of a synthetic mucus array (**Fig. 3.4D**). This system utilizes a 3D-printed mold capable of supporting variable amounts of synthetic mucin hydrogel which can then be inserted into a 96-well plate. Importantly, this allows for parallel assessment of nanoparticle or viral transit through synthetic mucus of a highly tunable nature. Future studies can better elucidate the differential adhesive or diffusive impacts of mucin composition on nanoparticle drug delivery or even viral morphology (**S. Fig. 3.5**).

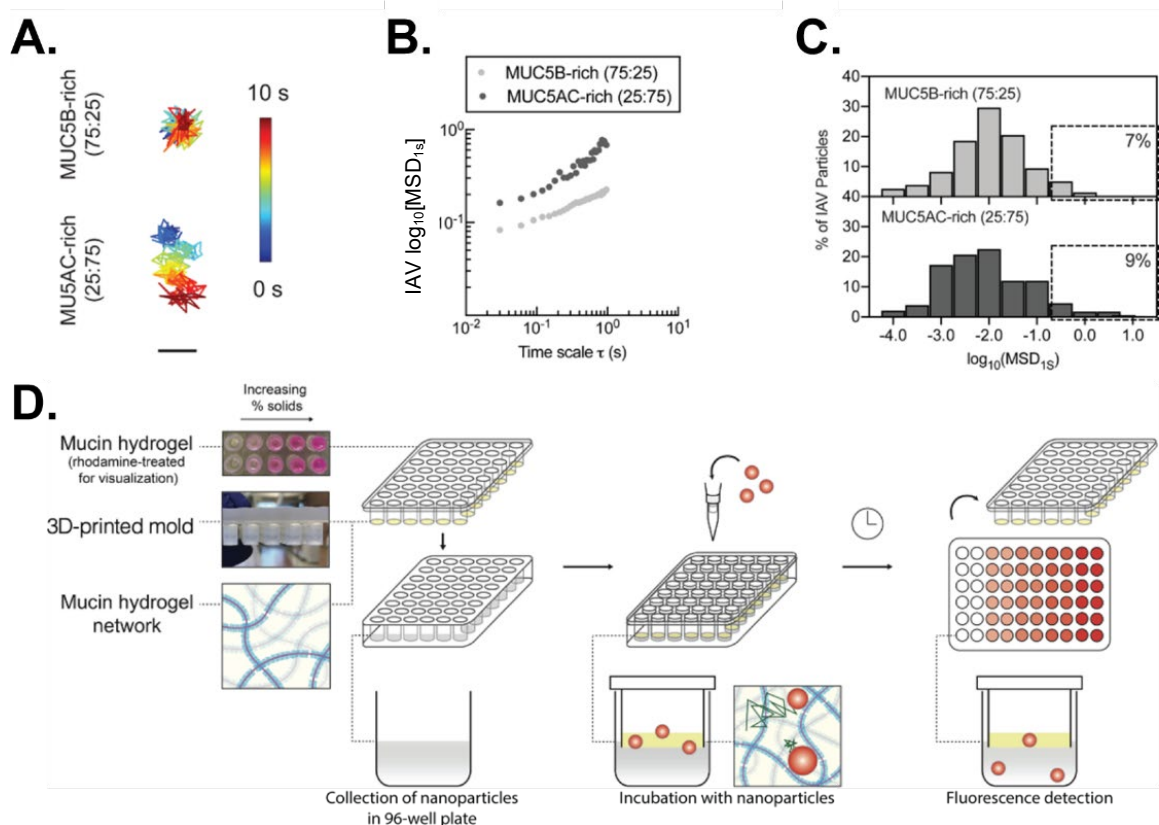


Figure 3.4. Investigation of Mucus Composition on IAV Diffusivity and a Synthetic Mucus Array. (A) Representative trace trajectories of IAV diffusion in synthetic mucus preparation of indicated MUC5B and MUC5AC compositions. Scale bar = 0.2 μm . (B) Measured $\log_{10}\text{MSD}_{1\text{s}}$ for IAV in gel compositions as in A. IAV in MUC5AC-rich gels exhibits a higher diffusivity. (C) Histogram analysis of IAV by synthetic mucus composition stratified by $\log_{10}\text{MSD}_{1\text{s}}$ values as in (A) and (B). (D) Schematic diagram of the Synthetic Mucus Array (SMA). Briefly, desired mucin compositions and cross-linking reagent are incubated in a bottomless 96-well array on parafilm until solid. Then, the SMA is removed and placed into a standard 96-well plate, allowing for analysis on fluorescent particle penetration (pictured above) or viral infectivity readouts (not pictured).

3.1.7 Discussion

In this chapter, we examined the roles of mucus microstructure and IAV-mucin adhesive interactions. While prior studies reported a lower mobility for IAV relative to comparably sized PS-NP (~120 nm) [160,291], we found that IAV displayed lower mobility

in only half of our patient mucus samples. Previous work has demonstrated rigidity-dependent diffusion of lipid and protein-based nanoparticles through biological gels where particle deformability can be tuned to enhance mobility [292,293]. Our findings therefore might be due to the semi-deformable nature of IAV particles [294] compared to rigid PS-NP, but additional work is required to explore this. Overall, however, diffusion of IAV and PS-NP was comparable when considering all samples tested. By contrast, disrupting the mucus crosslinking with the reducing agent DTT enhanced IAV diffusion through mucus due to the increased network pore size. Further, we have demonstrated that a smaller network size, as detected by PS-NP, substantially decreases IAV mobility in a synthetic mucus model with systematically varied crosslinking density. Future work with the synthetic mucus array will allow for additional functional investigations on the impact of mucus composition on IAV diffusivity as well as other respiratory viruses.

Several reports on IAV diffusion through mucus suggest interactions with mucin-associated sialic acid contribute to its transport behavior [160,163,295]. For example, it has been shown H1N1 and H3N2 IAV adhere to human lung tissue sections and salivary mucus in a sialic acid-dependent manner [200]. In addition, previous work has shown NA activity of a swine IAV facilitates its transit through porcine lung mucus [160]. Conversely, we did not find that NA inactivation reduces IAV diffusion through mucus. Indeed, we observed that for some samples IAV exhibited enhanced mobility after NAI addition relative to PS-NP. This behavior might be due to an unexpected increase in network size and therefore enhanced IAV diffusivity due to the NAI treatment (**S. Fig. 3.2A**), possibly by either direct effects of NAI on mucus structure or differences between individual donors. Ultimately, we attribute the NAI-dependent pore size differences to the varying properties of the mucus collected as there is likely a wide variation in the glycans present in human

mucus from different donors. Based on our results, it is likely IAV HA binding of mucin glycans is weak and reversible regardless of endogenous NA activity.

In natural infections, influenza virions can vary in morphology, producing a mixture of spherical and filamentous virions [296]. Recent work has also shown the impact of IAV particle morphology on transport in mucus which will be important to consider in subsequent studies [205]. Based on this prior work, IAV particles with a filamentous morphology and the potential for HA/NA polarization within the IAV envelope are more likely to engage in multivalent HA-sialic acid interactions than spherical IAV like the PR8 strain used in this work. Given that PR8 predominantly forms spherical virions, we are unable to observe the diffusion of pleomorphic IAV strains in mucus. However, we have rescued a well-characterized pleomorphic IAV strain [251,297] as well as a nearly isogenic mutant that only produces spherical particles [210,298] (**S. Fig. 3.5**). Having optimized particle collection timepoints, we will investigate the diffusivity of the pleomorphic IAV strain compared its spherical-only mutant in the context of both patient mucus samples and the synthetic mucin array.

The literature to date has generally focused on the entrapment of IAV within human mucus purely as a function of sialic-acid presentation [160,163,279]. From a more physiological perspective, our data support the rationale that the crosslinking and pore structure of mucus gels can help to protect the airway epithelium from IAV and potentially other respiratory viruses. The inflammatory response to IAV infection is known to increase reactive oxygen species production, oxidative stress, and cytokine expression resulting in acute lung injury [299]. In response to oxidative stress, the epidermal growth factor pathway, responsible for mucin hypersecretion, becomes activated leading to increased mucus concentration in the airway lumen [280,300]. In addition, prior studies have found

oxidative stress can increase the elasticity of airway mucus, attributed to the oxidation of mucin cysteine domains leading to the formation of mucin-mucin disulfide crosslinks [289]. Increased mucin concentration and mucin-mucin crosslinking due to oxidative stress might be a beneficial part of the inflammatory response towards IAV infection to hinder virus penetration through the mucus barrier. However, these potential benefits may be undermined by compromised airway clearance in mucus gels with abnormal viscous and elastic properties [301].

In summary, we have determined that IAV mobility can be limited by both the structural and biochemical features of the mucus gel network. The influence of gel network structure observed in our work bears similarity to past studies that demonstrate the size dependence of particle diffusion through mucus and other biological matrices [293,302–305]. Unlike previous reports, we have not observed significant binding of IAV to sialic acid leading to particle entrapment, indicating that PR8 IAV penetration through dense mucus is not dependent solely on NA function. As might be expected, mucus gels with pore sizes approaching the diameter of IAV are capable of physically entrapping viral particles. Steric hindrance within the mucus gel network may also influence the accessibility of sialic acid receptors to HA binding. Our results also provide a framework for direct measurement of viral particle association to mucus gels which may prove useful for future studies on respiratory viruses by our group and others in the field.

Chapter 4 : Membrane-Tethered Mucin 1 is Stimulated by Interferon and Virus Infection in Multiple Cell Types and Inhibits Influenza A Virus Infection in Human Airway Epithelium

Ethan Iverson¹, Kira Griswold¹, Daniel Song², Talita B. Gagliardi¹, Kajal Hamidzadeh¹, Mehmet Kesimer³, Sanju Sinha^{4,5}, Melissa Perry¹, Gregg A. Duncan², and Margaret A. Scull^{1,#}

¹ Department of Cell Biology & Molecular Genetics, Maryland Pathogen Research Institute, University of Maryland, College Park, MD, USA.

² Fischell Department of Bioengineering, University of Maryland, College Park, MD, USA.

³ Marsico Lung Institute, University of North Carolina, Chapel Hill, NC, USA.

⁴ Cancer Data Science Laboratory, National Cancer Institute, National Institutes of Health, Bethesda, MD, USA.

⁵ Center for Bioinformatics and Computational Biology, University of Maryland, College Park, MD, USA.

Corresponding author

Email address: scull@umd.edu

This chapter features text and data currently in submission and under revision at mBio. A preprint of the manuscript prior to revision can be found here: [306].

My contribution to this work was rescuing and preparation of all viral stocks, IHC staining of HAE with the rH3-probe, infection and fixation of IAV-infected HAE for downstream TEM processing, adaption of commercial MUC1 ELISA for use with biotinylate-IAV, MUC1-IP and associated immunoblot. I also performed replicate work of MUC1 shedding after HAE infection with IAV, replicate work of RT-qPCR analysis of MUC1 transcripts following HAE culture stimulus and infection, replication of MUC1-CT Western blot following HAE stimulus and infection. I performed IHC staining of HAE following IAV infection, IF staining of HAE following IAV infection. I also cultured, stimulated, and analyzed macrophages by Western blot. I optimized the production and quality control of CRISPR/Cas9-modified BCI-NS1.1. I performed all IAV infections and analyses on modified HAE. Additionally I helped write and edit the manuscript.

4.1.1 Abstract

Influenza A virus (IAV) causes significant morbidity and mortality in the human population. Tethered mucin 1 (MUC1) is highly expressed in airway epithelium, the primary site of IAV replication, and also by other cell types that influence IAV infection, including macrophages. MUC1 has the potential to influence infection dynamics through physical interactions and/or signaling activity, yet MUC1 modulation and its impact during viral pathogenesis remains unclear. Thus, we investigated MUC1–IAV interactions in an in vitro model of human airway epithelium (HAE). Our data indicate that a recombinant IAV hemagglutinin (H3) and H3N2 virus can bind endogenous HAE MUC1. Notably, infection of HAE with H1N1 or H3N2 IAV strains does not trigger MUC1 shedding, but instead stimulates an increase in cell-associated MUC1 protein. We observed a similar increase after type-I or -III interferon (IFN) stimulation; however, inhibition of IFN signaling during H1N1 infection only partially abrogated this increase, indicating multiple soluble

factors contribute to MUC1 upregulation during the antiviral response. In addition to HAE, primary human monocyte-derived macrophages also upregulated MUC1 protein in response to IFN treatment and conditioned media from IAV-infected HAE. Then, to determine the impact of MUC1 on IAV pathogenesis, we developed HAE genetically-depleted for MUC1, finding that MUC1 knock-out cultures exhibited enhanced viral growth compared to control cultures for several IAV strains. Together, our data support a model whereby MUC1 inhibits productive uptake of IAV in HAE. Infection then stimulates MUC1 expression on multiple cell types through IFN-dependent and -independent mechanisms that further impact infection dynamics.

4.1.2 Introduction

The respiratory epithelium encodes large and extensively glycosylated proteins, termed mucins, to maintain airway surface hydration and protect the underlying cells from environmental insults, such as respiratory viruses [14,15]. While some mucins are secreted and form a mucus gel, others – the aptly named “tethered” mucins – remain anchored to the apical epithelial cell surface, giving rise to the periciliary layer (PCL) [14,15,17]. The PCL serves as a platform for overlying secreted mucins, allowing ciliary action to propel the secreted mucus gel in a process known as mucociliary clearance (MCC) [20,56]. Additionally, tethered mucins of the PCL represent steric obstacles to impede further access to the underlying epithelium [15]. In addition to the bulky extracellular domain (ED) typical of tethered mucins, the highly abundant mucin 1 (MUC1) features a highly-conserved cytoplasmic tail (CT) that can be differentially phosphorylated [307,308] and interact with many partners including kinases and adapter proteins involved in signal transduction [17,37,38]. The presence of an autoproteolytic SEA domain upstream the transmembrane domain, in conjunction with enzymatic sheddases, can lead

to the release of the MUC1-ED domain from the MUC1-CT domain [17,32]. MUC1-CT can also be translocated to the nucleus [39–41], altogether supporting important functions outside its canonical representation among the PCL.

MUC1/Muc1 (humans/mice) has been implicated in various aspects of both bacterial and viral infections. For example, the genetic disruption of *Muc1* is associated with elevated inflammation and faster *Pseudomonas aeruginosa* clearance [37], yet results in more severe *Streptococcus pneumoniae* infection [309]. Adenoviral infection in *Muc1*^{-/-} mice is modestly increased with no significant inflammatory differences in the lung [310] and adenoviral vector gene transfer efficiency *in vitro* and *in vivo* is inhibited by MUC1/Muc1 expression [19,311], suggesting that MUC1 restricts adenovirus by acting as a physical barrier. Outside the airway, MUC1 has been shown to be an attachment factor for *Helicobacter pylori* [312] and *Salmonella enterica* [313], while the presence of MUC1 in breast milk is protective against human immunodeficiency virus transmission [314]. MUC1 has also been shown to suppress respiratory syncytial virus-induced inflammation *in vitro* by forming a negative feedback loop with tumor necrosis factor (TNF α) [315] and altered expression of MUC1 has been described in response to multiple inflammatory stimuli [316], suggesting it might play a universal and dynamic role during insult by different pathogens [317,318]. Notably, no consensus on MUC1 function or dynamics during infection is reflected in these studies.

Influenza A virus (IAV) infects the human airway epithelium (HAE) [132] and causes an estimated annual burden of 290,000-645,000 deaths worldwide in non-pandemic years [117]. To gain access to airway epithelial cells, IAV must first penetrate the secreted mucus and underlying PCL barriers. Subsequent endocytic uptake into epithelial cells is mediated through interactions between the viral attachment protein hemagglutinin and glycans with terminal sialic acid (SA) linkages on the cell surface [155]. While it is known that SA recognition heavily impacts cellular tropism and epizootic

potential [319], the extent and consequence of IAV attachment to SA on specific host proteins is unclear [320]. A recent report suggests that IAV can interact with the extracellular domain of MUC1 and that this interaction has important implications for pathogenesis *in vivo* [321]. However, it is not known if MUC1 can restrict IAV access to well-differentiated epithelial cells, or if SA-mediated interactions subvert a normally protective physical role and instead support IAV uptake. Additionally, it is not known how MUC1 expression is impacted during IAV infection of the respiratory epithelium and whether its immunomodulatory role is important in the context of IAV pathogenesis.

Here we investigate specific interactions between IAV and MUC1 in a physiologically-relevant model of HAE. Consistent with previous reports in cell lines [321], we show that IAV can interact with membrane-tethered MUC1 in HAE; however, in contrast to earlier findings, we find no evidence of IAV-mediated MUC1 shedding in several epithelial model systems. Our data instead indicate that MUC1 is upregulated in all HAE component cell types as well as primary human monocyte-derived (PMD) macrophages by soluble factors, including type I and type III interferons, produced during IAV infection. Then, using an *in vitro* HAE model system that is genetically deleted for MUC1, we demonstrate that depletion of MUC1 is pro-viral for several IAV strains, leading to enhanced IAV replication and spread.

4.1.3 The IAV Hemagglutinin Protein Binds MUC1 Isolated from HAE Apical Secretions and Co-Localizes with MUC1 During Infection

Previous work suggests that IAV can interact with MUC1 based on fluorescence microscopy and colocalization analysis in A549 cells [321]. Thus, we sought to determine if the IAV hemagglutinin protein binds MUC1 derived from an *in vitro* model of primary HAE since this system recapitulates important aspects of airway epithelial morphology

and physiology including both secreted and tethered mucin expression (**S. Fig. 4.1**) [1,15,70]. In support of a potential HA-MUC1 interaction in HAE, our initial experiments revealed recombinant, Fc-tagged H3 hemagglutinin (rH3-Fc) binding at the apical cell surface in histological cross-sections of HAE cultures in regions that also stained positive for MUC1-ED (**Fig. 4.1A**).

Notably, in HAE cultures, MUC1 can also be identified in apical secretions along with other, less abundant tethered mucins (e.g., MUC4, MUC16) [15,322]; thus, to further interrogate HA-MUC1 interaction we enriched for MUC1 in HAE secretions by immunoprecipitation with anti-MUC1-coated beads (**Fig. 4.1B**). This MUC1-enriched material was then washed and eluted off the beads before being separated by SDS-PAGE electrophoresis and transferred to a membrane, where interaction with influenza virus hemagglutinin protein was determined using rH3-Fc as a probe. Detection of rH3-Fc binding and anti-MUC1-ED reactivity in the same region of the membrane indicated a likely interaction between the viral attachment protein and this mucin molecule (**Fig. 4.1C**). MUC16, another tethered mucin that was also previously identified in HAE secretions, was detected in the total input but not in the immunoprecipitated conditions. These data support that MUC1 was further enriched from other tethered mucins and are consistent with the conclusion that detection of rH3-Fc is indicative of hemagglutinin-MUC1 binding.

Since the rH3-Fc probe represents a soluble form of HA, we next sought to determine if whole virions could interact with HAE-derived MUC1. Towards this goal, we utilized Sulfo-NHS-SS-biotin to label sucrose-purified A/Udorn/307/72, a well-characterized strain that natively possesses an H3 similar to the recombinant H3 probe and confirmed that the labeled virus (Udorn^{biotin}) retained infectivity in HAE (**S. Fig. 4.2**). We then asked whether Udorn^{biotin} could interact with MUC1 using a modified ELISA scheme (**Fig. 4.1D**). Here, MUC1 in HAE culture lysates was isolated by MUC1 capture antibody coated on the bottom of the ELISA plate. Subsequent binding of 3×10^4 PFU of

Udorn^{biotin} or biotinylated-anti-MUC1 detection antibody (provided in the ELISA kit and used as a positive control) to the immobilized MUC1 in the well was assessed using Streptavidin-HRP and the addition of HRP substrate. To control for interactions between Udorn^{biotin} and MUC1 not mediated through the viral HA, we ran a parallel condition in which Udorn^{biotin} was incubated in the ELISA well in the presence of high amounts of neutralizing anti-H3 goat serum shown to abolish all hemadsorption activity of the biotinylated virus (E. Iverson and M. A. Scull, data not shown). Udorn^{biotin} was able to support the detection of MUC1 primarily through interactions with HA, as indicated by the near complete loss of reactivity after incubation with neutralizing antibodies (**Fig. 4.1E**). Together with our data in Figure 1C, these results indicate that the hemagglutinin of IAV can mediate interactions with purified forms of HAE-derived MUC1.

Finally, to determine if the influenza virus-MUC1 interaction occurs during infection in the context of the native HAE microenvironment, we inoculated HAE cultures with $\geq 5 \times 10^5$ plaque forming units (PFU; approximate multiplicity of infection (MOI) of 10) of A/Udorn/307/72 and subsequently chilled the cultures to 4°C so as to irreversibly stabilize virus adsorption and restrict cellular entry [213]. Next, we performed transmission electron microscopy with immunogold labeling to detect IAV H3 as well as MUC1-ED, allowing us to observe potential colocalization of these two molecules prior to cellular uptake. MUC1 was once again identified at the apical surface, primarily localized to microvilli, as previously described [15]. IAV was also found in close proximity to immunogold-labeled MUC1 (**Fig. 4.1F-I**), in line with our *in vitro* interactions and prior work in A549 cells [321]. Taken together, our results suggest that influenza virus interacts with MUC1 during the early stages of infection in a physiologically-relevant system that recapitulates the extracellular environment in the airway.

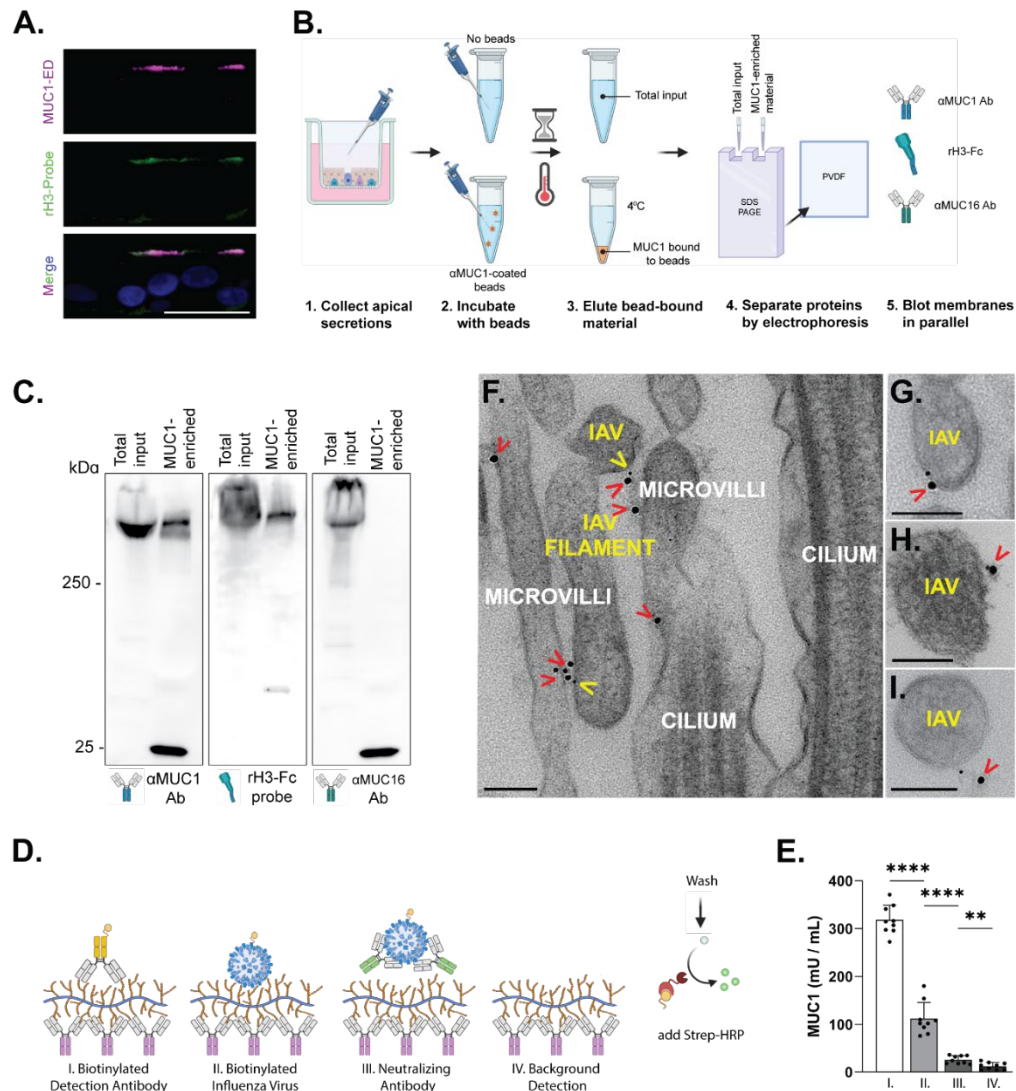


Figure 4.1. IAV Hemagglutinin and IAV Bind HAE-Derived MUC1 and Co-localize During Infection. (A) IHC of normal HAE, immunostaining for the extracellular domain of MUC1 (MUC1-ED, purple), with a trimerized hemagglutinin probe (rH3-Probe, green), and the merged channel with nuclei (blue). Scale bar = 20 μ m. (B) Schematic diagram of HAE wash collection, immunoprecipitation of MUC1-containing material, gel electrophoretic separation of bead-bound material, and subsequent Western blot probes used in (C). In (C), crude HAE wash (total input) and MUC1-IP material (MUC1-enriched) were separated by SDS-PAGE in triplicate and probed as indicated. (D) Cartoon schematic of modified MUC1 ELISA protocol utilizing biotinylated Udorn with indicated conditions (Roman numerals) and (E) corresponding ELISA results. Error bars indicate standard deviation. (F-I) Transmission electron microscopy of HAE after adsorption with A/Udorn/307/72(H3N2) influenza virus. Images were taken from (F, G, and I) primary HAE and (H) an immortalized HAE cell line (BCi-NS1.1; [93]). MUC1 (indicated by red carets) and H3 (yellow carets) were detected with 18nm and 6nm gold nanoparticle-conjugated antibodies, respectively. Scale bars = 100 nm. All data are significant where indicated (* $p < 0.05$, ** $p < 0.01$, *** $p < 0.001$, **** $p < 0.0001$). Diagrams in (B) and (D) created with BioRender.com.

4.1.4 IAV Replication in HAE is Not Associated with an Increase in Soluble MUC1

Given our results indicating HAE-MUC1 interacts with IAV hemagglutinin, we next sought to determine the consequence of this interaction. Previous work in CHO cells suggested that the ectodomain of ectopically-expressed MUC1 could act as a releasable decoy that is shed upon IAV binding to prevent subsequent infection of underlying cells [321]. To determine whether MUC1 is shed during viral challenge in the context of the airway PCL, we inoculated primary, well-differentiated HAE cultures with either A/Udorn/307/72 or another well-characterized virus, A/PR/8/34, which possesses a H1 hemagglutinin, and quantified MUC1 and infectious virus in apical washes 24 hours post-infection (hpi; **Fig. 4.2**). Surprisingly, in contrast to previous observations, we found that neither A/PR/8/34 nor A/Udorn/307/72 infection resulted in a significant change in soluble MUC1 levels relative to mock-infected cultures despite reaching mean titers of 1.9×10^6 and 2.4×10^6 , respectively.

To determine if a lack of MUC1 shedding after IAV challenge was an HAE-specific phenomenon, we executed a similar experiment in A549 cells expressing endogenous MUC1. Following a one-hour incubation at 4°C to allow viral particles to bind to the cell surface, we removed the inoculum, returned the cultures to 37°C, and quantified MUC1 and infectious virus in cell culture supernatants 24 hours later (**S. Fig. 4.3**). Similar to our HAE results, infection in A549 cells with A/PR/8/34 or A/Udorn/307/72 did not trigger an increase in MUC1 shedding; in fact, a significant decrease in soluble MUC1 was observed following inoculation with A/Udorn/307/72. These data corroborate our results in HAE and together suggest that MUC1 expressed endogenously in human airway cells is not shed during IAV challenge.

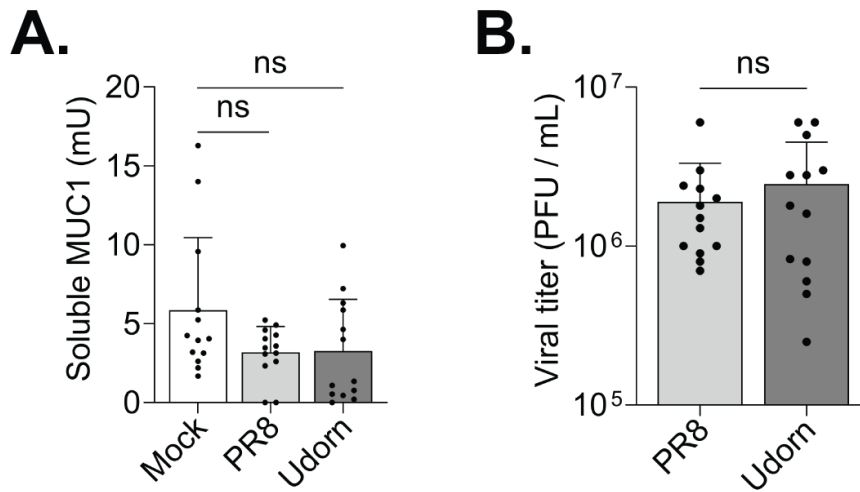


Figure 4.2. IAV Replication in HAE is not Associated with Increased Soluble MUC1. HAE cultures were infected with 5×10^4 PFU of either A/PR/8/34 or A/Udorn/307/72 or mock-infected. After 24 hours, apical HAE compartments were washed with PBS which was used to determine (A) soluble MUC1-ED by ELISA and (B) viral titer by plaque assay. Results shown are from four independent experiments, each performed in HAE cultures derived from a unique donor. Experimental results were analyzed by Mann-Whitney U test compared to mock conditions or each other (ns = not significant). Error bars indicate standard deviation.

4.1.5 Cell-Associated MUC1 Levels are Upregulated During IAV Infection and After Interferon Treatment

As the lack of an increase in soluble MUC1 levels following infection of human airway cells was unexpected, we sought to further characterize MUC1 dynamics in HAE after IAV challenge. Since previous reports have described an increase in MUC1 protein following IFN γ exposure in other systems [323], and IAV infection of HAE triggers both type I and type III IFN [67], we quantified MUC1 gene expression and cell-associated MUC1 protein levels following IAV infection, or after treatment of HAE with IFN β , IFN $\lambda 3$, or TNF α (previously implicated in upregulating MUC1 [317,324]). Neither type I or type III IFN treatment (**Fig. 4.3A** and **4.3B**) nor A/PR/8/34 infection (**Fig. 4.3C**) triggered an

increase in MUC1 transcripts above mock-treated controls, let alone a response typical of well-characterized interferon stimulated genes (**S. Fig. 4.4**). However, type I and type III IFN, along with IAV, were able to stimulate production of MUC1 protein similar to that seen with TNF α (**Fig. 4.3D**). Furthermore, IAV-mediated upregulation of MUC1 protein was at least partially IFN signaling-independent, as the addition of a Janus tyrosine kinase (JAK)1 inhibitor did not abolish increased MUC1 protein expression as it did for MX1, a marker for IFN signaling (**Fig. 4.3E**).

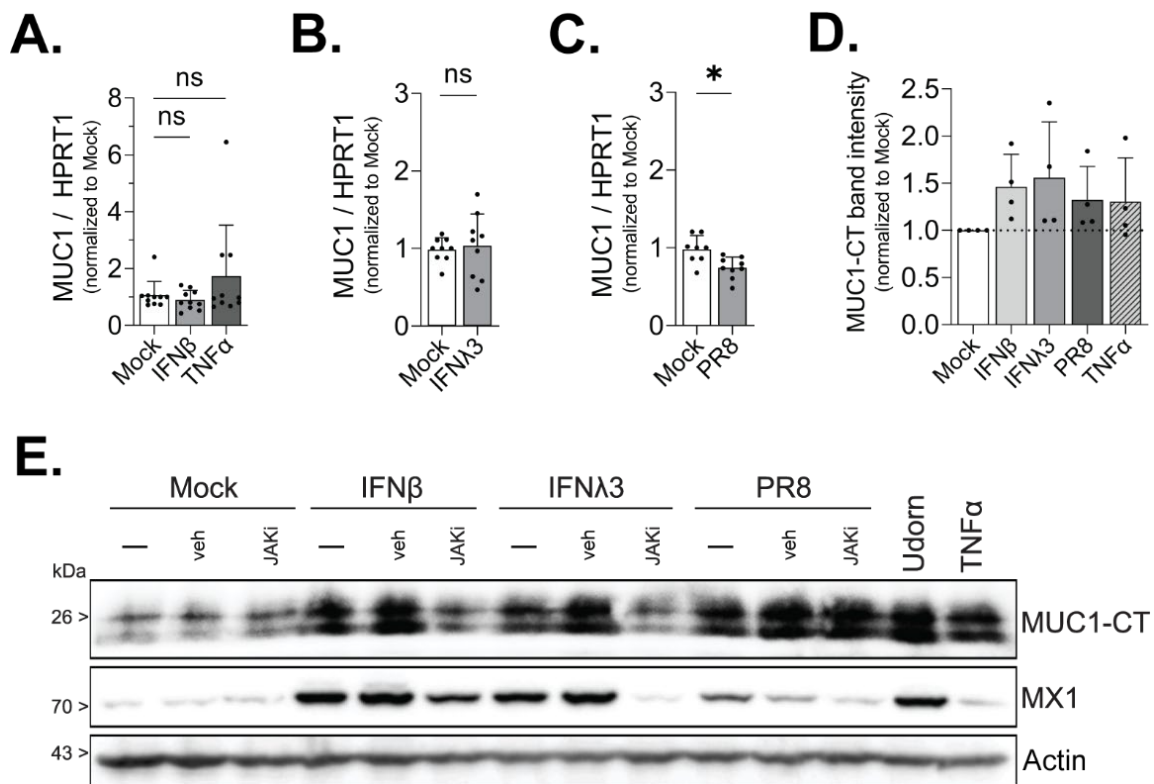


Figure 4.3. Cell-associated MUC1 Levels are Upregulated During IAV Infection and Interferon Treatment. HAE were (A) and (B) stimulated as indicated or (C) infected with IAV and MUC1 expression quantified by qPCR after 24 hours of treatment. In (D) HAE were stimulated as indicated or infected with PR8 as in (A-C) for 24 hours, protein lysate collected, and MUC1 expression quantified by Western blot for MUC1-CT. MUC1-CT band intensity was analyzed by densitometry relative to actin band intensity. In (E), HAE were stimulated with IFN or IAV as indicated (-), in the presence of JAK inhibitor Ruxolitinib (JAKi), or with DMSO as a vehicle control (veh). After 24 hours, lysate was collected and analyzed by Western blot for MUC1-CT, MX1, or actin. In (A-C), results are representative of three biological replicates, and the densitometry analysis of (D) is representative of four biological replicates, including select lanes in (E), all of which are comprised of at least two unique HAE donors. Error bars indicate standard deviation. All experimental results were analyzed by Mann-Whitney U test compared to mock conditions and significant where indicated (* $p < 0.05$).

In order to visualize which cells were expressing MUC1 after IFN challenge or IAV infection, we fixed cultures either 6 and 24 hours post-IFN treatment or 24 and 48 hpi and stained for MUC1 using standard immunohistochemical approaches. Surprisingly, despite a lack of protein expression in basal cell populations at baseline and a lack of mRNA

upregulation after IFN treatment (**S. Fig. 4.1** and **Fig. 4.3A**), we observed MUC1 protein in all HAE component cell types following IFN β stimulation (**Fig. 4.4A, left panel**). Similarly, infection of HAE with A/Udorn/307/72 (500 PFU, approximate MOI of 0.01) was associated with ubiquitous MUC1 protein expression throughout the epithelium by 48 hpi (**Fig. 4.4A, right panel**). Inoculation of HAE cultures with a higher dose of A/Udorn/307/72 (50,000 PFU, approximate MOI of 1) followed by *en face* immunofluorescence staining 24 hpi (**Fig. 4.4B, C**) supported these findings, showing a significant increase in both MUC1 fluorescence intensity (**Fig. 4.4D**) and MUC1-positive area (**Fig. 4.4E**) across the apical surface as compared to uninfected baseline conditions. Together, our data show MUC1 protein broadly expressed in HAE after IFN exposure and IAV infection.

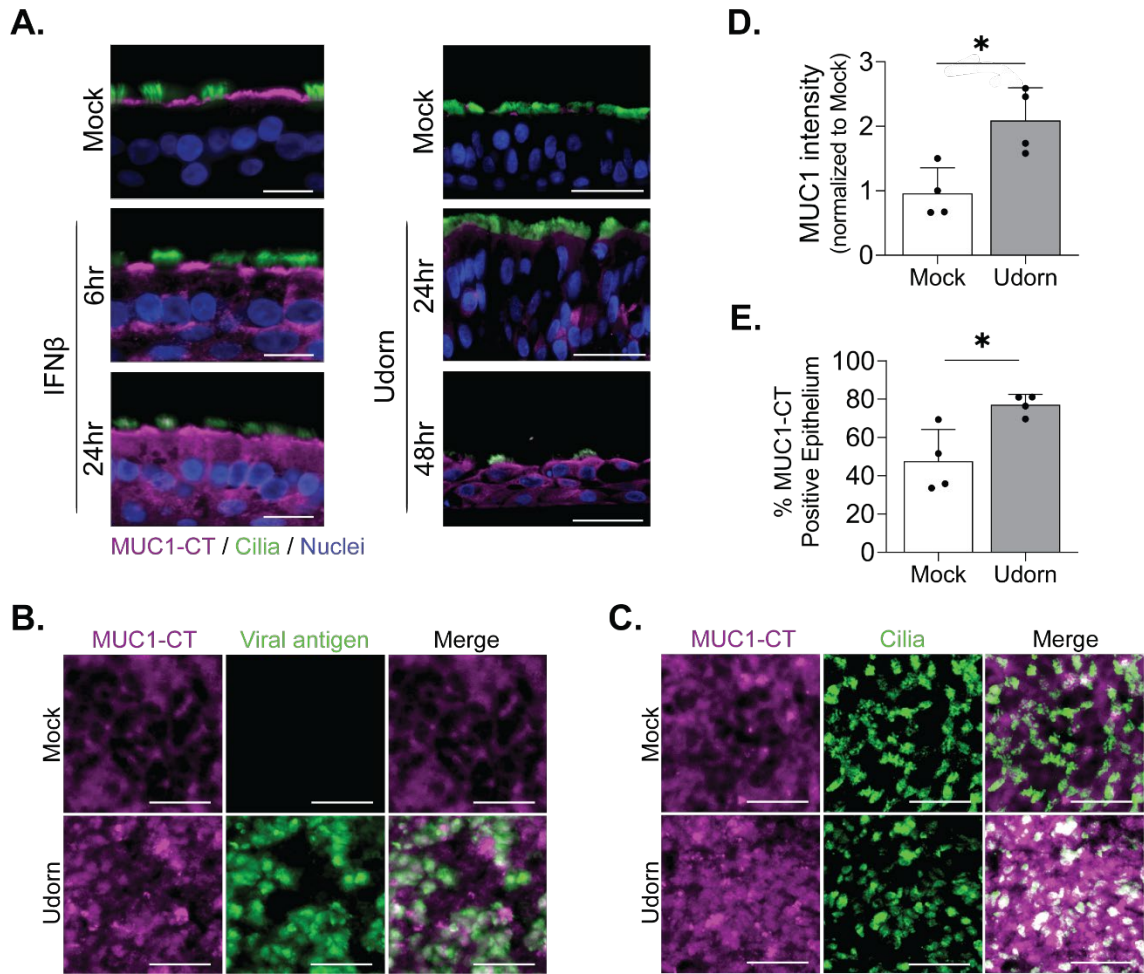


Figure 4.4. Type 1 IFN and IAV Broadly Upregulate MUC1 Expression Across HAE. (A) HAE were stimulated with IFN β or mock conditions (left) or infected with Udon (5×10^2 PFU, right) and at indicated time points fixed for immunohistochemical detection of MUC1-CT (purple), acetylated alpha-tubulin (cilia marker; green), and nuclei. In (B-E), HAE were infected with IAV (5×10^4 PFU) and stained *en face* for MUC1-CT (purple), (C) viral antigen (NP, green), and (D) cilia cell marker (acetylated alpha tubulin; green). The (D) mean intensity or (E) total staining area of MUC1-CT staining was quantified by FIJI and analyzed by Mann-Whitney U test compared to mock condition, indicating significance (* $p < 0.05$). Results in (D) and (E) are representative of four biological replicates across two unique HAE donors. Error bars are indicative standard deviation. Scale bars in A = 20 μ m and for (B) and (C) = 25 μ m.

4.1.6 Soluble Factors Secreted by HAE During IAV Infection Upregulate MUC1 on Primary Human Monocyte-Derived Macrophages

Beyond epithelial cells, MUC1 is known to be expressed by cells of the hematopoietic lineage [325–327], including macrophages, and this expression can modulate their phagocytic activity [323]. As macrophages play an important role during IAV infection [328,329] and because we observed elevated MUC1 protein during IAV infection and after IFN treatment across HAE component cell types, we next determined the impact of host- and viral-derived factors likely present in epithelial tissue during IAV infection on MUC1 expression in macrophages. Following differentiation with granulocyte-macrophage colony-stimulating factor (GM-CSF; to better achieve alveolar-like macrophages) [330–332], we stimulated PMD macrophages with Poly I:C (a viral double-stranded RNA mimetic), inflammatory cytokine TNF α , type I interferon (IFN β), or type III interferon (IFN λ 3). Both Poly I:C and IFN β resulted in a strong upregulation of MUC1 protein similar to the IFN γ (type II IFN) and LPS combination treatment [323] while IFN λ 3 and TNF α induced detectable, albeit weak, upregulation (**Fig. 4.5A** and **4.5B**).

To further assess whether MUC1 upregulation was mediated by soluble factors produced in the context of infection, we infected HAE with 5×10^4 PFU (approximate MOI of 1) of A/Udorn/307/72 and then transferred the virus-free basolateral medium [333] to naïve PMD macrophages (**Fig. 4.5C**). While MUC1 protein was elevated by unspent and mock-conditioned medium, these levels were markedly increased in cultures receiving IAV-conditioned supernatant at both 24 and 48 hours (**Fig. 4.5D** and **4.5E**). These data indicate that IAV infection of HAE leads to the secretion of soluble factors that have the potential to increase MUC1 levels on multiple cell types during infection *in vivo*.

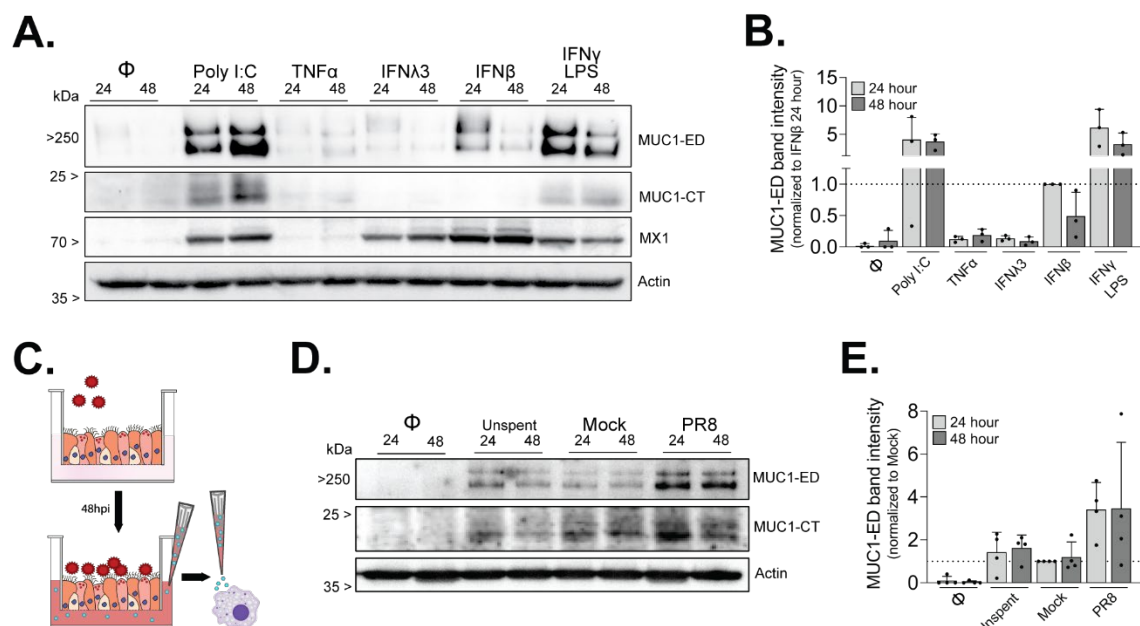


Figure 4.5. Primary Human Monocyte-Derived Macrophages Upregulate MUC1 in Response to IFN and Soluble Factors Produced From IAV-infected HAE. GM-CSF-derived PMD macrophages were either untreated (Φ) or stimulated as indicated for 24 or 48 hours. (A) Cell lysates were then collected and analyzed by Western blot for MUC1-ED, MUC1-CT, MX1, and actin. (B) Densitometry across conditions reported in A. Data represent MUC1-ED relative to actin for each sample, normalized to IFN β / 24hr. (C) Cartoon schematic of experiment conditions in (D) where PMD macrophages were stimulated with freshly prepared, mock-conditioned, or IAV-infected HAE-conditioned basolateral media before lysate collection and Western blot analysis for MUC1-ED, MUC1-CT, and actin. HAE-conditioned basolateral media used in (D) was collected from independent experimental replicates across unique HAE donors. (E) Densitometry across conditions reported in (D). Data represent MUC1-ED relative to actin for each sample, normalized to Mock / 24hr. Densitometry reported in (B) and (E) represent biological replicates across three and four unique donors, respectively, where error bars indicate the standard deviation.

4.1.7 Generation of HAE Cultures Lacking MUC1

Given the ability of IAV to bind MUC1 during infection, and our observed changes in MUC1 protein dynamics in both HAE and PMD macrophages as a consequence of IAV infection, we next sought to determine the impact of MUC1 on IAV replication. We utilized CRISPR/Cas9-mediated genome editing to achieve well-differentiated HAE cultures that

were genetically knocked-out (KO) for MUC1. To do so, we cloned a single guide (sg)RNA targeting MUC1 (exon 5; **Fig. 4.6A**), or no known sequence (non-targeting control), into a GFP-expressing lentiviral vector that also encodes the Cas9 nuclease, transduced immortalized human airway epithelial cells (BCi-NS1.1; [98]), and sorted for GFP-positive cells prior to differentiation. Our data demonstrate on-target editing (**Fig. 4.6B**) and subsequent analysis using the Inference of CRISPR Edits (ICE) algorithm [334] revealed 87% of alleles were edited in differentiated cultures which correlated with a reduction in total MUC1 protein (**Fig. 4.6C**). We observed a lack of overt histopathology in differentiated cultures (**Fig. 4.6D**); however, compared with control cultures, MCC was significantly reduced in MUC1-depleted cultures (**Fig. 4.6E**). Nonetheless, overall, MUC1 was not critical for HAE differentiation or survival, allowing for mechanistic dissection of its role in HAE.

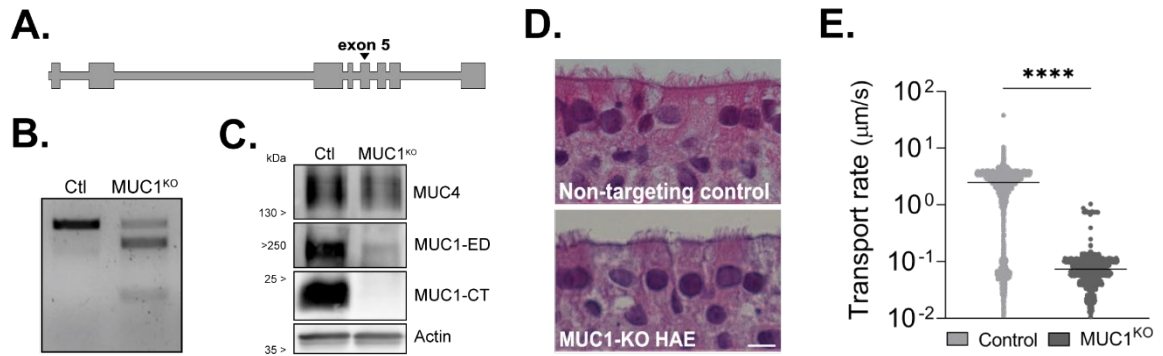


Figure 4.6. Establishment and Characterization of Immortalized HAE Depleted for MUC1. Immortalized airway epithelial BCI-NS1.1 cells were transduced with CRISPR/Cas9 and sgRNA targeting (A) MUC1 exon 5 for protein depletion (MUC1KO) or without predicted targeting site (Ctl / Control). (B) Genomic DNA was extracted and used in a T7 endonuclease I cleavage assay demonstrating editing at the target site. (C) After differentiation, total HAE lysate was collected, separated by PAGE, and blotted for non-targeted tethered mucin MUC4 (extracellular domain), MUC1-ED, MUC1-CT, and actin. (D) H&E stained, histological sections of paraffin embedded cultures show normal ciliated epithelium. Scale bar = 20 μ m. (E) Fluorescent microparticles were applied apically to indicated cultures to determine mucociliary transport rate. The median transport rate is indicated by a horizontal bar. MCC between culture types was analyzed by Mann-Whitney U test, indicating significance (**** $p < 0.0001$).

4.1.8 IAV Challenge in HAE Lacking MUC1 Reveals Altered Infection Dynamics

To determine how MUC1 depletion would impact IAV infection dynamics, we inoculated both MUC1 KO and control HAE cultures with 500 PFU (approximate MOI of 0.01) A/Udorn/307/72 to allow for multiple rounds of infection and monitored both viral growth kinetics as well as spread throughout the culture by *en face* staining for viral antigen. Viral titers were significantly higher in MUC1 KO cultures compared with control cultures at both 12 and 24 hpi; however, this difference was lost by 48 hpi (**Fig. 4.7A**). These data were consistent with immunostaining results that revealed a limited number of viral antigen-positive cells in control cultures at 12 hpi, while all MUC1 KO cultures had resolvable foci indicative of multicycle replication by this same time point (**Fig. 4.7B**). To

assess whether IAV was better able to initiate successful infection of MUC1 KO cultures, we tabulated the number of viral antigen-positive foci on predetermined regions of infected cultures 12 hpi. MUC1 KO cultures had significantly more resolvable foci compared with control HAE cultures (**Fig. 4.7C**). We further expanded this analysis to assess the area of each identified foci, finding that IAV foci were larger in MUC1 KO cultures (**Fig. 4.7D**). In line with these observations, MUC1 KO cultures also had a significantly greater percentage of viral antigen-positive epithelium at 24 hpi (**Fig. 4.7E**). By 48 hpi, both sets of cultures were extensively infected (**Fig. 4.7B** and **Fig. 4.7E**) and the integrity of the apical layer was severely compromised with many regions entirely absent, indicating exhaustive infection in the culture and cytopathic effects (**S. Fig. 4.7**).

As the SA-binding capability of IAV is critical in mediating its endocytic uptake [155], and as we have previously only explored the well-characterized lab strain A/Udorn/307/72, we sought to address whether MUC1's anti-IAV functionality extends to more recent clinical isolates and A/Udorn/307/72 with altered SA-binding preferences. To address this question, we selected two viruses representing a H3N2 (A/Perth/16/09) and a H1N1 (A/California/04/09) circulating in humans in 2009. Additionally, we created two sets of mutations in the background of A/Udorn/307/72 (capable of binding to both α 2-3- and α 2-6-linked SA) which lead to enhanced recognition of either α 2-3- (HA: L226Q / S228G) or α 2-6-linked (HA: E190D) SA [161,162]. MUC1 KO and control HAE were infected as before and both viral titers in the apical compartment as well as the frequency of infected cells were assessed at 24 hpi. As we observed for A/Udorn/307/72 in **Figure 4.7B**, all viruses displayed enhanced spread in MUC1 KO cultures compared to control cultures (**Fig. 4.7F**). Furthermore, in congruence with our earlier results, all viruses replicated to higher infectious titers in MUC1 KO cultures (**Fig. 4.7G**) although the magnitude of this difference varied between viruses. Together, these results indicate that

in our experimental conditions, MUC1 is not required for initial attachment in HAE and moreover that its loss leads to enhanced viral replication and spread, particularly at early time points (**Fig. 4.7A** and **4.7G**).

To directly assess whether MUC1 impedes initial uptake of IAV in HAE, we inoculated control and MUC1 KO HAE cultures with 5,000 PFU of A/Udorn/307/72 (approximate MOI of 0.1) for 30, 60, or 120 minutes. After the elapsed time, we removed the inoculum and allowed replication to proceed up to 12 hpi in the presence of the neuraminidase inhibitor, zanamivir. These conditions were established to facilitate accumulation of viral antigen in initially-infected cells, but prevent further spread. We then determined the frequency of successful infection events within each inoculation time frame in the presence or absence of MUC1 by *en face* staining for viral nucleoprotein (NP) and quantifying NP+ foci in predetermined fields of view, as in **Figure 4.7C**. Compared to control cultures, MUC1 KO cultures showed more NP+ foci, and this difference was best illustrated with the shortest incubation time of 30 minutes (**Fig. 4.8**), supporting the hypothesis that MUC1 significantly delays the productive uptake of IAV.

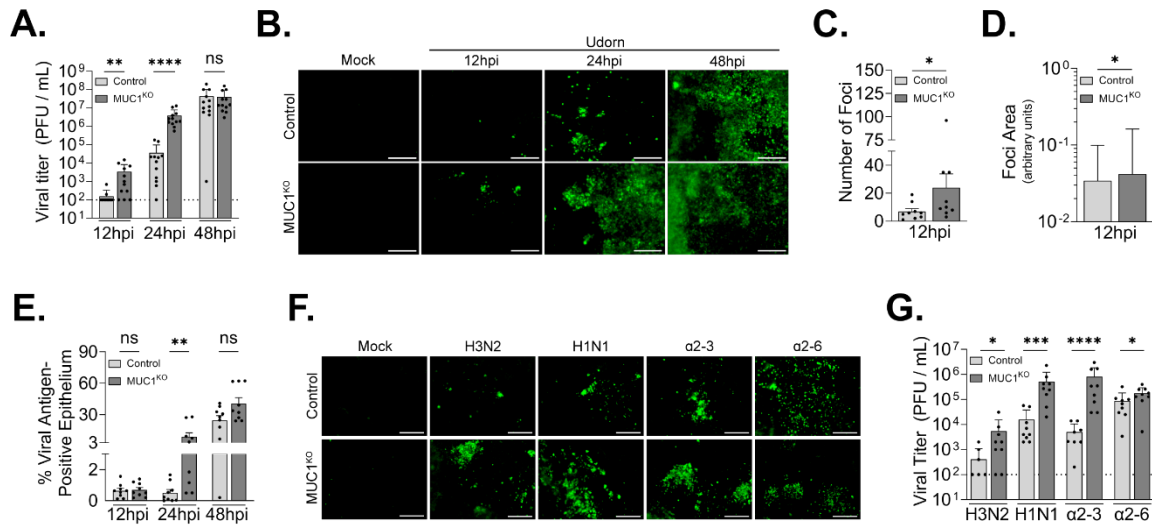


Figure 4.7. Infection in HAE Lacking MUC1 with Multiple IAV Strains Reveals Enhanced Viral Spread. Well-differentiated control or MUC1^{KO} HAE cultures were infected with indicated IAV strains at a low multiplicity of infection (500 PFU). (A-E) At the indicated time points, cultures were washed apically with PBS for (A) viral titer determination, subsequently fixed, and (B) stained en face for viral NP antigen. Viral antigen immunofluorescence signal at pre-determined fields of view from HAE was analyzed for the (C) total number of fluorescent foci per individual HAE culture and (D) signal area of contiguous viral antigen (i.e., adjacent infected cells) by culture type. (E) The total viral antigen signal area per culture reported by collection time point. In F and (G), cultures were infected with indicated viruses as before and at 24 hpi the apical surface was washed with PBS to (G) determine viral titer, and fixed to be (F) stained for viral NP antigen. Viruses used: H3N2, A/Perth/16/09; H1N1, A/California/04/09; α2-3, A/Udon/307/72 with HA: L242Q / S244G; α2-6, A/Udon/307/72(H3N2) with HA: E206D. The results of three experimental replicates in (C), (D), and (E) were determined using ImageJ and all results analyzed by Mann-Whitney U test. Results in (A) and (G) are from four and three experimental replicates, respectively. All data are significant where indicated (* $p < 0.05$, ** $p < 0.01$, *** $p < 0.001$, **** $p < 0.0001$). Error bars indicate the standard deviation. Scale bars = 100 μm.

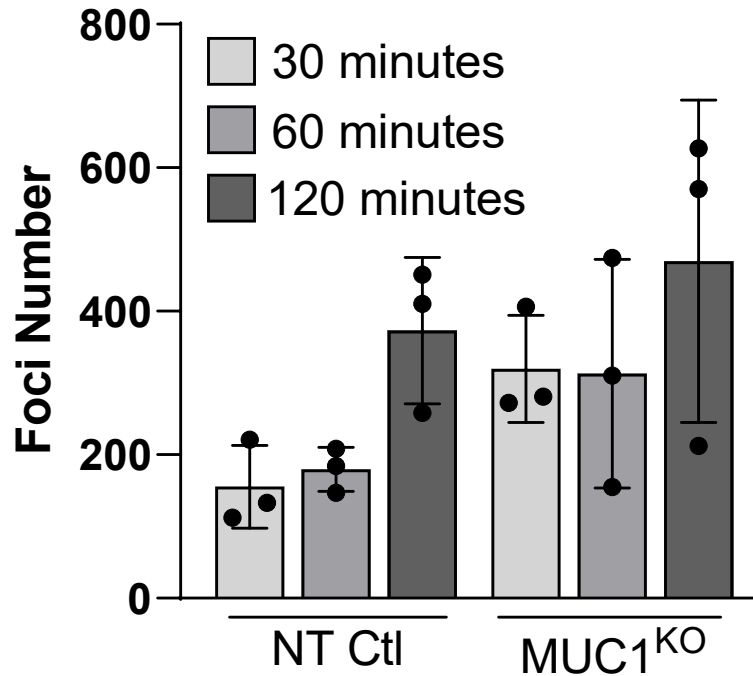


Figure 4.8. HAE Lacking MUC1 Exhibit Rapid IAV Uptake. Well-differentiated non-targeting control (NT Ctl) and MUC1^{KO} cultures were inoculated with 5×10^3 PFU of Udorn for the indicated time points. At which point the inoculum was removed, cultures briefly washed with PBS, and 1,250 nM of zanamivir (50 μ L PBS, apically; 500 μ L normal media, basolaterally) applied to prevent secondary infections. The infection was allowed to proceed for 12 hours prior to fixation and immunostaining for viral antigen (NP). Fluorescent foci were quantified from predetermined fields of view and the values for each culture were plotted. Data representative of one experimental replicate. Pairwise comparisons of each time point were deemed non-significant when analyzed by Mann-Whitney U test. Error bars indicate the standard deviation.

4.1.9 Discussion

It has been demonstrated that MUC1 plays an important, pathogen-specific, and potentially multifaceted role during respiratory infection [37,309,315,321,323]. MUC1 is an abundant constituent of the PCL where its extracellular domain contributes to airway surface hydration and its cytoplasmic domain has been shown to influence a variety of cellular signaling pathways that modulate the immune response [316,335], cell survival [336,337], and cancer progression [338]. Additionally, MUC1 expression and

phosphorylation state depend on external inflammatory stimuli [317,318]. Based on our previous work [322] and that of others [321,323], it is clear that MUC1 plays an important role during IAV infection. However, the nature of this role is poorly understood, and prior research was done in cell culture systems lacking a well-developed glycocalyx or in mice, where mucin orthologs exhibit incomplete homology with their human counterparts. Thus, we sought to explore MUC1-IAV interaction, dynamics of expression, and overall impact on IAV infection in a physiologically-relevant *in vitro* model of human airway epithelium.

Our results support a direct interaction between IAV and endogenous MUC1 during infection in HAE, extending previous findings that demonstrated colocalization of IAV with MUC1 on the surface of A549 cells [321]. Notably, MUC1-ED, the large extracellular domain of MUC1, is capable of dissociating from MUC1-CT through the autocatalytic SEA-module in response to external stimuli [32,339] and it has been previously suggested that this cleavage domain facilitates release of MUC1-ED upon interaction with IAV in the airway lumen [321]. However, we did not detect an increase in soluble MUC1-ED levels after IAV infection in both HAE and A549 cells, suggesting that IAV binding to MUC1-ED does not induce its shedding in systems with endogenous expression with or without a dense glycocalyx.

Surprisingly, we found that type I and type III IFN can upregulate cell-associated MUC1 protein in HAE despite no significant increases in MUC1 mRNA levels. These data hint at the possibility whereby some MUC1 expression is regulated through a post-transcriptional mechanism under these conditions. IAV upregulation of MUC1 protein in HAE was not exclusively dependent on IFN signaling, indicating multiple soluble factors produced during infection may contribute to elevated MUC1 expression. At least part of this increased expression was due to MUC1 upregulation at the apical surface though broad expression of MUC1 across all HAE component cell types after IAV infection and IFN stimulation further indicates that MUC1 expression is nearly ubiquitous across the

epithelium. While upregulation at the apical surface likely contributes to barrier function, expression here and in other cells types (e.g., basal cells) may serve alternative roles, potentially suppressing inflammation [335], and/or priming for epithelial repair in response to damage [38,338,340].

As macrophages play a key role during IAV infection [328,329] and previous work demonstrated that macrophages can express MUC1 in response to type II IFN [323], we explored whether IFN produced during IAV infection [67] could induce MUC1 in PMD macrophages. We show here that, in addition to HAE, PMD macrophages upregulate MUC1 following type I and type III IFN stimulation. While literature on the human monocyte response to type III IFN is conflicting [341]; human monocyte-derived macrophages and *ex vivo* human macrophages are capable of responding to type III interferon [341–343], which is consistent with our observations across multiple donors. Moreover, these PMD macrophages upregulate MUC1 in response to soluble factors produced by infected HAE. These results suggest that sites of infected epithelium might induce MUC1 expression in local macrophages as well as potentially other immune effector cells that have been shown to at least conditionally express MUC1 [325–327]. Interestingly, the banding pattern of MUC1-ED as expressed in PMD macrophages suggests an altered glycosylation state. As the expression [323] and glycosylation state [344] of MUC1 can both independently influence uptake of foreign material in different cellular contexts, further investigation should be undertaken to explore cell-specific impacts of MUC1 expression during IAV infection.

We have also established a MUC1-depleted HAE system through CRISPR/Cas9 technology. Others have established similar workflows [99,101] which offer the powerful ability to genetically manipulate otherwise intractable primary human tissue. Our characterization of these immortalized KO cultures reveals robust protein depletion as well as no gross morphological pathology. Additional functional characterization, however,

revealed that MUC1-depleted cultures displayed markedly lower MCC compared with non-targeting control cultures. As the PCL contributes to airway hydration and therefore proper secreted mucus mobility [14,15,17], it follows that MUC1 depletion could negatively affect this capability. It is also possible that loss of MUC1 alters other factors which impact MCC, such as baseline secreted mucin expression, which were not measured in this study. Future studies on air surface liquid characteristics such as PCL density and/or height, combined with other mucus steady state kinetics (e.g., secreted mucin expression) will better delineate the contribution MUC1 and other tethered mucins make toward overall mucociliary function. The HAE system we utilized here is one of several *in vitro* models that offer the ability to probe the mucosal interface which has been difficult to study in normal 2D tissue culture systems [1].

In our HAE system depleted for MUC1, we found that IAV growth kinetics are increased over control cultures, particularly at 12 and 24 hpi. By the earliest time point of 12 hpi, MUC1 depleted cultures had detectable viral titer whereas the majority of control cultures were below the limit of detection. Additionally, not only was the number of foci detectable by *en face* immunofluorescence significantly higher, but there was also clear evidence of multicycle replication visible as early as 12 hpi (the earliest time point investigated) in MUC1 KO cultures compared to control cultures. Since IAV can produce new virions as early as 6 hours [345], this implies that there is a significant delay in both the timing and success rate of productive infection initiation in control cultures relative to MUC1-depleted cultures. Indeed, our results from **Figure 4.8**, while not significant and in need of replication, suggest that the enhanced replication and spread of IAV in MUC1-depleted cultures is from the more rapid uptake of viral particles. This is consistent with previous reporting whereby tethered-mucin analogs slow the kinetics of viral attachment to membrane-bound receptors [346]. When considering the native airway environment, such a dramatic delay in uptake could be seen as a greatly increased rate of failure to

establish an infection. We note that in the HAE culture system there is no true clearance resultant from MCC as the secreted mucus layer and its components are transported over the same regions of the culture endlessly.

Consistent with other findings [321], we found that IAV can interact with MUC1, although its absence does not seem to preclude productive IAV uptake. Indeed, as loss of MUC1 enhances viral replication, it is possible that MUC1 may not only be dispensable for initial attachment but in fact may counteract subsequent productive virion adsorption and possibly endocytic entry as well. Importantly, recent work with Muc1 knockout mice has similarly shown that the loss of Muc1 enhances the rate IAV replication, though this did not impact the cumulative viral load [347].

One current model for IAV uptake suggests that virions rely on multivalent interactions with sialylated host proteins and glycolipids to deform local membrane orientation and subsequently trigger endosomal uptake [206,207]. While neuraminidase is normally thought of as a mechanism to avoid virion aggregation and inhibition by secreted mucins [160], recent work has additionally highlighted its importance at this early entry step at or near the host cell membrane [203,205]. In this model, tethered mucins support virion clearance through air-surface liquid hydration and MCC [14,15], but additionally as large constituents of the PCL, also sterically block and, when sialylated, compete with productive virion attachment to membrane-adjacent sialylated attachment sites [14,15]. Our results utilizing wild type Udorn (that binds both α 2-3- and α 2-6-linked SA) and the mutant Udorn L226Q / S228G and E190D viruses possessing altered SA-binding profiles indicate that MUC1 can inhibit IAV replication regardless of this receptor preference. Notably, the α 2-6-linked SA-binding Udorn mutant (E190D) displayed a much smaller difference in replication between MUC1 KO and control cultures relative to both the α 2-3-linked SA-binding mutant (L226Q / S228G) and wild-type Udorn. A preference for α 2-3-linked SA might be more inhibited by MUC1 relative to a mixed or α 2-6-linked

dominant binding profile. However, compared to wild-type Udorn, both SA-binding mutants yielded lower titers at 24 hpi in MUC1 KO cells. Previous work has shown that HA receptor binding preference fitness is also significantly reliant on epistatic balance even between residues outside the receptor binding domain [348] which can confound conclusions about MUC1's influence on these mutants. Additionally, MUC1 significantly inhibited the replication of both H3N2 and H1N1 clinical isolates. H3N2 and H1N1 viruses have converged in their human receptor preferences for α 2-6-linked SA-containing glycoconjugates [349], though more modern drifted H3N2 variants might have continued to diverge in this regard [158]. Both of these clinical isolates display a wider degree of enhanced replication in MUC1 KO relative to control cultures (1.1 and 1.5 log scale difference for A/Perth/16/09 and A/California/04/09, respectively) compared to the α 2-6-linked SA-binding Udorn mutant (0.3 log). It is also possible that preference for the carbohydrate core in addition to the terminal sialylated moiety further influences the inhibitory function of MUC1. Nonetheless, work on artificial tethered mucin analogs has shown that both sialylated and unsialylated artificial tethered mucins can inhibit productive interactions with gangliosides and delay IAV fusion events, respectively [346]. Together these results suggest that, regardless of receptor binding, MUC1 can significantly inhibit IAV spread in HAE.

Our results are also consistent with the emerging role of MUC1 in response to inflammatory stimuli and we expand on known inflammatory triggers for its expression both in HAE and in PMD macrophages. Indeed, the surprising finding that MUC1 is upregulated beyond the apical layer supports a broader dynamic role during infection at the epithelial surface. Specifically, our data support the model proposed by Kato *et al.* [335] whereby pathogenic insult leads to general inflammation that subsequently upregulates MUC1 expression and immune cell recruitment [347]. This would immediately protect local epithelial cells by acting as a barrier, but further accumulation would help

resolve potentially harmful inflammation and simultaneously prime cells for survival and ultimately proliferation to repair local tissue damage following infection.

Additionally, our results demonstrate that MUC1 significantly reduces IAV replication by acting early in infection, consistent with its canonical role as a barrier protecting the airway epithelium. However, instead of the model that suggests MUC1 is acting as a soluble decoy receptor that is dynamically shed in response to viral interaction, our work indicates that MUC1 acts as a general barrier to productive endocytic uptake. As we only investigate the earliest steps in IAV infection of HAE, future studies should aim to investigate how viral-mediated upregulation of MUC1 might impact subsequent spread and immune response to an established infection.

Chapter 5 : Interferon Responses in HAE and Impact on Viral Infection Dynamics

Jorg Calis^{1,2,*}, Kira Griswold^{3,4,*}, Ethan Iverson^{4,*}, Emma DeGrace^{1,*}, Skyler Uhl¹, Peter Falci⁴, Brad Rosenberg^{1,#}, Margaret A. Scull^{4,#}

¹ Department of Microbiology, Icahn School of Medicine at Mount Sinai, New York, NY, USA

² Laboratory of Virology and Infectious Disease, The Rockefeller University, New York, NY, USA

³ Department of Pediatrics, University of Pittsburgh, Pittsburgh, PA, USA (Current address)

⁴ Department of Cell Biology & Molecular Genetics and Maryland Pathogen Research Institute, University of Maryland, College Park, MD, USA

⁵ Fischell Department of Bioengineering, University of Maryland, College Park, MD, USA

* Equal contribution

Corresponding author

Email address: brad.rosenberg@mssm.edu; scull@umd.edu

My contribution to this work includes helping with the generation, stimulation, and dissociation of HAE cultures for single-cell RNA sequencing. I contributed expertise on airway epithelial cell biology, specifically cell type-specific gene expression, during initial cluster analysis. I also validated infection phenotypes and ISG expression profiles (including CXCL10 and CD38) at the protein level through *en face* immunostaining and flow cytometry and drafted the manuscript.

5.1.1 Abstract

The extensive environmental contact between the respiratory tract combined with its unique functional constraints gives rise to the unique tissue of the human airway epithelium (HAE). In part owing to the presence of multiple unique cell types, different regions and component cell types exhibit differential susceptibility to viral infections. As the principle component of the anti-viral response, interferon (IFN) has been studied extensively for its protective functions including therapeutic use against an array of viral pathogens. While previous work has hinted at an asymmetrical capability to respond to

IFN apically and basolaterally in HAE, this is at odds with previous reporting about secretion of IFN in both compartments. Here we utilize a highly polarized primary HAE system grown at an air-liquid interface to explore the response to both apical and basolateral site-exposure of type I and type III IFN. Additionally, we utilize single-cell RNA sequencing methods to explore both the identity of the cells present within our HAE system, finding congruence with *in vivo* reports. We also assess their individual responses to multiple IFN types and exposure sites. We find that while there is robust expression of type I and type III IFN receptors basolaterally as previously described, apical expression in some ciliated cells can also be observed. Moreover, the response to apical or basolateral site-exposure is protective against both influenza A virus and severe acute respiratory syndrome coronavirus 2 challenge. Importantly, type I IFN basolateral site-exposure induces a stronger interferon stimulated gene (ISG) response profile relative to its apical exposure, while this is not observed for type III IFN. We find shared ISG response profiles as well as cell type-specific response profiles, and that these cell type-specific response profiles are also reflective of protein expression following IFN or viral infection. Overall, our data advances our understanding of HAE response to IFN as a function of site-exposure and cell type and serves as a foundation for further investigation on the complexities of IFN response dynamics.

5.1.2 Introduction

A large array of viral respiratory pathogens, including members of the *Picornaviridae*, *Coronaviridae*, and *Orthomyxoviridae* families, target the human airway epithelium (HAE) for infection [133]. Ultimately, these acute viral respiratory infections represent a significant cause of morbidity and mortality [117,350,351]. A principle mechanism to alleviate infection-mediated disease is preexposure prophylaxis with

vaccinations [352]; however, many challenges remain in effectively targeting future emerging and even current viral respiratory pathogens [352,353]. Post-exposure prophylaxis through direct-acting antivirals offers the ability to attenuate severe disease and prevent deaths without prior host immunity [354]. However, development of effective and safe direct acting antivirals is a laborious and time-consuming process and their absence in the wake of emergent virus pandemics, such as in the case of severe acute respiratory syndrome coronavirus 2 (SARS-CoV-2) [355], poses a grave threat to global public health. Additionally, the majority of extant direct-acting antivirals target chronic infections, namely human immunodeficiency virus and hepatitis C virus [354]. In the absence of universal direct acting antivirals or existing vaccines, interferon (IFN) based therapeutics represent a potentially broad antiviral class that could be efficacious [354,356].

As a key component of the antiviral response, IFN represents a potent restricting factor to viral infection as well as a source for immunopathology [357–359]. Interaction between extracellular IFN and its cognate receptor potentiates signaling through the classical JAK/STAT pathway, coordinating the expression of hundreds of interferon stimulated genes (ISGs) [357,359]. Importantly, despite the numerous distinct IFN subtypes, there are only three unique receptors (one dedicated for each IFN type), implying the existence of complex and nuanced signaling inputs [357]. Indeed, type I (e.g. IFN α , IFN β) and type III (e.g. IFN λ_1) both mediate antiviral signaling in HAE with somewhat redundant roles [65,67,360].

It has been shown that HAE secrete IFN both apically (i.e. towards the airway lumen) and basolaterally (i.e. toward the extracellular matrix and vasculature) in the context of viral infection [361]. Similarly, multiple delivery routes for IFN are under development [356,362]. Since previous work has suggested the basolateral

predominance of type 1 IFN receptor components [363], study on the response profile to IFN in the highly polarized context of the HAE [1] is important for the rational design of IFN-based antiviral therapeutics. Furthermore, the HAE is composed of multiple cell types which vary in form, function, location, abundance, and degree of interaction with the airway luminal environment [1]. Additional work to date has highlighted cell-specific responses and their broader connection to pathology following respiratory virus infection [364,365]. However, cell type-specific receptor expression and moreover cell-specific response profiles to IFN is lacking.

Thus, to explore the impact of IFN on HAE as a function of the site of exposure and component cell identity, we utilized a primary HAE model which recapitulates important physiological aspects of the human airway, such as diverse cell types and high degree of polarity [1,366]. Due to the fact that primary HAE cultures are also susceptible to a diverse array of respiratory pathogens [1] and faithfully recapitulate the HAE response to infection, they have become the gold-standard for modeling respiratory virus-host interactions *in vitro* [75,76,366]. Here we extend previous reports describing differential expression of IFN receptor components within HAE. In alignment with this heterogeneous receptor expression, we find the type and location of IFN application impacts the overall magnitude of the IFN response and further identify both global and cell-type specific ISG expression in HAE, particularly for IFN β . Selected cell-type specific ISGs were further analyzed and their restricted expression found to be maintained in the context of IAV and SARS-CoV-2 infection. Overall, these results expand our knowledge of respiratory HAE responses to IFN and viral infection, paving the way for the rational therapeutic use of IFN.

5.1.3 Polarization of IFN Secretion and IFN Receptor Distribution in HAE

We and others have shown that IAV infection of primary HAE cultures grown ALI leads to secretion of IFN in to both apical and basolateral culture compartments following viral infection [361,363]. To further explore HAE immune response kinetics in response to IAV infection, we infected HAE with 500 PFU of the H1N1 influenza virus A/PR/8/34 (PR8) and monitored the kinetics of viral infection and IFN generated in 24-hour intervals. Productive infection was confirmed by the increase in viral titer over time, achieving titers in excess of 1×10^7 PFU / mL by 48 hpi (**Fig 5.1A**). The detection of viral nucleoprotein (NP) antigen by immunostaining also revealed the dissemination of the virus over time, with most of the culture surface being infected by 48 hpi (**Fig 5.1B**). In response to ongoing viral PR8 replication, we found that HAE secreted both type I and type III IFN throughout the course of infection. However, the magnitude and timing of the secretion of each IFN differed. IFN λ_1 and IFN λ_3 secretion was detected as early as 24 hpi in both culture compartments (**Fig. 5.1D**) while IFN β – also secreted bidirectionally – was only detected at 48 hpi (**Fig 5.1C**).

In the absence of IFN receptor expression on the apical surface of the HAE cultures, the bidirectional secretion of IFN could be interpreted as resulting from errant secretion or lysis of IFN-producing cells. Indeed, previous reporting has suggested that IFNAR2 is expressed basolaterally and that this asymmetric localization controls TLR3 expression in responses to basolateral type I IFN [363]. Thus, to further assess IFN receptor localization and potential cell-type specific expression, we probed histological cross-sections of HAE with antibodies specific for each receptor component (**S. Fig. 5.1**). In alignment with previous studies [363], we observed robust expression of IFNAR2 on the basolateral surface of the culture, which was also observed for other type I (i.e. IFNAR1, albeit to a lesser extent) and type III (i.e. IL28R and IL10Rb) receptor

components. However, we also detected expression of all receptors at the apical surface, though this was limited to a subset of ciliated cells (**Fig. 5.1E**).

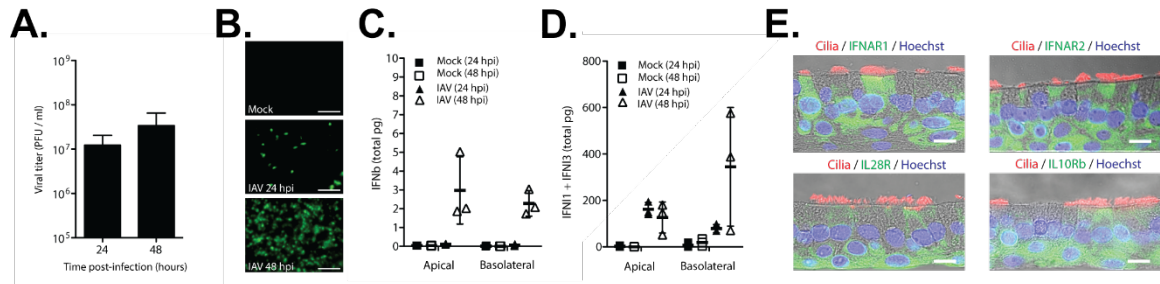


Figure 5.1. HAE are Permissive to IAV and Exhibit Asymmetrical IFN Receptor Expression and IFN Secretion. HAE were infected with 500 PFU PR8 and (A) washes were collected to determine viral titer prior to (B) fixation and staining for viral antigen (NP, green). In (C) and (D) the apical and basolateral secretion of IFN β and IFN λ 1 or IFN λ 3 was determined from apical washes and conditioned media from the basolateral compartment. Data representative of three biological replicates from one HAE donor. Error bars indicate the standard deviation. In (E), IHC staining of HAE for the distribution of the type I IFN (IFNAR1 and IFNAR2) and type III IFN (IL28R and IL10Rb) receptor components were compared to isotype controls (**S. Fig. 5.1**). In (E), scale bar = 10 μ m.

5.1.4 Apical and Basolateral Application of Type I and Type III IFN is Protective Against IAV and SARS2

Given our detection of both the apical and basolateral expression of type I and type III IFN receptors, we next sought to investigate whether site-specific application of these IFNs can lead to the productive establishment of an antiviral state. To do this, we applied IFN β (1 nM) to either the apical or basolateral compartment alone, or to both compartments of the culture simultaneously for 6 or 24 hours. Following this compartmentalized stimulation, transcripts of the antiviral gene MX1 were found to be elevated at all time points (**S. Fig. 5.2**), with the most robust MX1 expression found in conditions with basolateral treatment, indicating successful IFN-mediated signaling. To assess whether these differential responses could be restrictive to viral replication, we applied IFN β as before, alongside

IFN λ_3 (10 nM), a representative type III IFN. After stimulation for the indicated time, HAE were inoculated with PR8 and viral titer was quantified 24 hpi (**Fig. 5.2A**). Compared to either single directional treatment, stimulation with both apical and basolateral IFN β had a more potent protective effect. Following 24-hour stimulation the protective effect of all directional treatments was more potent. Indeed, following the combined apical and basolateral IFN β application, no viral titer could be recovered. These trends were also similar for IFN λ_3 application, with all treatments and time points eliciting significant protection from IAV. However, 6-hour treatment apically was less protective relative to basolateral treatment or combined treatment. Following 24-hour stimulation, this relative difference between apical IFN λ_3 and basolateral or combined stimulation was less pronounced. Overall, these results confirm the protective effect of both type I and type III IFN and suggest exposure time and directional nuances to the elicited antiviral state.

To ensure that the directional effects of IFN are not confounded by potential leakage or mobility between compartments, we utilized a 20kDa FITC-dextran probe which is slightly smaller than the molecular weight of IFN β , predicted to be 22 kDa. We applied this FITC-dextran apically or basolaterally to normal HAE cultures. HAE cultures treated with EDTA (to disrupt cell-cell junctions and contacts) and Transwells without any cells were used as controls. After 24 hours, the relative fluorescence of each compartment was assessed. Following apical application to a Transwell lacking any cells, roughly two thirds of the FITC-dextran was present in the basolateral chamber relative to the apical chamber (**Fig. 5.2B**), indicating significant mobility between compartments. By contrast, when applied apically to a normal HAE culture, FITC-dextran mobility was entirely restricted to the apical compartment (**Fig. 5.2B**). Treatment with EDTA, however, was able to completely overcome the mobility restriction posed by the in-tact HAE culture, following the same distribution pattern seen without cells on the Transwell, and suggests that cell-

cell contacts play an important role in maintaining separation between compartments. Similar results were obtained following the basolateral application of FITC-dextran although basolateral-to-apical migration following EDTA treatment was more restricted relative to the Transwell only condition (**Fig. 5.2C**). Together these results confirm that the results reported in (**Fig. 5.2B**) are due to site-specific effects of IFN rather than culture permeability or transport of IFN across HAE.

Next, we sought to expand the results from (**Fig. 5.2A**) and assess whether the directionality of IFN treatment was able to restrict the replication of SARS-CoV-2. In this experiment HAE cultures were treated with 1 nM IFN β either apically, basolaterally, or in both compartments, as before. However, the IFN treatment was further subdivided to be 24-hours prior to or 24-hours after SAR-CoV-2 inoculation of 1×10^6 PFU (approximate MOI of 20), where the post-infection treatment better mimics real-world clinical scenarios of post-exposure therapeutics. In all conditions, the infection was allowed to progress for 48 or 72 hours, at which point cultures were fixed and subjected to immunostaining for viral antigen (**Fig. 5.2D**, nucleocapsid, N). We then quantified the percent of the epithelial surface staining positive for viral antigen in pre-determined fields of view (**Fig. 5.2E**). In all IFN β pre-treatment conditions, there was a reduction in viral antigen-positive area across all the HAE cultures regardless of the directionality of IFN exposure (**Fig. 5.2E**). However, application of IFN β to the apical compartment alone exhibited the least restriction to viral replication while basolateral and combined stimulation conditions were able to potently restrict spread across the HAE (**Fig. 5.2E**). Similarly, treatment of HAE with IFN 24 hours post-infection was effective in restricting viral replication relative to the vehicle control, where, once again, apical IFN application had the least impact relative to vehicle conditions and basolateral and combined stimulation conditions exhibited potent restriction on viral spread.

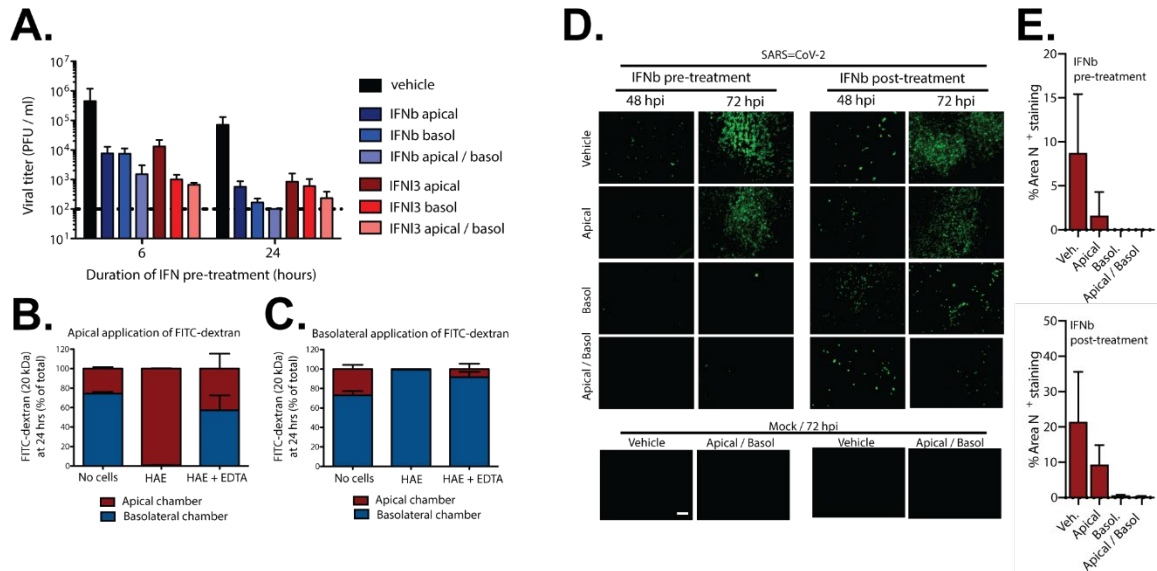


Figure 5.2. IFN Stimulation of HAE from Apical and Basolateral Sources is Protective Against IAV and SARS-CoV-2. In (A), HAE were stimulated with IFN β (IFN β) or IFN λ_3 (IFN λ_3) by the indicated routes for either 6 or 24 hours. Afterwards, cells were infected with 500 PFU of PR8 for 24 hpi and apical washes used to determine viral titer by plaque assay. Data representative of nine biological replicates across two HAE donors. FITC-dextran was applied to either the (B) apical or (C) basolateral chamber to empty Transwells (no cells), HAE, or HAE with 0.5 M EDTA (HAE+EDTA) for 24 hours. Afterwards, fluorescence in each compartment was analyzed as a percent of total applied. (D) HAE were stimulated with IFN β 24 hours prior to (left) or after (right) inoculation with 1×10^6 PFU SAR-CoV-2. At the indicated time points, cultures were fixed and stained for viral antigen (N, green) and (E) the total area of fluorescence in predetermined fields of view analyzed using FIJI. Data representative of six biological replicates from two HAE donors. Error bars are indicative of the standard deviation.

5.1.5 HAE Is Composed of Diverse Cell Types Consistent with Airway Epithelium

In Vivo

As HAE cultures grown at an air liquid interface are capable of differentiating into multiple cell types present *in vivo* and recapitulate transcriptional profiles of the native tissue (reviewed in [1]), we sought to further explore the HAE cellular composition as well as potential cell-type specific responses to type I and type III IFN applied either apically or

basolaterally. To do so, cultures were dissociated by short, repeated incubations with the cell-dissociative reagent TrypLE. Released cells were removed to a protease-neutralizing solution after each incubation to preserve viability and the final cell suspension was passed through a 10-micron strainer to eliminate multicellular clumps. These samples were then integrated into a microfluidic device to facilitate partitioning of single cells into oil-emulsion droplets that also contained lysis and reverse transcriptase reaction components along with barcoded primer-carrying microspheres. This technique, termed “inDrop” [270], enables subsequent pooling and amplification of all cell material prior to single cell RNAseq and barcode-mediated deconvolution of individual cell transcriptomic profiles.

After sequencing and quality control, data from mock- or IFN-treated HAE cultures were mapped and quantified in a modified, custom pipeline based on previous pipelines [269,270]. Clustering analysis revealed major cell type components of HAE [8,10], namely ciliated, goblet, club, and basal cells (**Fig. 5.3A and 5.3B**). Notably, the relative proportion of each cell type was stable across the various IFN treatments (**Fig. 5.3C**). We also found subsets of cells within some of these clusters and the profiles of intermediate groups presumably caught within the active process of differentiation (**Fig. 5.3A**). As recently reported [8,10], we were also able to detect a rare population of cells referred to as ionocytes. These results are congruent with the cells described in the human lung cell atlas [10], confirming the strong utility of the HAE model as an *in vitro* correlate of *in vivo* epithelial biology.

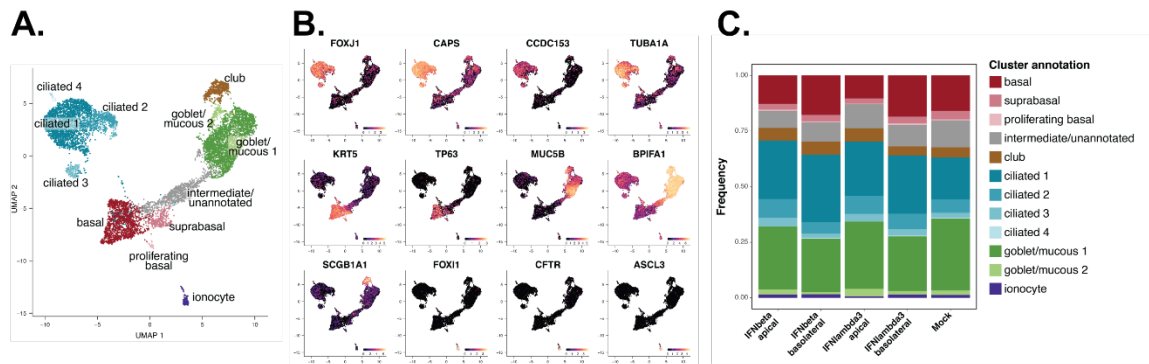


Figure 5.3. The Cellular Composition Profile of HAE. HAE cultures were dissociated and subjected to single-cell RNA sequencing using the inDrop method. Using a custom analysis pipeline (see section 2.3.14 and 2.3.15), annotated UMAP plots were generated and display (A) inferred cell identity after integration across treatment conditions or (B) cell-identity defining gene expression patterns (higher expression indicated by lighter tones). In (C) the frequency of cell identities after integration shown in (A) are displayed, showing minimal impact on cell identity inference by the integration analysis.

5.1.6 Differences in the Magnitude of the ISG Response in Apical vs. Basolateral Stimulation are More Pronounced for IFN β than IFN λ

Next, we looked at ISG induction following apical or basolateral application of IFN β or IFN λ within each of the four main component cell types. For many ISGs, we observed a statistically significant difference in induction between the two sites of IFN β exposure (indicated with a connecting line) (**Fig. 5.4**). Consistent with our results in **Fig. 5.2** showing a robust antiviral effect following basolateral IFN stimulation, basolateral application of IFN β frequently induced significantly higher transcript levels of specific ISGs relative to apical stimulation (**Fig. 5.4**). This effect was seen across all four main cell types, though the relative differences in apical vs. basolateral-mediated ISG expression varied across

cell types and individual ISGs (**Fig. 5.4**). By contrast, following IFN λ_3 application, relatively few ISGs were differentially expressed between apical and basolateral application conditions (**Fig. 5.4**); further, this lack of differential induction was consistent across the four main cell types. Together these results suggest that the impact of IFN stimulation directionality on ISG induction varies as a function of the type of IFN. Generally, IFN β elicited a response of greater magnitude with basolateral stimulation than apical stimulation, while IFN λ_3 stimulation did not vary significantly by the directionality of stimulation.

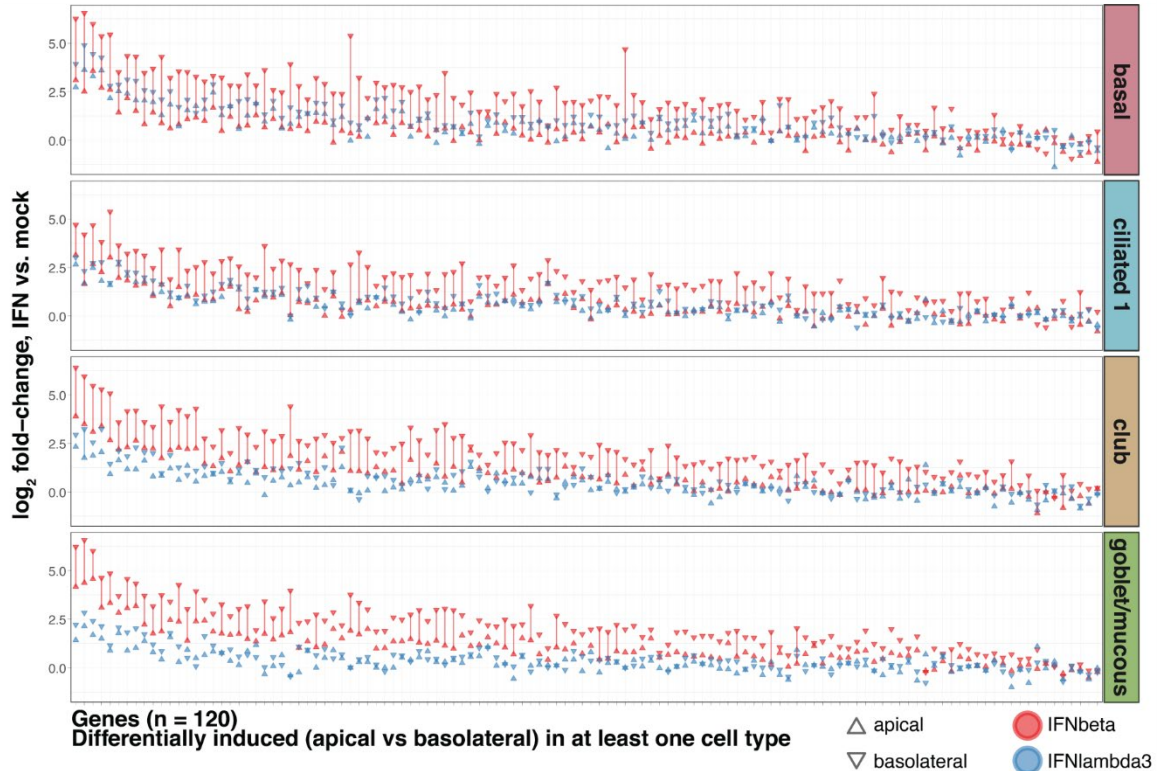


Figure 5.4. The Basolateral Application of Type I IFN Induces Stronger ISG Expression in Four HAE Cell Types. Induction of ISG from the single-cell RNA sequencing dataset for four main cell types (basal, ciliated 1, club, and goblet/mucous). Each position along the x-axis denotes a different ISG. The log₂ fold-change differences (relative to mock for each condition) in induction based on the compartmental delivery of the same IFN for the same ISG among each cell type grouping are indicated on the y-axis. Where significant (cutoff of 0.58 log fold-change with a minimum p value of 0.0001), vertical lines connect the points within the same IFN type.

5.1.7 The HAE IFN Response Induces a Shared ISG Program and Cell Type-specific ISGs

Given that basolateral stimulation with IFNβ yielded the most robust ISG response, we focused on this condition to further analyze the response as a function of cell type to see conserved and differential ISG induction programs. In this analysis we computed the differential gene expression of each ISG by cell type relative to mock conditions. **Figure 5.5** shows all genes across the X-axis which were differentially expressed relative to mock

conditions. The Y-axis shows the significance of the upregulation based on the analysis pipeline adapted for single-cell RNAseq [276,277] rather than a simple analysis on the fold-change of gene expression in the relatively sparse datasets of individual cells. Each of the genes plotted here has a point for each cell type. Our results reveal genes following a “classical” ISG expression pattern (**Fig. 5.5**) where, absent IFN stimulation, there is almost no detectable expression; however, following IFN stimulation there is a robust upregulation among all cell types. Additionally, our analysis reveals cell-specific induction profiles (**Fig. 5.5**). For instance, chemokines CXCL10 and CXCL11 are highly induced in basal cells following IFN β stimulation with either low or nearly no induction in other cell types, respectively. By contrast, the multifunctional CD38 was induced only in ciliated cells. Together our results reveal shared programs of ISG response following IFN stimulation across all cell types as well as cell-type specific response programs.

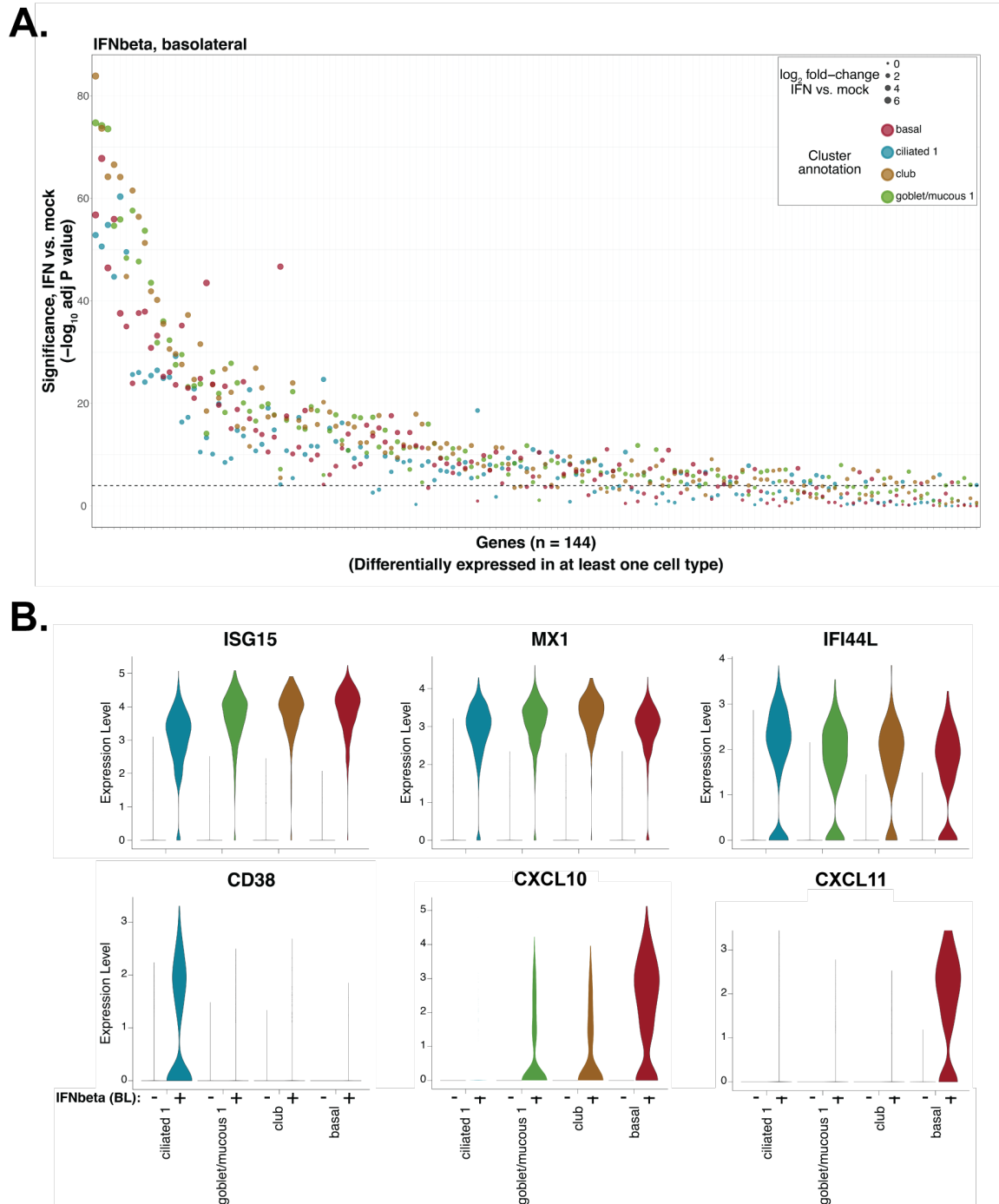


Figure 5.5. The Significance of ISG Upregulation Following Basolateral Type I IFN Exposure and Cell-Type Specific ISG Expression. (A) Each x-axis position denotes a different ISG where induction relative to mock conditions is statistically significant. The cell type is denoted by the colored circle as indicated. (B) The expression level (y-axis) of the indicated genes for each cell, grouped by cell type, displayed on a violin plot. The expression profile with (+) and without (-) IFN β is shown within each cell type. The top row shows a “classical” ISG signature whereas the bottom row shows cell-type specific induction by IFN.

5.1.8 Cell Type-specificity of CD38 and CXCL10 is Retained on the Protein Level in the Context of Both Apical and Basolateral IFN Stimulation and During Infection

Since our transcriptional analysis of human airway epithelial component cell type responses to IFN revealed both shared and cell type specific ISG induction profiles, we next sought to validate these findings at the protein level. To do this, we first stimulated HAE apically and basolaterally with IFN β in the presence of secretory pathway inhibitors to promote the intracellular accumulation of the secreted chemokine CXCL10. Next, cultures were dissociated, fixed, and stained for CXCL10 (or MX1) prior to flow cytometry analysis. As shown in **Fig. 5.6**, and in alignment with our single cell-sequencing results, following a 6-hour IFN β stimulation, protein expression of MX1 was detected in cells without the basal cell marker, KRT5, as well as those with KRT5. Staining for CXCL10, however, was largely restricted to KRT5-positive cells (**Fig. 5.6A, C, right**). To investigate whether the protein expression profile of CD38 was also congruent with our transcriptional data enrichment, we stimulated HAE with IFN β apically and basolaterally for 24 and 48 hours. Following dissociation and immunostaining as before, comparison of CD38 staining as well as a ciliated cell marker (acetylated α -tubulin) revealed a high degree of double-positive cells (**Fig. 5.6B, C, left**). Together these data reveal congruence between the computed significance applied to our single-cell transcriptional dataset and protein expression by HAE.

To determine if we could find evidence of these cell specific ISG programs after viral infection, we infected HAE with 500 PFU of PR8 (approximate MOI of 0.01). At 48 hpi cultures were fixed and processed for histology and subsequent immunostaining. As shown in **Fig 5.6D**, by 48 hpi CD38 is upregulated in ciliated cells in IAV-infected cultures as compared to mock cultures. We also sought to investigate if cell type-specific

upregulation of CD38 held for SARS-CoV-2. As before, we infected HAE cultures with 1×10^6 PFU SARS-CoV-2 (approximate MOI of 20) and fixed cells 48 hpi for analysis of both SARS-CoV-2 antigen and CD38 expression by *en face* immunofluorescence. For comparison, HAE cultures were either mock-stimulated, or stimulated with apical and basolateral IFN β in parallel. Mock cultures showed very little to no apparent CD38 staining, but the CD38 that was detected was restricted to cells that also stained positive for alpha acetylated tubulin (cilia marker). Cultures stimulated with IFN β showed elevated expression of CD38, again localized to ciliated cells (**Fig. 5.6E**). Notably, a minority of ciliated cells expressed much higher levels of CD38 (**Fig. 5.6E**). Similar to the IFN β condition, SARS-CoV-2-infected HAE demonstrated ciliated cell-specific upregulation of CD38. However, the overall degree and extent of CD38-positive ciliated cells was more limited and generally restricted to regions of obvious cytopathology. Together these data demonstrate that the transcriptional induction of CD38 in response to IFN β as shown by our single-cell RNA sequencing dataset is supported by multiple protein-based detection methods and additionally occurs within the context of viral infection.

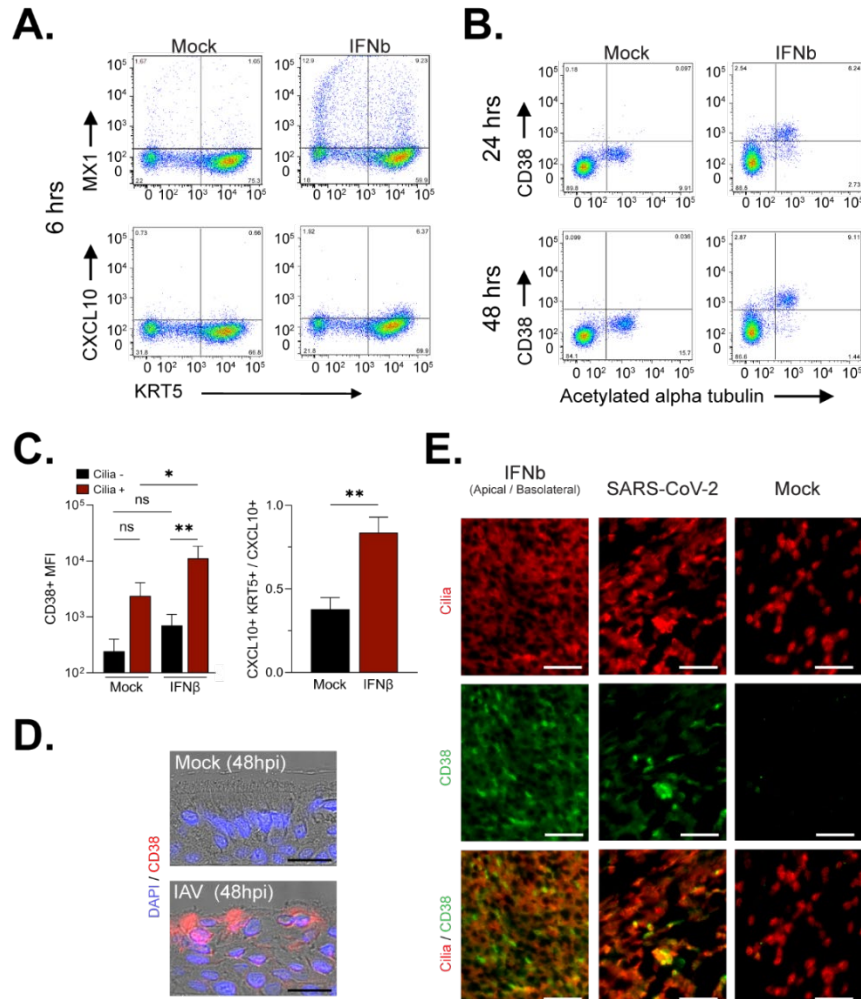


Figure 5.6. CXCL10 and CD38 Protein Expression Matches Transcriptomic Data and SARS-CoV-2 Induces CD38 Expression in Ciliated Cells. HAE cultures were stimulated apically and basolaterally with IFN β for (A) 6 hours in the presence of protein secretory inhibitors or (B) 24 and 48 hours before being dissociated for flow cytometry analysis. In (A), the “classical” ISG of MX1 is compared alongside the basal cell marker, KRT5, revealing ubiquitous expression after IFN stimulation. By contrast, CXCL10 expression is restricted to a subset of KRT5-positive cells. In (B), CD38 is compared against the ciliated cell marker (acetylated alpha tubulin), revealing a ciliated-cell restricted expression pattern after IFN stimulation. In (C), the mean-fluorescence intensity (MFI) of CD38 (left) staining for ciliated and non-ciliated cells is compared between mock and IFN β stimulated conditions, revealing significant induction of CD38. On the right, the fraction of CXCL10- and KRT5-positive cells over the total number of CXCL10-positive cells is graphed, showing significant expression restriction by cell marker. Data representative of three biological replicates from three HAE donors and considered statistically significant by Mann-Whitney U test (* $p < 0.05$; ** $p < 0.01$). In (D), mock- and A/PR/8/34-infected HAE were processed for IHC and stained for CD38 (red) or nuclei (blue). By 48 hpi, induction of CD38 in ciliated cells is evident. In (E), HAE stimulated with IFN β (48 hours), infected with 1×10^6 PFU of SARS-CoV-2, or mock treated (72 hpi) were fixed and immunostained for cilia (red) or CD38 (green). IFN treatment or SARS-CoV-2 infection is associated with CD38 expression restricted to ciliated cells.

5.1.9 Discussion

In this chapter we have explored the IFN-driven response programs by HAE both after IFN stimulation and in the context of infection by several respiratory viruses. Our initial results confirm the asymmetric secretion of IFN following IAV infection and reveal differential kinetics to type 1 and type 3 IFN expression. Additionally, we have revealed that both type 1 IFN receptor components are ubiquitously expressed along the basolateral surface of the pseudostratified epithelium, in alignment with previous data showing basolateral polarization of IFNAR2 during differentiation [363]. We also detected IFNAR1 and IFNAR2 in some columnar epithelial cells, notably ciliated cells, at the apical surface. This same expression pattern holds true for type III IFN receptor components (i.e. IL28R and IL10Rb) which are known to be restricted to mucosal epithelium [66,343] but which to knowledge on the specific localization for HAE was lacking. This heterogeneity in IFN receptor component distribution suggested that the magnitude of the antiviral response may differ according to IFN exposure site and that component cell types may exhibit unique ISG signatures.

In line with these receptor expression profiles, we find that HAE can elicit an antiviral response following either type I or III exposure, at either the apical or basolateral surface. Moreover, the responses generated by IFN from each direction are restrictive of viral replication in HAE, albeit varying by the IFN type and site of exposure. Generally, any IFN stimulation is potently restrictive when given prior to IAV or SARS-CoV-2 inoculation though earlier and longer stimulation periods exhibit enhanced protection. Furthermore, in at least the case of SARS-CoV-2, these protective effects are still very restrictive to viral spread when applied even 24 hrs after viral inoculation. Importantly, this delayed application of IFN β following SARS-CoV-2 infection best parallels the clinical setting. Moreover, while basolateral and combined application routes demonstrated the most

potent effects, apical application was still protective. This suggests that the targeted and direct IFN delivery to the airway lumen, such as by nebulized IFN, is also able to achieve a protective antiviral state in HAE and therefore could be valuable in a clinical setting in the treatment of SARS-CoV-2 and potentially other respiratory viral infections.

However, we see a difference in the relative response to type I IFN when applied apically or basolaterally relative to type III IFN. Specifically, type I IFN induces a stronger response when delivered basolaterally compared with apically, whereas type III IFN induces ISGs to the same degree regardless of directionality. As the principle responding cell type to each of these stimuli will differ based on the location of application, this hints at the possibility whereby a coordinated antiviral state can be shaped by this initial “sentinel” exposure. Indeed, we do not find universal differences in, for example, ciliated cell expression of ISGs following directionally distinct IFN exposure. For instance, following apical exposure to IFN β , ciliated cells would have a direct stimulation not reliant on paracrine signaling from any other cell within the HAE culture. However, following basolateral exposure, as IFN is not able to transit through the HAE culture, ciliated cells would presumably be reliant on the paracrine signaling of basolateral cells propagating this stimulus to the apical-facing epithelium. Despite the fact that ciliated cells would be responding indirectly to this basolateral signal, they, along with the other major cell-type components of our HAE system, induce their ISG program the strongest. However, this trend does not hold for stimulation by IFN λ_3 , implying the difference in response programs not only by IFN type, primary stimulated cell (by compartment), but additionally by cell type. In line with this inference, we find the differential expression of various ISGs by cell type. In the case of chemokines, such as CXCL10 and CXCL11, it might be that relatively little (but tightly regulated) expression is preferable to reduce the chance of immunopathology and excessive immune cell recruitment. In the case of CD38, there is

no known role for its expression in HAE to our knowledge. Still, universal and conserved “generalist” ISG response programs are clearly evident and warrant further investigation.

Together these results have implications not only for understanding the course of the immune response in the context of respiratory infection [359] but also in rational design of clinical trials of IFN as therapeutics [354]. Indeed, clinical trials on the use of IFN as a therapeutic for SARS and MERS are inconclusive on the extent to which there is a benefit of use [359]. However, as the route of exposure, type of IFN, and timing relative to the initial infection or overall therapeutic course can vary significantly [358], understanding how each of these factors impacts and shapes the immune response positively or negatively is critical. Ultimately, the utility of IFN in response to a viral infection might also be pathogen specific, as SARS-CoV-2 shows type 1 IFN susceptibility where SARS-CoV does not [367]. Moreover, the receptor for SARS-CoV-2—ACE2—can be stimulated by IFN α 2 and IFN γ [368]. As such, systemic administration of type 1 IFN, for instance, might be ill advised. Nevertheless, phase 2 trials of nebulized IFN β for the treatment of SARS-CoV-2 infection are underway. Together our results expand our understanding of IFN and HAE cell-type specific responses and pave the way for future functional studies on specific IFN-induced antiviral programs as well as rational design of IFN-based therapeutic trials.

Chapter 6 : Conclusion

In this dissertation, we investigated human airway epithelial defensive capabilities against influenza virus. Chapter 3 investigates the diffusion of influenza virus as it transits through secreted mucus. Chapter 4 describes how the tethered mucin 1 (MUC1) is regulated within human airway epithelium (HAE) after exposure to interferon (IFN) or influenza virus (IAV) infection while also detailing the pro-viral impact the loss of MUC1

has on IAV entry and spread. Finally, Chapter 5 details how HAE responds to different types of IFN based on the directionality of the exposure as well as the various cell-type specific responses and their impact on viral replication.

In viewing the viral transmission cycle, we considered the first barrier to successful respiratory viral infection to be the secreted mucus barrier. As previous literature has shown that the secreted mucus gel is protective against IAV [200,280], we sought to characterize the impact of secreted mucus microstructure and adhesive properties on IAV diffusivity. Overall, we found that the mucus microstructure, namely the degree of cross-linking and therefore local pore size, play a large role in the diffusivity of IAV. Indeed, by disrupting the native disulfide bonds of patient mucus samples and therefore increasing the sample pore sizes, we were able to show that IAV diffusivity increases as well. By using purified bovine submaxillary mucus [255] we were able to increasingly titrate a cross-linking agent to achieve the same effect.

Surprisingly, we found that inactivation of IAV neuraminidase (NA) did not consistently reduce viral diffusivity. Indeed, in some patient samples IAV was more diffusive, even without changes in pore size for those samples. Ultimately, however, the possibility of microstructural changes resulting from the NA inhibitor itself confound the straightforward interpretations on the adhesive properties of patient-derived mucus and warrants further study. While previous reporting links the sialic content of secreted mucus as a mechanism for its IAV neutralizing capabilities [160,280], it is possible that NA primarily liberates virions that would be otherwise trapped by local microstructure or sialic acid presentation rather than the diffusion prior to such entrapment. Other groups have suggested that the morphology of virions impacts the penetration of secreted mucus gels by impacting the location of viral glycoproteins [205]. However, beyond potential glycoprotein polarity effects, we believe that rod-like morphology alone could enhance

individual virion mobility in secreted mucus gels [369,370]. Future work with the SMA will be able to investigate not only the impact mucus composition plays on IAV but further address the impact of viral morphology on diffusivity.

After successful penetration of the secreted mucus layer, incoming viruses encounter tethered mucins within the periciliary layer (PCL). We reasoned that the ubiquity of their luminal expression [15] and potential to be sialylated [17] might mean that IAV directly interacts with a tethered mucin. Previous work identified an interaction between IAV and the most abundant tethered mucin, MUC1, in the context of immortalized adherent cells [321]. In line with this previous finding, we were able to show through several assays the feasibility of an HA-mediated interaction with MUC1, including the co-localization of IAV and MUC1 by electron microscopy. However, we did not find that IAV mediates any “shedding” of the extracellular component of MUC1. Using a genetically tractable immortalized HAE line, we sought to investigate how the CRISPR/Cas9 mediated genetic depletion of MUC1 impacts the kinetics of IAV infection. Compared to non-targeting control cultures, cultures depleted for MUC1 had markedly increased IAV replication. By varying the inoculation time of IAV on control and MUC1-depleted cultures and by applying a high amount of NA inhibitor after these brief adsorption periods, we were able to assess the impact of MUC1 on successful viral entry timing. Preliminary results suggest that in the absence of MUC1, IAV is able to successfully initiate entry more rapidly than control cultures. In the future we can assess the impact of MUC1 on other respiratory viruses as well as investigate the role of other tethered mucins (e.g. MUC4 and MUC16) on viral entry and replication. While MUC1 is the most abundant tethered mucin in the airway, MUC4 and MUC16 are also very common and could differentially modulate infection dynamics.

Unexpectedly, we found that MUC1 expression is driven by type I and type III interferon (IFN) despite not being a canonical interferon-stimulated gene (ISG). Indeed, infection of HAE with IAV was also able to induce MUC1 expression. Intriguingly, we did not detect transcriptional upregulation, hinting at the possibility of post-transcriptional regulatory mechanisms governing MUC1 expression. As previous work had shown that macrophages expressed MUC1 in response to type II IFN and bacterial PAMPs, we sought to investigate if this held true for the type I and type III IFN expressed by IAV-infected HAE. Notably, in addition to double-stranded RNA (i.e. a viral PAMP), type I and III IFNs were able to induce MUC1 expression in primary monocyte-derived (PMD) macrophage cells. Moreover, transfer of conditioned basolateral media from IAV-infected HAE was also sufficient to drive MUC1 expression in PMD macrophages. Together we showed that MUC1 is widely expressed across HAE in response to IAV infection and that the IFN-driven expression of MUC1 is also true of PMD macrophages. As previous work has identified an anti-inflammatory role for MUC1 [335], we predict that the inflammatory- and IFN-driven expression of MUC1 serves to reduce local immunopathology. Future work is needed to better delineate the consequence of this upregulation in the context of viral infection of HAE, as well as the extent to which non-epithelial cells also express MUC1 in inflammatory or anti-viral contexts.

We also sought to expand previous work [363] and further explore the IFN-responsive nature of HAE. We found that not only are HAE expressing type I and type III receptor components apically in addition to basolaterally, but that the response to IFN by exposure from either compartment is capable of establishing a protective antiviral state. Indeed, IFN exposure prior to IAV and SARS-CoV-2 infection was potentially restrictive to viral replication and moreover exposure to IFN even 24 hpi significantly inhibited infection by SARS-CoV-2. Intriguingly, we found that only a subset of ciliated cells expressed type

I or type III IFN receptors, implying the possibility of cell-type specific IFN responses in addition to IFN responses varying by directionality of exposure. As previous reporting suggested that HAE was only capable of responding to type I IFN from the basolateral compartment [363], our confirmation that HAE can productively respond to IFN present in the airway lumen has implications for delivery of IFN as a broad-spectrum antiviral therapeutic [359,362].

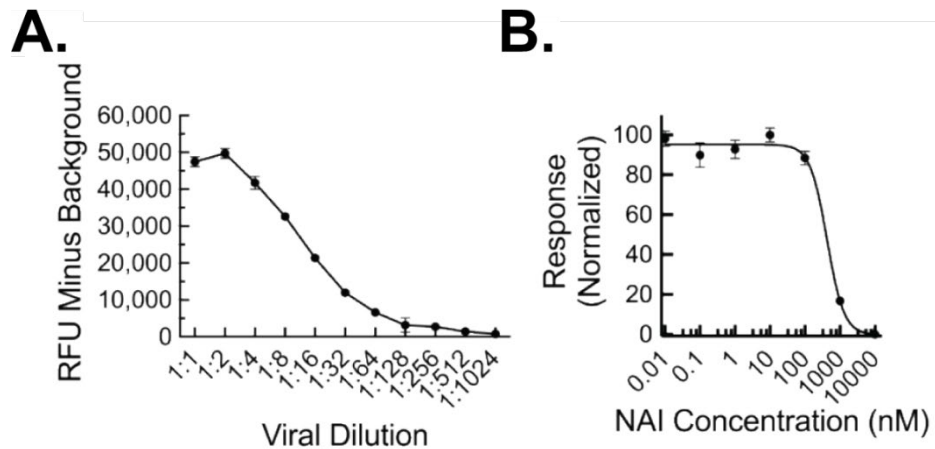
We also sought to better delineate the cellular composition of our HAE cultures as well as explore cell-type specific response profiles. To do this, we dissociated cultures after mock and IFN exposure and analyzed the cells using the inDrop method for single-cell RNAseq [270]. In line with previous reporting [8,10], we found the same major cell component types, as well as the rare subpopulation of cells referred to as ionocytes. We next compared the response to either type I (i.e. IFN β) or type III (i.e. IFN λ_3) as delivered from either the apical or basolateral compartment among each of the main cell types (i.e. ciliated cells, basal cells, goblet cells, club cells). Interestingly, while the response to type III in all four major cell types was similar regardless of whether the exposure was restricted to the apical or basolateral compartment, a subset of ISGs were more potently stimulated by type I IFN from the basolateral compartment relative to the apical.

When we compared the IFN response profile by cell type, we found the existence of a more “generalized” response pattern among all cell types. However, we also found cell-type specific IFN-driven responses. For instance, after IFN stimulation CXCL10 expression was restricted to basal cells whereas CD38 was restricted to ciliated cells. We sought to validate these cell-type specific findings on a protein level. Indeed, through flow cytometry we found that while MX1 could be detected in cells regardless of the basal cell marker, KRT5, CXCL10 was restricted to a subset of KRT5-positive cells. Similarly, CD38 was restricted to cells also staining positive for a ciliated cell marker. Moreover, both IAV

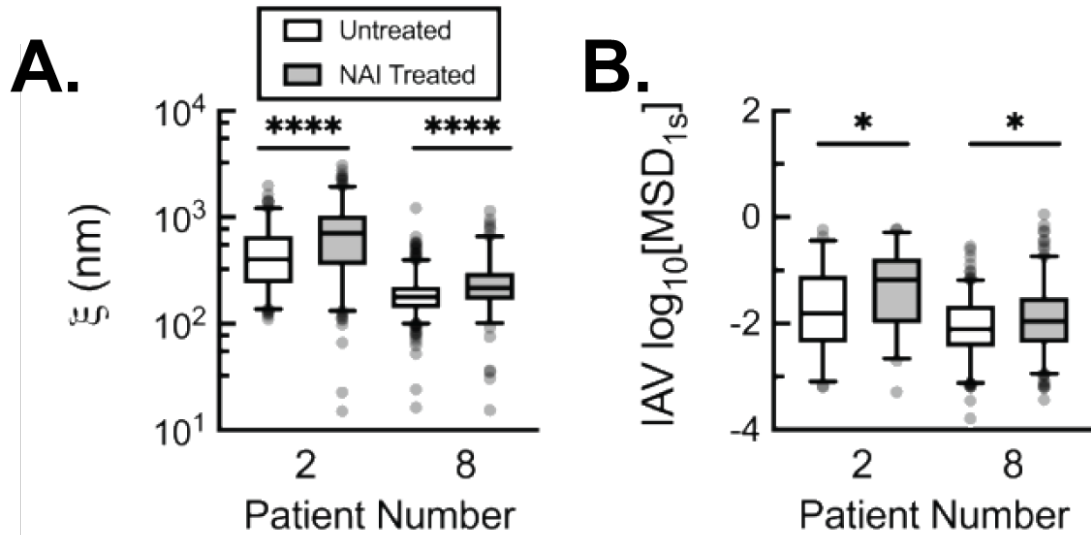
and SARS-CoV-2 infections were able to drive the ciliated cell-specific expression of CD38 in HAE. While restriction of some ISGs to basal cells (e.g. CXCL10) makes sense given their proximity to the vasculature of the lung for leukocyte extravasation, the exact function and consequence of such a restricted expression program is yet to be explored.

A main goal of this dissertation was to explore the intrinsic defensive capabilities of both secreted and tethered mucins on IAV infection. In pursuit of the former, we have expanded on previous virion tracking studies to delineate the contribution of mucus microstructure on IAV diffusivity. Additionally, we have created the synthetic mucin array apparatus which will allow for further study on the virus-host interactions centered on the secreted mucus gel. By exploring the role of tethered mucins on IAV infection of HAE, we have unexpectedly found IFN-driven expression of MUC1 in an expanded cell population of HAE. Additionally, we have established and optimized a pipeline to deplete any target of interest within an immortalized HAE line. In Chapter 5 we also characterized the cell composition of our HAE culture system and expanded our understanding of the IFN-responsive capabilities of HAE. In doing so, we have also characterized cell-type specific responses to type I and type III IFN by apical and basolateral stimulation on the single-cell level. To that end, we have confirmed the cell-type specific response profile of select ISGs and, in the future, we hope to delineate the phenotypic consequence of these cell-specific expression profiles. Overall, our work here serves to expand our understanding of how viruses overcome innate barriers to infection at the epithelial surface and offer finer granularity to IFN dynamics within the HAE.

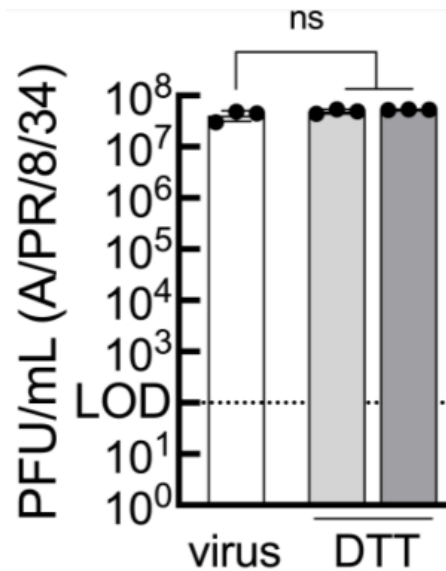
Chapter 7 : Appendices



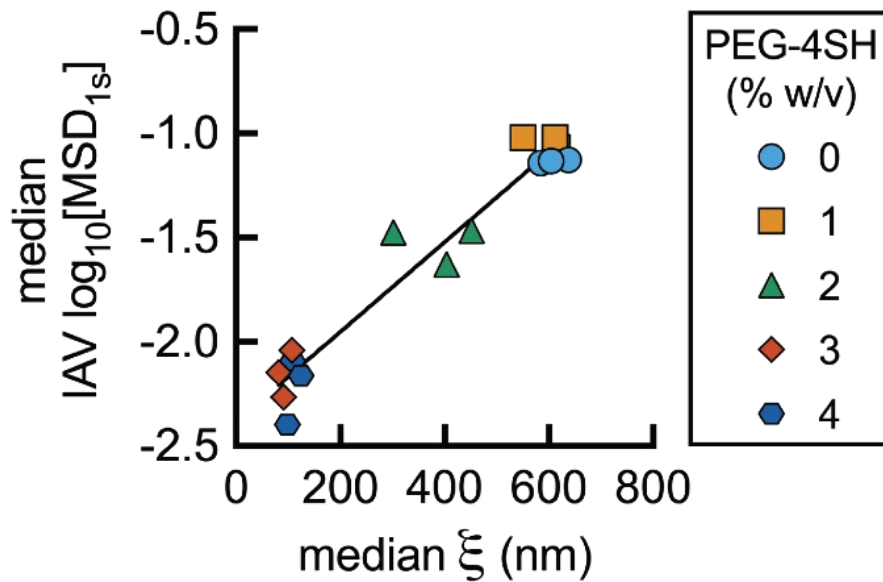
Supplementary Figure 3.1. High Concentration of Zanamivir Potently Inhibits the NA Activity of IAV. (A) Neuraminidase activity of unlabeled A/PR/8/34 at indicated dilutions. (B) Neuraminidase activity of unlabeled A/PR/8/34 (at 1:16 dilution) following incubation with indicated concentration of zanamivir. Inhibition curve: $Y = -0.3021 + (95.7421) / (1 + 10^{((2.630 - X) * -1.797)})$. Error bars are indicative of the standard deviation across technical replicates from one experimental replicate.



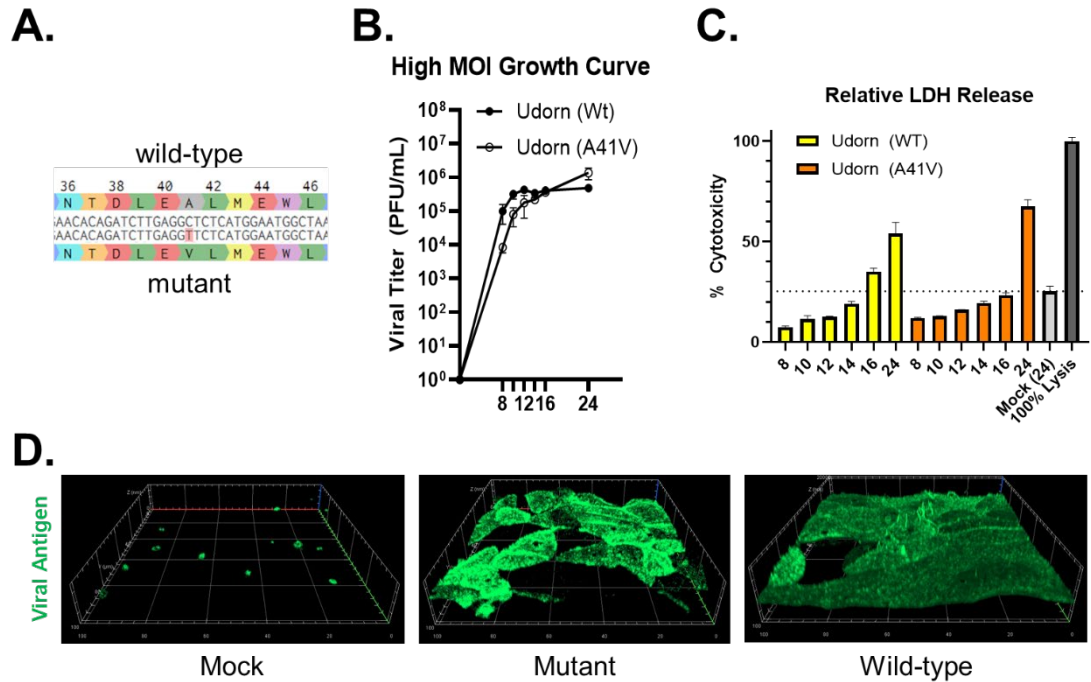
Supplementary Figure 3.2. NAI Addition Leads to Altered Microstructure of Some Mucus Samples Concomitant with IAV Diffusivity. (A) Calculated pore size (ξ) in untreated (white) and NAI treated (zanamivir; 10 μM final concentration; grey) based on PS-NP diffusion in human mucus of indicated patient number. (B) Diffusivity of A/PR/8/34 in the corresponding samples as in A. Whiskers are drawn down to the 5th percentile, up to the 95th percentile, and outliers are plotted as points. Data set statistically analyzed with two-tailed Mann-Whitney test: ns = not significant; $p > 0.05$, $*p < 0.05$, $**p < 0.01$, $***p < 0.001$, $****p < 0.0001$.



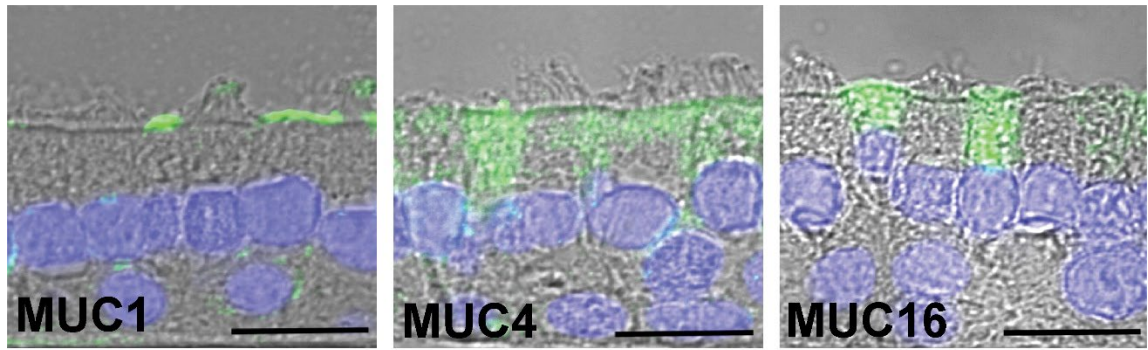
Supplementary Figure 3.3. DTT Does Not Impact IAV Infectivity at Doses Capable of Altering Mucus Microstructure. Viral titer of A/PR/8/34 following 30-minute incubation with (5 mM [light grey] and 10 mM [dark grey]) and without (white) and dithiothreitol (DTT). Data representative of three biological replicates with error bars indicating standard deviation. Experimental results were analyzed by Mann-Whitney U test (ns = non-significant).



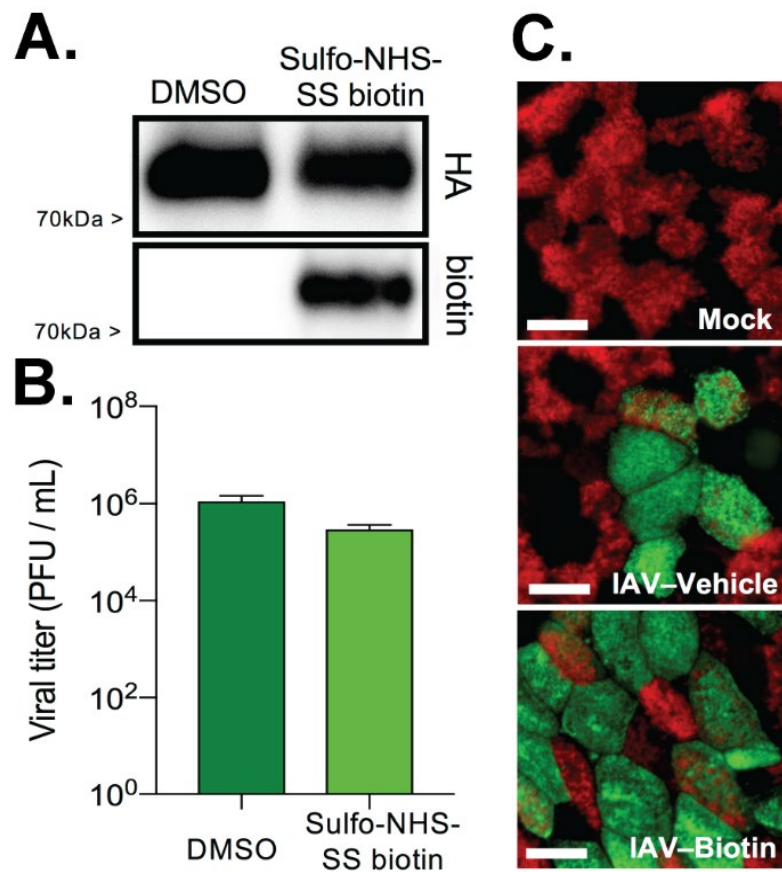
Supplementary Figure 3.4. Median Mucus Pore Size Correlates with IAV Diffusivity. Median gel pore size (ξ) calculated from the PS-NP compared to the median \log_{10} MSD value for the IAV particles in synthetic mucus of varying crosslinking densities, $R^2 = 0.9435$.



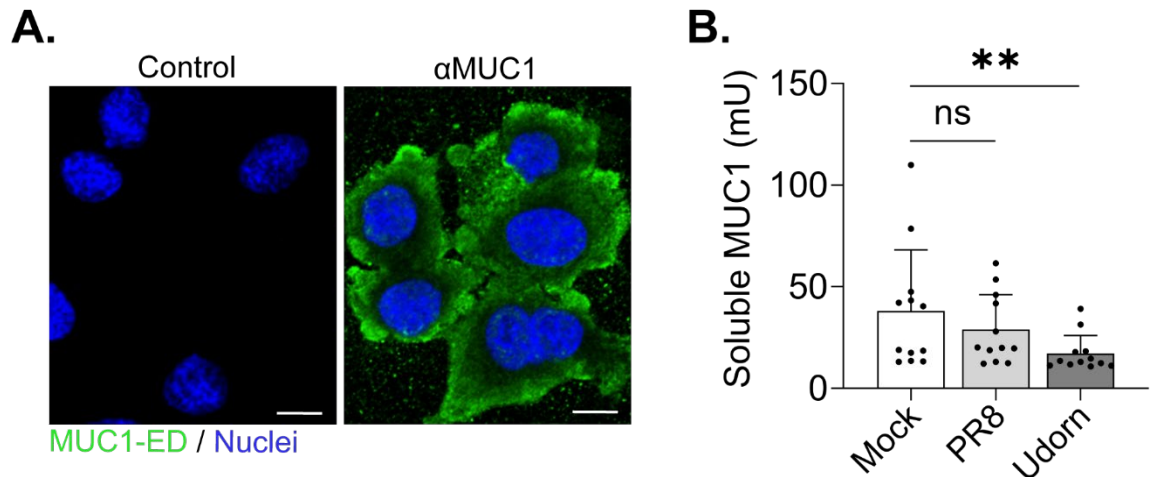
Supplementary Figure 3.5. Comparison of Pleomorphic and Monomorphic IAV with Nearly Isogenic Background. (A) Genetic composition of A/Udorn/307/72 (wild type) compared to the spherical mutant (mutant) at indicated amino acid positions of segment seven (matrix protein 1 coding sequence pictured). The mutant has the mutation C147U resulting in a coding change of M1 A41V. (B) Growth curve of wild type (Wt) and mutant (A41V) at indicated time points following a high MOI (3) inoculum on MDCK cells to facilitate rapid virion production. (C) Cytotoxicity analysis of supernatant from the infection experiment carried out in (B). (D) Confocal imaging of viral antigen (hemagglutinin) at 8 hpi in mock, mutant-infected, and wild type-infected MDCK cells. Error bars indicate the standard deviation.



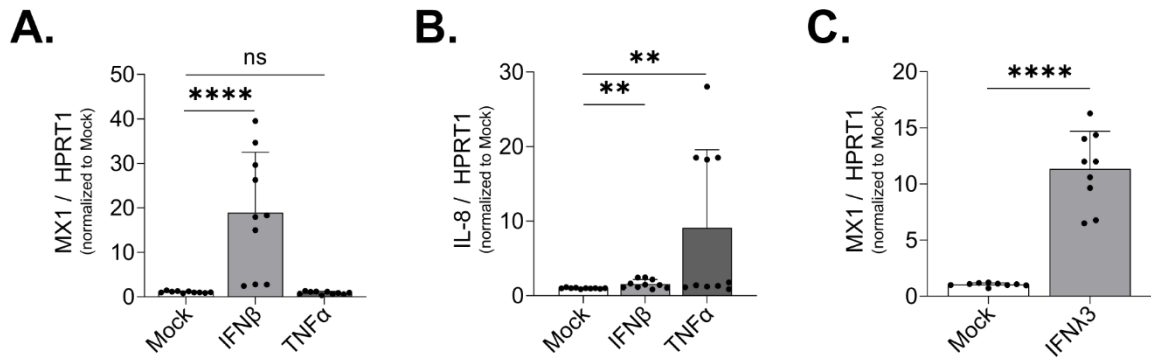
Supplementary Figure 4.1. HAE Express Three Abundant Tethered Mucins. Normal HAE were fixed and processed for histology prior to immunostaining for tethered mucins MUC1, MUC4, and MUC16 (green). Scale bar = 20 μm.



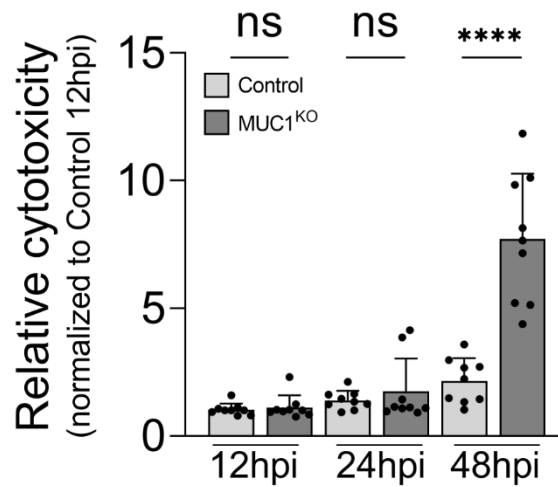
Supplementary Figure 4.2. Biotinylation of IAV has Minimal Impact on Viral Titer and Tropism. Equal amounts of A/Udorn/307/72 were biotinylated with Sulfo-NHS-SS biotin prior to analysis by (A) Western blot, (B) plaque assay, and (C) *en face* immunostaining after 24 hpi infection on HAE. In (C), ciliated cells are indicated by red and viral antigen indicated by green. Error bars indicate the standard deviation.



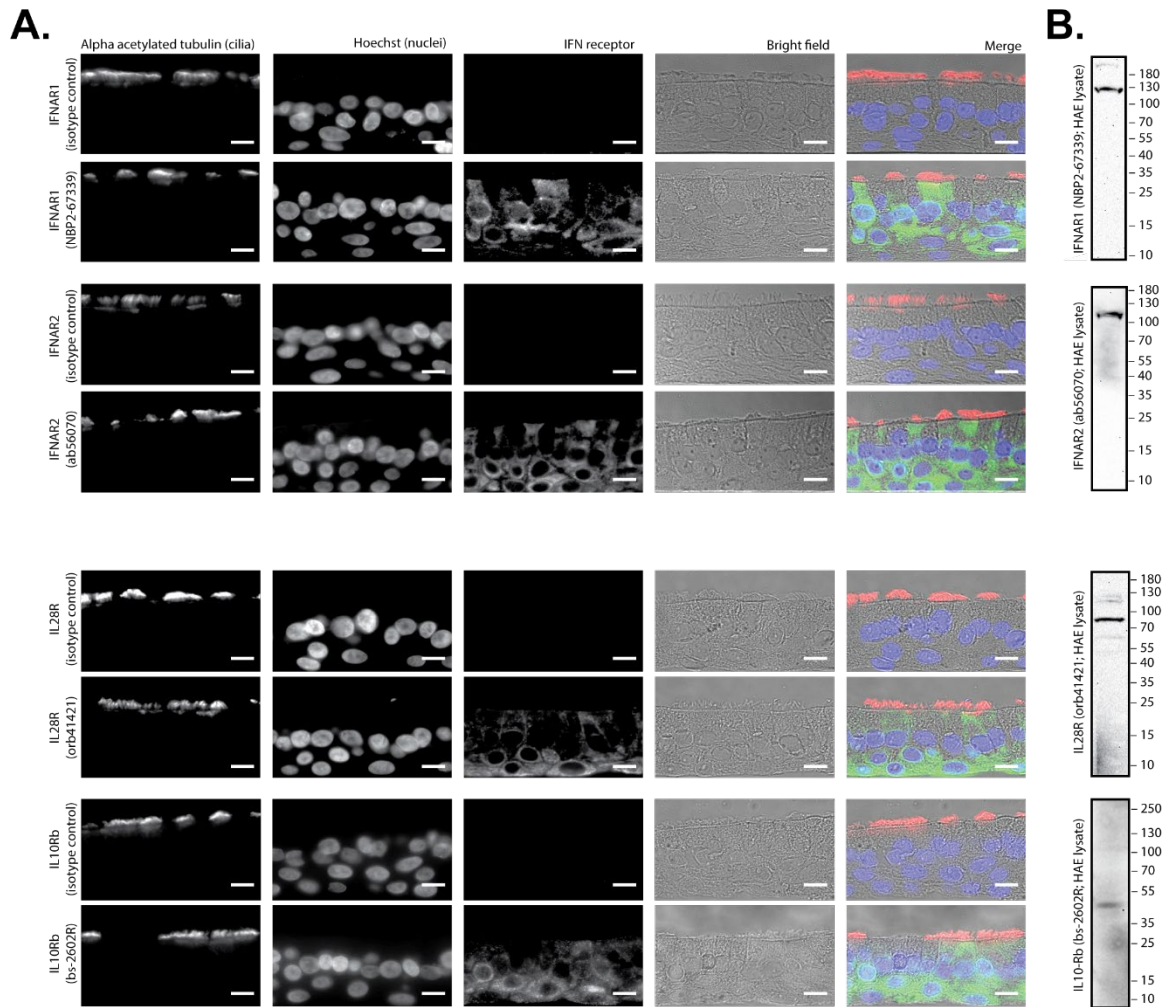
Supplementary Figure 4.3. A549 Express MUC1 at Baseline but Do Not Shed It Following IFN Infection. (A) A549 cells were stained for the extracellular domain of MUC1 and nuclei. Scale bar = 50 μ m. In (B), A549 cells were infected with IAV as indicated and MUC1 in the cell culture supernatants 24 hours post-infection was quantified by ELISA. Results from four experimental replicates were analyzed by Mann-Whitney U test compared to mock condition (ns = not significant; ** $p < 0.0021$). Error bars indicate the standard deviation.

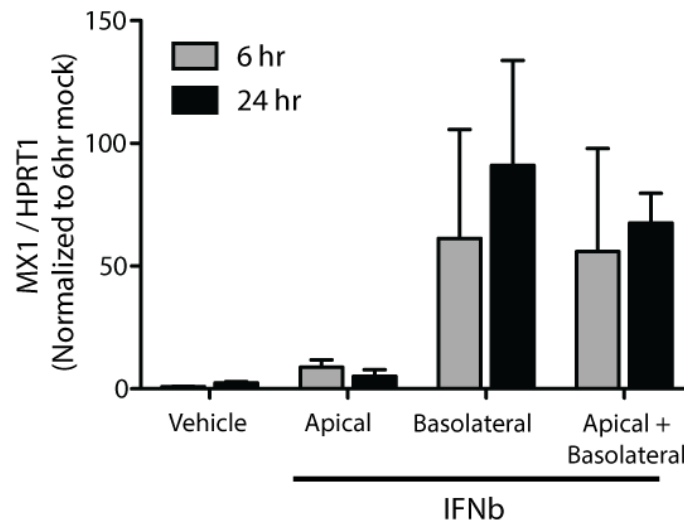


Supplementary Figure 4.4. Expression of canonical interferon-stimulated genes and inflammatory chemokines in HAE following cytokine stimulation. HAE were stimulated with recombinant human IFN β , TNF α , or mock conditions for 24 hours. Total RNA was then collected and (A) MX1 and (B) IL-8 expression analyzed by qPCR. In (C) HAE were stimulated with recombinant IFN λ 3 for 24 hours prior to RNA collection and qPCR quantification of MX1 as before. Results from three experimental replicates and three unique donors were analyzed by Mann-Whitney U test compared to mock conditions (ns = not significant; ** $p < 0.0021$; **** $p < 0.0001$). Error bars indicate the standard deviation.



Supplementary Figure 4.7. Relative cytotoxicity increases substantially at later time points during IAV infection in HAE. Relative cytotoxicity in MUC1-depleted and control HAE following IAV infection determined by quantification of lactate dehydrogenase levels in apical washes at indicated time points. Results from three experimental replicates were analyzed by Mann-Whitney U test compared to control cultures of the same time point (ns = not significant; **** $p < 0.0001$). Error bars indicate the standard deviation.





Supplementary Figure 5.2. IFN β Induces MX1 Expression in HAE Following Differential Compartment Stimulus. RT-qPCR of MX1 relative to control gene HPRT1 expression following IFN β (1 nM) stimulation by indicated compartment route. Results are normalized to vehicle conditions at 6 hours. Error bars indicate the standard deviation.

References

1. Iverson E, Kaler L, Agostino EL, Song D, Duncan GA, Scull MA. Leveraging 3D Model Systems to Understand Viral Interactions with the Respiratory Mucosa. *Viruses*. 2020 Dec;12(12):1425.
2. Terjung R, editor. *Comprehensive Physiology* [Internet]. 1st ed. Wiley; 2011 [cited 2021 Dec 9]. Available from: <https://onlinelibrary.wiley.com/doi/book/10.1002/cphy>
3. Stamati K, Mudera V, Cheema U. Evolution of oxygen utilization in multicellular organisms and implications for cell signalling in tissue engineering. *J Tissue Eng*. 2011 Nov 16;2(1):2041731411432365.
4. Widdicombe JH, Wine JJ. Airway Gland Structure and Function. *Physiol Rev*. 2015 Oct;95(4):1241–319.
5. Schittny JC. Development of the lung. *Cell Tissue Res*. 2017 Mar 1;367(3):427–44.
6. Wiebe BM, Laursen H. Human lung volume, alveolar surface area, and capillary length. *Microscopy Research and Technique*. 1995;32(3):255–62.
7. Mercer RR, Russell ML, Roggli VL, Crapo JD. Cell number and distribution in human and rat airways. *Am J Respir Cell Mol Biol*. 1994 Jun;10(6):613–24.
8. Montoro DT, Haber AL, Biton M, Vinarsky V, Lin B, Birket SE, et al. A revised airway epithelial hierarchy includes CFTR-expressing ionocytes. *Nature*. 2018 Aug;560(7718):319–24.
9. Ruysseveldt E, Martens K, Steelant B. Airway Basal Cells, Protectors of Epithelial Walls in Health and Respiratory Diseases. *Frontiers in Allergy* [Internet]. 2021 [cited 2022 Apr 18];2. Available from: <https://www.frontiersin.org/article/10.3389/falgy.2021.787128>
10. Deprez M, Zaragosi LE, Truchi M, Becavin C, Ruiz García S, Arguel MJ, et al. A Single-cell Atlas of the Human Healthy Airways. *Am J Respir Crit Care Med*. 2020 Jul 29;
11. Rokicki W, Rokicki M, Wojtacha J, Dżeljjli A. The role and importance of club cells (Clara cells) in the pathogenesis of some respiratory diseases. *Kardiochir Torakochirurgia Pol*. 2016 Mar;13(1):26–30.
12. Barnes PJ. Club Cells, Their Secretory Protein, and COPD. *CHEST*. 2015 Jun 1;147(6):1447–8.
13. Pilon AL. Rationale for the Development of Recombinant Human CC10 as a Therapeutic for Inflammatory and Fibrotic Disease. *Annals of the New York Academy of Sciences*. 2000;923(1):280–99.

14. Button B, Cai LH, Ehre C, Kesimer M, Hill DB, Sheehan JK, et al. A periciliary brush promotes the lung health by separating the mucus layer from airway epithelia. *Science*. 2012;337(6097):937–41.
15. Kesimer M, Ehre C, Burns KA, Davis CW, Sheehan JK, Pickles RJ. Molecular organization of the mucins and glycocalyx underlying mucus transport over mucosal surfaces of the airways. *Mucosal Immunology*. 2013 Mar;6(2):379–92.
16. Okuda K, Chen G, Subramani DB, Wolf M, Gilmore RC, Kato T, et al. Localization of Secretory Mucins MUC5AC and MUC5B in Normal/Healthy Human Airways. *Am J Respir Crit Care Med*. 2019 Mar 15;199(6):715–27.
17. Hattstrup CL, Gendler SJ. Structure and Function of the Cell Surface (Tethered) Mucins. *Annual Review of Physiology*. 2008 Mar;70(1):431–57.
18. Stannard W, O’Callaghan C. Ciliary function and the role of cilia in clearance. *J Aerosol Med*. 2006;19(1):110–5.
19. Stonebraker JR, Wagner D, Lefensty RW, Burns K, Gendler SJ, Bergelson JM, et al. Glycocalyx Restricts Adenoviral Vector Access to Apical Receptors Expressed on Respiratory Epithelium In Vitro and In Vivo: Role for Tethered Mucins as Barriers to Luminal Infection. *J Virol*. 2004 Dec;78(24):13755–68.
20. Ma J, Rubin BK, Voynow JA. Mucins, Mucus, and Goblet Cells. *Chest*. 2018 Jul;154(1):169–76.
21. Thornton DJ, Rousseau K, McGuckin MA. Structure and function of the polymeric mucins in airways mucus. *Annu Rev Physiol*. 2008;70:459–86.
22. Rogers DF. The airway goblet cell. *The International Journal of Biochemistry & Cell Biology*. 2003 Jan;35(1):1–6.
23. Fujisawa T, Velichko S, Thai P, Hung LY, Huang F, Wu R. Regulation of Airway MUC5AC Expression by IL-1 β and IL-17A; the NF- κ B Paradigm. *J Immunol*. 2009 Nov 15;183(10):6236–43.
24. Park JA, Tschumperlin DJ. Chronic Intermittent Mechanical Stress Increases MUC5AC Protein Expression. *Am J Respir Cell Mol Biol*. 2009 Oct 1;41(4):459–66.
25. Bonser LR, Zlock L, Finkbeiner W, Erle DJ. Epithelial tethering of MUC5AC-rich mucus impairs mucociliary transport in asthma. *J Clin Invest*. 2016 Jun 1;126(6):2367–71.
26. Kesimer M, Makhov AM, Griffith JD, Verdugo P, Sheehan JK. Unpacking a gel-forming mucin: a view of MUC5B organization after granular release. *Am J Physiol Lung Cell Mol Physiol*. 2010 Jan;298(1):L15–22.
27. Bansil R, Turner BS. The biology of mucus: Composition, synthesis and organization. *Adv Drug Deliv Rev*. 2018 15;124:3–15.

28. Henderson AG, Ehre C, Button B, Abdullah LH, Cai LH, Leigh MW, et al. Cystic fibrosis airway secretions exhibit mucin hyperconcentration and increased osmotic pressure. *J Clin Invest*. 2014 Jul;124(7):3047–60.
29. Duncan GA, Jung J, Hanes J, Suk JS. The Mucus Barrier to Inhaled Gene Therapy. *Mol Ther*. 2016 Dec;24(12):2043–53.
30. J W, T S, K R. Selective permeability of mucus barriers. *Curr Opin Biotechnol*. 2018 Apr 16;52:124–33.
31. Duncan GA, Kim N, Colon-Cortes Y, Rodriguez J, Mazur M, Birket SE, et al. An Adeno-Associated Viral Vector Capable of Penetrating the Mucus Barrier to Inhaled Gene Therapy. *Mol Ther Methods Clin Dev*. 2018 Jun 15;9:296–304.
32. Palmai-Pallag T, Khodabukus N, Kinarsky L, Leir SH, Sherman S, Hollingsworth MA, et al. The role of the SEA (sea urchin sperm protein, enterokinase and agrin) module in cleavage of membrane-tethered mucins. *The FEBS Journal*. 2005;272(11):2901–11.
33. Blalock TD, Spurr-Michaud SJ, Tisdale AS, Gipson IK. Release of Membrane-Associated Mucins from Ocular Surface Epithelia. *Invest Ophthalmol Vis Sci*. 2008 May 1;49(5):1864–71.
34. Thathiah A, Carson DD. MT1-MMP mediates MUC1 shedding independent of TACE/ADAM17. *Biochem J*. 2004 Aug 15;382(1):363–73.
35. Thathiah A, Blobel CP, Carson DD. Tumor Necrosis Factor- α Converting Enzyme/ADAM 17 Mediates MUC1 Shedding. *J Biol Chem*. 2003 Jan 31;278(5):3386–94.
36. Hanson R, Hollingsworth M. Functional Consequences of Differential O-glycosylation of MUC1, MUC4, and MUC16 (Downstream Effects on Signaling). *Biomolecules*. 2016 Jul 30;6(3):34.
37. Lu W, Hisatsune A, Koga T, Kato K, Kuwahara I, Lillehoj EP, et al. Cutting Edge: Enhanced Pulmonary Clearance of *Pseudomonas aeruginosa* by Muc1 Knockout Mice. *The Journal of Immunology*. 2006 Apr 1;176(7):3890–4.
38. Carson DD. The Cytoplasmic Tail of MUC1: A Very Busy Place. *Science Signaling*. 2008 Jul 8;1(27):pe35–pe35.
39. Wei X, Xu H, Kufe D. MUC1 Oncoprotein Stabilizes and Activates Estrogen Receptor α . *Molecular Cell*. 2006 Jan 20;21(2):295–305.
40. Escher TE, Lui AJ, Geanes ES, Walter KR, Tawfik O, Hagan CR, et al. Interaction Between MUC1 and STAT1 Drives IFITM1 Overexpression in Aromatase Inhibitor-Resistant Breast Cancer Cells and Mediates Estrogen-Induced Apoptosis. *Mol Cancer Res*. 2019 May;17(5):1180–94.

41. Bitler BG, Goverdhan A, Schroeder JA. MUC1 regulates nuclear localization and function of the epidermal growth factor receptor. *J Cell Sci.* 2010 May 15;123(10):1716–23.
42. Milara J, Morell A, Ballester B, Armengot M, Morcillo E, Cortijo J. MUC4 impairs the anti-inflammatory effects of corticosteroids in patients with chronic rhinosinusitis with nasal polyps. *Journal of Allergy and Clinical Immunology.* 2017 Mar 1;139(3):855–862.e13.
43. Das S, Majhi PD, Al-Mugotir MH, Rachagani S, Sorgen P, Batra SK. Membrane proximal ectodomain cleavage of MUC16 occurs in the acidifyingGolgi/post-Golgi compartments. *Sci Rep.* 2015 Jun 5;5(1):9759.
44. Bonser L, Erle D. Airway Mucus and Asthma: The Role of MUC5AC and MUC5B. *JCM.* 2017 Nov 29;6(12):112.
45. Ostedgaard LS, Price MP, Whitworth KM, Abou Alaiwa MH, Fischer AJ, Warriar A, et al. Lack of airway submucosal glands impairs respiratory host defenses. *Königshoff M, Morrissey EE, editors. eLife.* 2020 Oct 7;9:e59653.
46. Smith DJ, Gaffney EA, Blake JR. A model of tracer transport in airway surface liquid. *Bull Math Biol.* 2007 Apr;69(3):817–36.
47. Chu KK, Unglert C, Ford TN, Cui D, Carruth RW, Singh K, et al. In vivo imaging of airway cilia and mucus clearance with micro-optical coherence tomography. *Biomed Opt Express.* 2016 Jul 1;7(7):2494–505.
48. Matsui H, Randell SH, Peretti SW, Davis CW, Boucher RC. Coordinated clearance of periciliary liquid and mucus from airway surfaces. *J Clin Invest.* 1998 Sep 15;102(6):1125–31.
49. Cooper JL, Quinton PM, Ballard ST. Mucociliary transport in porcine trachea: differential effects of inhibiting chloride and bicarbonate secretion. *American Journal of Physiology-Lung Cellular and Molecular Physiology.* 2013 Feb 1;304(3):L184–90.
50. Oldenburg AL, Chhetri RK, Hill DB, Button B. Monitoring airway mucus flow and ciliary activity with optical coherence tomography. *Biomed Opt Express.* 2012 Sep 1;3(9):1978–92.
51. Sedaghat MH, Shahmardan MM, Norouzi M, Heydari M. Effect of Cilia Beat Frequency on Muco-ciliary Clearance. *J Biomed Phys Eng.* 2016 Dec;6(4):265–78.
52. Song D, Iverson E, Kaler L, Bader S, Scull MA, Duncan GA. Modeling Airway Dysfunction in Asthma Using Synthetic Mucus Biomaterials. *ACS Biomater Sci Eng* [Internet]. 2021 Apr 19 [cited 2021 Apr 20]; Available from: <https://doi.org/10.1021/acsbomaterials.0c01728>
53. Carpenter J, Wang Y, Gupta R, Li Y, Haridass P, Subramani DB, et al. Assembly and organization of the N-terminal region of mucin MUC5AC: Indications for structural and functional distinction from MUC5B. *PNAS* [Internet]. 2021 Sep 28

[cited 2021 Sep 29];118(39). Available from:
<https://www.pnas.org/content/118/39/e2104490118>

54. Rogers DF. Mucociliary dysfunction in COPD: effect of current pharmacotherapeutic options. *Pulm Pharmacol Ther.* 2005;18(1):1–8.
55. Elgeti J, Gompper G. Emergence of metachronal waves in cilia arrays. *Proc Natl Acad Sci USA.* 2013 Mar 19;110(12):4470–5.
56. Bustamante-Marin XM, Ostrowski LE. Cilia and Mucociliary Clearance. *Cold Spring Harb Perspect Biol* [Internet]. 2017 Apr [cited 2020 Oct 18];9(4). Available from: <https://www.ncbi.nlm.nih.gov/pmc/articles/PMC5378048/>
57. Loiseau E. Active mucus–cilia hydrodynamic coupling drives self-organization of human bronchial epithelium. *Nature Physics.* :14.
58. Smith DJ, Gaffney EA, Blake JR. Modelling mucociliary clearance. *Respir Physiol Neurobiol.* 2008 Nov 30;163(1–3):178–88.
59. Mogensen TH. Pathogen Recognition and Inflammatory Signaling in Innate Immune Defenses. *Clinical Microbiology Reviews.* 2009 Apr;22(2):240.
60. Singh H, Koury J, Kaul M. Innate Immune Sensing of Viruses and Its Consequences for the Central Nervous System. *Viruses.* 2021 Jan 23;13(2):170.
61. Goldstein ME, Scull MA. Modeling Innate Antiviral Immunity in Physiological Context. *Journal of Molecular Biology.* 2021 Dec;167374.
62. Liu T, Zhang L, Joo D, Sun SC. NF- κ B signaling in inflammation. *Sig Transduct Target Ther.* 2017 Jul 14;2(1):1–9.
63. Oyler-Yaniv J, Oyler-Yaniv A, Maltz E, Wollman R. TNF controls a speed-accuracy tradeoff in the cell death decision to restrict viral spread. *Nat Commun.* 2021 Dec;12(1):2992.
64. McNab F, Mayer-Barber K, Sher A, Wack A, O'Garra A. Type I interferons in infectious disease. *Nat Rev Immunol.* 2015 Feb;15(2):87–103.
65. Lazear HM, Nice TJ, Diamond MS. Interferon- λ : Immune Functions at Barrier Surfaces and Beyond. *Immunity.* 2015 Jul 21;43(1):15–28.
66. Ye L, Schnepf D, Staeheli P. Interferon- λ orchestrates innate and adaptive mucosal immune responses. *Nature Reviews Immunology.* 2019 Oct;19(10):614–25.
67. Galani IE, Triantafyllia V, Eleminiadou EE, Koltsida O, Stavropoulos A, Manioudaki M, et al. Interferon- λ Mediates Non-redundant Front-Line Antiviral Protection against Influenza Virus Infection without Compromising Host Fitness. *Immunity.* 2017 May;46(5):875–890.e6.
68. Zhou J hua, Wang Y ning, Chang Q yan, Ma P, Hu Y, Cao X. Type III Interferons in Viral Infection and Antiviral Immunity. *CPB.* 2018;51(1):173–85.

69. Davis AS, Chertow DS, Moyer JE, Suzich J, Sandouk A, Dorward DW, et al. Validation of Normal Human Bronchial Epithelial Cells as a Model for Influenza A Infections in Human Distal Trachea. *J Histochem Cytochem*. 2015 May;63(5):312–28.
70. Kesimer M, Kirkham S, Pickles RJ, Henderson AG, Alexis NE, DeMaria G, et al. Tracheobronchial air-liquid interface cell culture: a model for innate mucosal defense of the upper airways? *American Journal of Physiology-Lung Cellular and Molecular Physiology*. 2009 Jan 1;296(1):L92–100.
71. Zeng H, Goldsmith CS, Maines TR, Belser JA, Gustin KM, Pekosz A, et al. Tropism and Infectivity of Influenza Virus, Including Highly Pathogenic Avian H5N1 Virus, in Ferret Tracheal Differentiated Primary Epithelial Cell Cultures. *Journal of Virology*. 2013 Mar 1;87(5):2597–607.
72. Newby CM, Rowe RK, Pekosz A. Influenza A virus infection of primary differentiated airway epithelial cell cultures derived from Syrian golden hamsters. *Virology*. 2006 Oct 10;354(1):80–90.
73. You Y, Richer EJ, Huang T, Brody SL. Growth and differentiation of mouse tracheal epithelial cells: selection of a proliferative population. *American Journal of Physiology-Lung Cellular and Molecular Physiology*. 2002 Dec 1;283(6):L1315–21.
74. Kondo M, Tamaoki J, Takeyama K, Nakata J, Nagai A. Interleukin-13 Induces Goblet Cell Differentiation in Primary Cell Culture from Guinea Pig Tracheal Epithelium. *Am J Respir Cell Mol Biol*. 2002 Nov 1;27(5):536–41.
75. Leslie Fulcher M, Gabriel S, Burns KA, Yankaskas JR, Randell SH. Well-Differentiated Human Airway Epithelial Cell Cultures. In: *Human Cell Culture Protocols* [Internet]. New Jersey: Humana Press; 2004 [cited 2021 Dec 14]. p. 183–206. Available from: <http://link.springer.com/10.1385/1-59259-861-7:183>
76. Karp PH, Moninger TO, Weber SP, Nesselhauf TS, Launspach JL, Zabner J, et al. An In Vitro Model of Differentiated Human Airway Epithelia: Methods for Establishing Primary Cultures. In: *Epithelial Cell Culture Protocols* [Internet]. New Jersey: Humana Press; 2002 [cited 2021 Dec 14]. p. 115–37. Available from: <http://link.springer.com/10.1385/1-59259-185-X:115>
77. Firth AL, Dargitz CT, Qualls SJ, Menon T, Wright R, Singer O, et al. Generation of multiciliated cells in functional airway epithelia from human induced pluripotent stem cells. *Proc Natl Acad Sci U S A*. 2014 Apr 29;111(17):E1723–30.
78. Firth AL, Menon T, Parker GS, Qualls SJ, Lewis BM, Ke E, et al. Functional Gene Correction for Cystic Fibrosis in Lung Epithelial Cells Generated From Patient iPSCs. *Cell Rep*. 2015 Sep 1;12(9):1385–90.
79. Wong AP, Bear CE, Chin S, Pasceri P, Thompson TO, Huan LJ, et al. Directed differentiation of human pluripotent stem cells into mature airway epithelia expressing functional CFTR protein. *Nat Biotechnol*. 2012 Sep;30(9):876–82.

80. Hawkins FJ, Suzuki S, Beermann ML, Barillà C, Wang R, Villacorta-Martin C, et al. Derivation of Airway Basal Stem Cells from Human Pluripotent Stem Cells. *Cell Stem Cell*. 2021 Jan 7;28(1):79-95.e8.
81. Kuek LE, Griffin P, Martinello P, Graham AN, Kalitsis P, Robinson PJ, et al. Identification of an Immortalized Human Airway Epithelial Cell Line with Dyskinetic Cilia. *Am J Respir Cell Mol Biol*. 2018;59(3):375–82.
82. Rayner RE, Makena P, Prasad GL, Cormet-Boyaka E. Optimization of Normal Human Bronchial Epithelial (NHBE) Cell 3D Cultures for in vitro Lung Model Studies. *Scientific Reports*. 2019 24;9(1):500.
83. Munye MM, Shoemark A, Hirst RA, Delhove JM, Sharp TV, McKay TR, et al. BMI-1 extends proliferative potential of human bronchial epithelial cells while retaining their mucociliary differentiation capacity. *Am J Physiol Lung Cell Mol Physiol*. 2017 Feb 1;312(2):L258–67.
84. Chandrala LD, Afshar-Mohajer N, Nishida K, Ronzhes Y, Sidhaye VK, Koehler K, et al. A Device for measuring the in-situ response of Human Bronchial Epithelial Cells to airborne environmental agents. *Sci Rep*. 2019 Dec;9(1):7263.
85. Tarran R, Button B, Picher M, Paradiso AM, Ribeiro CM, Lazarowski ER, et al. Normal and cystic fibrosis airway surface liquid homeostasis. The effects of phasic shear stress and viral infections. *J Biol Chem*. 2005 Oct 21;280(42):35751–9.
86. Derichs N, Jin B, Song Y, Finkbeiner WE, Verkman AS. Hyperviscous airway periciliary and mucous liquid layers in cystic fibrosis measured by confocal fluorescence photobleaching. *FASEB j*. 2011 Jul;25(7):2325–32.
87. Farberman MM, Ibricevic A, Joseph TD, Akers KT, Garcia-Medina R, Crosby S, et al. Effect of Polarized Release of CXC-Chemokines from Wild-Type and Cystic Fibrosis Murine Airway Epithelial Cells. *Am J Respir Cell Mol Biol*. 2011 Aug 1;45(2):221–8.
88. Tarran R, Trout L, Donaldson SH, Boucher RC. Soluble Mediators, Not Cilia, Determine Airway Surface Liquid Volume in Normal and Cystic Fibrosis Superficial Airway Epithelia. *Journal of General Physiology*. 2006 Apr 24;127(5):591–604.
89. Lakshmi SP, Reddy AT, Banno A, Reddy RC. Airway Epithelial Cell Peroxisome Proliferator-Activated Receptor γ Regulates Inflammation and Mucin Expression in Allergic Airway Disease. *J Immunol*. 2018 Sep 15;201(6):1775–83.
90. Sotty J, Garçon G, Denayer FO, Alleman LY, Saleh Y, Perdrix E, et al. Toxicological effects of ambient fine (PM_{2.5-0.18}) and ultrafine (PM_{0.18}) particles in healthy and diseased 3D organo-typic mucociliary-phenotype models. *Environmental Research*. 2019 Sep 1;176:108538.
91. Stewart CE, Torr EE, Mohd Jamili NH, Bosquillon C, Sayers I. Evaluation of Differentiated Human Bronchial Epithelial Cell Culture Systems for Asthma Research [Internet]. Vol. 2012, *Journal of Allergy*. Hindawi; 2012 [cited 2020 Dec 5]. p. e943982. Available from: <https://www.hindawi.com/journals/ja/2012/943982/>

92. Parker J, Sarlang S, Thavagnanam S, Williamson G, O'Donoghue D, Villenave R, et al. A 3-D Well-Differentiated Model of Pediatric Bronchial Epithelium Demonstrates Unstimulated Morphological Differences Between Asthmatic and Nonasthmatic Cells. *Pediatr Res*. 2010 Jan;67(1):17–22.
93. Hackett TL, Singhera GK, Shaheen F, Hayden P, Jackson GR, Hegele RG, et al. Intrinsic Phenotypic Differences of Asthmatic Epithelium and Its Inflammatory Responses to Respiratory Syncytial Virus and Air Pollution. *Am J Respir Cell Mol Biol*. 2011 Nov 1;45(5):1090–100.
94. Mertens TCJ, Karmouty-Quintana H, Taube C, Hiemstra PS. Use of airway epithelial cell culture to unravel the pathogenesis and study treatment in obstructive airway diseases. *Pulmonary Pharmacology & Therapeutics*. 2017 Aug 1;45:101–13.
95. Leclercq B, Happillon M, Antherieu S, Hardy EM, Alleman LY, Grova N, et al. Differential responses of healthy and chronic obstructive pulmonary diseased human bronchial epithelial cells repeatedly exposed to air pollution-derived PM₄. *Environ Pollut*. 2016 Nov;218:1074–88.
96. Liu X, Ory V, Chapman S, Yuan H, Albanese C, Kallakury B, et al. ROCK Inhibitor and Feeder Cells Induce the Conditional Reprogramming of Epithelial Cells. *Am J Pathol*. 2012 Feb;180(2):599–607.
97. Supryniewicz FA, Upadhyay G, Krawczyk E, Kramer SC, Hebert JD, Liu X, et al. Conditionally reprogrammed cells represent a stem-like state of adult epithelial cells. *PNAS*. 2012 Dec 4;109(49):20035–40.
98. Walters MS, Gomi K, Ashbridge B, Moore MAS, Arbelaez V, Heldrich J, et al. Generation of a human airway epithelium derived basal cell line with multipotent differentiation capacity. *Respir Res*. 2013 Dec 3;14:135.
99. Chu HW, Rios C, Huang C, Wesolowska-Andersen A, Burchard EG, O'Connor BP, et al. CRISPR–Cas9-mediated gene knockout in primary human airway epithelial cells reveals a proinflammatory role for MUC18. *Gene Therapy*. 2015 Oct;22(10):822–9.
100. Everman JL, Sajuthi S, Saef B, Rios C, Stoner AM, Numata M, et al. Functional genomics of CDHR3 confirms its role in HRV-C infection and childhood asthma exacerbations. *Journal of Allergy and Clinical Immunology*. 2019 Oct 1;144(4):962–71.
101. Koh KD, Siddiqui S, Cheng D, Bonser LR, Sun DI, Zlock LT, et al. Efficient RNP-directed Human Gene Targeting Reveals SPDEF Is Required for IL-13-induced Mucostasis. *Am J Respir Cell Mol Biol*. 2020 Mar;62(3):373–81.
102. Walker PJ, Siddell SG, Lefkowitz EJ, Mushegian AR, Adriaenssens EM, Dempsey DM, et al. Changes to virus taxonomy and the Statutes ratified by the International Committee on Taxonomy of Viruses (2020). *Arch Virol*. 2020 Nov;165(11):2737–48.

103. Parry R, Wille M, Turnbull OMH, Geoghegan JL, Holmes EC. Divergent Influenza-Like Viruses of Amphibians and Fish Support an Ancient Evolutionary Association. *Viruses*. 2020 Sep;12(9):1042.
104. Arunkumar GA, Bhavsar D, Li T, Strohmeier S, Chromikova V, Amanat F, et al. Functionality of the putative surface glycoproteins of the Wuhan spiny eel influenza virus. *Nat Commun*. 2021 Oct 25;12(1):6161.
105. Content J. Cell-free translation of influenza virus mRNA. *J Virol*. 1976 May;18(2):604–18.
106. Krug RM, Morgan MA, Shatkin AJ. Influenza viral mRNA contains internal N6-methyladenosine and 5'-terminal 7-methylguanosine in cap structures. *J Virol*. 1976 Oct;20(1):45–53.
107. McGeoch D, Fellner P, Newton C. Influenza virus genome consists of eight distinct RNA species. *Proceedings of the National Academy of Sciences*. 1976 Sep 1;73(9):3045–9.
108. Etkind PR, Krug RM. Purification of influenza viral complementary RNA: its genetic content and activity in wheat germ cell-free extracts. *Journal of Virology* [Internet]. 1975 Dec [cited 2022 Jan 3]; Available from: <https://journals.asm.org/doi/abs/10.1128/jvi.16.6.1464-1475.1975>
109. Baltimore D. Expression of animal virus genomes. *BACTERIOL REV*. 1971;35:7.
110. Smith W, Andrewes CH, Laidlaw PP. A VIRUS OBTAINED FROM INFLUENZA PATIENTS. *Lancet (London, England)*. 1933 Jul 8;222(5732):66–8.
111. Francis T. A New Type of Virus from Epidemic Influenza. *Science*. 1940 Nov 1;92(2392):405–8.
112. Taylor RM. Studies on Survival of Influenza Vitus Between Epidemics and Antigenic Variants of the Virus. 1949;39:8.
113. Sederdahl BK, Williams JV. Epidemiology and Clinical Characteristics of Influenza C Virus. *Viruses*. 2020 Jan 13;12(1):89.
114. Caini S, Kuszniarz G, Garate VV, Wangchuk S, Thapa B, de Paula Júnior FJ, et al. The epidemiological signature of influenza B virus and its B/Victoria and B/Yamagata lineages in the 21st century. *PLoS One*. 2019 Sep 12;14(9):e0222381.
115. Cohen C, Kleynhans J, Moyes J, McMorow ML, Treurnicht FK, Hellferscee O, et al. Asymptomatic transmission and high community burden of seasonal influenza in an urban and a rural community in South Africa, 2017–18 (PHIRST): a population cohort study. *The Lancet Global Health*. 2021 Jun 1;9(6):e863–74.
116. Endo A, Uchida M, Kucharski AJ, Funk S. Fine-scale family structure shapes influenza transmission risk in households: Insights from primary schools in Matsumoto city, 2014/15. *PLOS Computational Biology*. 2019 Dec 26;15(12):e1007589.

117. Iuliano AD, Roguski KM, Chang HH, Muscatello DJ, Palekar R, Tempia S, et al. Estimates of global seasonal influenza-associated respiratory mortality: a modelling study. *The Lancet*. 2018 Mar 31;391(10127):1285–300.
118. Thompson WW, Weintraub E, Dhankhar P, Cheng PY, Brammer L, Meltzer MI, et al. Estimates of US influenza-associated deaths made using four different methods. *Influenza and Other Respiratory Viruses*. 2009 Jan 1;3(1):37–49.
119. Estimated Flu-Related Illnesses, Medical Visits, Hospitalizations, and Deaths in the United States — 2017–2018 Flu Season | CDC [Internet]. 2021 [cited 2022 Jan 4]. Available from: <https://www.cdc.gov/flu/about/burden/2017-2018.htm>
120. Taubenberger JK, Kash JC. Influenza Virus Evolution, Host Adaptation, and Pandemic Formation. *Cell Host & Microbe*. 2010 Jun;7(6):440–51.
121. Taubenberger JK, Morens DM. Pandemic influenza—including a risk assessment of H5N1. *Rev - Off Int Epizoot*. 2009 Apr;28(1):187–202.
122. Choppin P, Igortamm S. Immunological Characteristics of N. Y. Strains of Influenza A Virus From the 1957 Pandemic. (24092). :8.
123. Coleman MT, Dowdle WR. Properties of the Hong Kong influenza virus. *Bull World Health Organ*. 1969;41(3-4-5):413–8.
124. Nakajima K, Desselberger U, Palese P. Recent human influenza A (H1N1) viruses are closely related genetically to strains isolated in 1950. *Nature*. 1978 Jul;274(5669):334–9.
125. Neumann G, Noda T, Kawaoka Y. Emergence and pandemic potential of swine-origin H1N1 influenza virus. *Nature*. 2009 Jun 18;459(7249):931–9.
126. Simonsen L, Clarke MJ, Schonberger LB, Arden NH, Cox NJ, Fukuda K. Pandemic versus Epidemic Influenza Mortality: A Pattern of Changing Age Distribution. *J Infect Dis*. 1998 Jul 1;178(1):53–60.
127. Kwok KO, Riley S, Perera RAPM, Wei VWI, Wu P, Wei L, et al. Relative incidence and individual-level severity of seasonal influenza A H3N2 compared with 2009 pandemic H1N1. *BMC Infectious Diseases*. 2017 May 11;17(1):337.
128. Shrestha SS, Swerdlow DL, Borse RH, Prabhu VS, Finelli L, Atkins CY, et al. Estimating the burden of 2009 pandemic influenza A (H1N1) in the United States (April 2009-April 2010). *Clin Infect Dis*. 2011 Jan 1;52 Suppl 1:S75-82.
129. Petersen E, Koopmans M, Go U, Hamer DH, Petrosillo N, Castelli F, et al. Comparing SARS-CoV-2 with SARS-CoV and influenza pandemics. *The Lancet Infectious Diseases* [Internet]. 2020 Jul 3 [cited 2020 Jul 6];0(0). Available from: [https://www.thelancet.com/journals/laninf/article/PIIS1473-3099\(20\)30484-9/abstract](https://www.thelancet.com/journals/laninf/article/PIIS1473-3099(20)30484-9/abstract)
130. Johnson NPAS, Mueller J. Updating the Accounts: Global Mortality of the 1918-1920 “Spanish” Influenza Pandemic. *Bulletin of the History of Medicine*. 2002;76(1):105–15.

131. Faust JS, Lin Z, Rio C del. Comparison of Estimated Excess Deaths in New York City During the COVID-19 and 1918 Influenza Pandemics. *JAMA Netw Open*. 2020 Aug 3;3(8):e2017527–e2017527.
132. Taubenberger JK, Morens DM. The Pathology of Influenza Virus Infections. *Annu Rev Pathol*. 2008;3:499–522.
133. Wolff GG. Influenza vaccination and respiratory virus interference among Department of Defense personnel during the 2017–2018 influenza season. *Vaccine* [Internet]. 2019 Oct 10 [cited 2019 Oct 18]; Available from: <http://www.sciencedirect.com/science/article/pii/S0264410X19313647>
134. Wu A, Mihaylova VT, Landry ML, Foxman EF. Interference between rhinovirus and influenza A virus: a clinical data analysis and experimental infection study. *The Lancet Microbe* [Internet]. 2020 Sep 4 [cited 2020 Sep 7];0(0). Available from: [https://www.thelancet.com/journals/lanmic/article/PIIS2666-5247\(20\)30114-2/abstract](https://www.thelancet.com/journals/lanmic/article/PIIS2666-5247(20)30114-2/abstract)
135. Nickbakhsh S, Mair C, Matthews L, Reeve R, Johnson PCD, Thorburn F, et al. Virus–virus interactions impact the population dynamics of influenza and the common cold. *PNAS* [Internet]. 2019 Dec 11 [cited 2019 Dec 17]; Available from: <https://www.pnas.org/content/early/2019/12/10/1911083116>
136. Matsuzaki Y, Sugawara K, Furuse Y, Shimotai Y, Hongo S, Oshitani H, et al. Genetic Lineage and Reassortment of Influenza C Viruses Circulating between 1947 and 2014. *Journal of Virology*. 90(18):8251–65.
137. Nesmith N, Williams JV, Johnson M, Zhu Y, Griffin M, Talbot HK. Sensitive Diagnostics Confirm That Influenza C is an Uncommon Cause of Medically Attended Respiratory Illness in Adults. *Clinical Infectious Diseases*. 2017 Sep 15;65(6):1037–9.
138. McCullers JA. The co-pathogenesis of influenza viruses with bacteria in the lung. *Nature Reviews Microbiology*. 2014 Apr;12(4):252–62.
139. Shirey KA, Perkins DJ, Lai W, Zhang W, Fernando LR, Gusovsky F, et al. Influenza “Trains” the Host for Enhanced Susceptibility to Secondary Bacterial Infection. *MBio*. 2019 May 7;10(3).
140. Berry I, Tuite AR, Salomon A, Drews S, Harris AD, Hatchette T, et al. Association of Influenza Activity and Environmental Conditions With the Risk of Invasive Pneumococcal Disease. *JAMA Netw Open*. 2020 Jul 1;3(7):e2010167–e2010167.
141. Shrestha S, Foxman B, Weinberger DM, Steiner C, Viboud C, Rohani P. Identifying the Interaction Between Influenza and Pneumococcal Pneumonia Using Incidence Data. *Sci Transl Med* [Internet]. 2013 Jun 26 [cited 2022 Jan 4];5(191). Available from: <https://www.science.org/doi/10.1126/scitranslmed.3005982>
142. Kobayashi SD, Olsen RJ, LaCasse RA, Safronetz D, Ashraf M, Porter AR, et al. Seasonal H3N2 influenza A virus fails to enhance *Staphylococcus aureus* co-

- infection in a non-human primate respiratory tract infection model. *Virulence*. 2013 Nov 15;4(8):707–15.
143. Katsurada N, Suzuki M, Aoshima M, Yaegashi M, Ishifuji T, Asoh N, et al. The impact of virus infections on pneumonia mortality is complex in adults: a prospective multicentre observational study. *BMC Infect Dis*. 2017 Dec 6;17(1):755.
 144. Morens DM, Taubenberger JK. The Mother of All Pandemics Is 100 Years Old (and Going Strong)! *Am J Public Health*. 2018;108(11):1449–54.
 145. Sreenivasan CC, Thomas M, Kaushik RS, Wang D, Li F. Influenza A in Bovine Species: A Narrative Literature Review. *Viruses* [Internet]. 2019 Jun 17 [cited 2020 Nov 29];11(6). Available from: <https://www.ncbi.nlm.nih.gov/pmc/articles/PMC6631717/>
 146. Worobey M, Han GZ, Rambaut A. Genesis and pathogenesis of the 1918 pandemic H1N1 influenza A virus. *Proceedings of the National Academy of Sciences*. 2014 Jun 3;111(22):8107–12.
 147. Turnbull ML, Wise HM, Nicol MQ, Smith N, Dunfee RL, Beard PM, et al. Role of the B Allele of Influenza A Virus Segment 8 in Setting Mammalian Host Range and Pathogenicity. *J Virol*. 2016 15;90(20):9263–84.
 148. Sun H, Xiao Y, Liu J, Wang D, Li F, Wang C, et al. Prevalent Eurasian avian-like H1N1 swine influenza virus with 2009 pandemic viral genes facilitating human infection. *PNAS* [Internet]. 2020 Jun 24 [cited 2020 Jun 30]; Available from: <http://www.pnas.org/content/early/2020/06/23/1921186117>
 149. Borkenhagen LK, Salman MD, Ma MJ, Gray GC. Animal influenza virus infections in humans: A commentary. *International Journal of Infectious Diseases*. 2019 Nov 1;88:113–9.
 150. Gonzalez G, Marshall JF, Morrell J, Robb D, McCauley JW, Perez DR, et al. Infection and Pathogenesis of Canine, Equine, and Human Influenza Viruses in Canine Tracheas. *Journal of Virology* [Internet]. 2014 Aug 15 [cited 2022 Jan 4]; Available from: <https://journals.asm.org/doi/abs/10.1128/JVI.00887-14>
 151. Gagnon CA, Spearman G, Hamel A, Godson DL, Fortin A, Fontaine G, et al. Characterization of a Canadian Mink H3N2 Influenza A Virus Isolate Genetically Related to Triple Reassortant Swine Influenza Virus. *Journal of Clinical Microbiology* [Internet]. 2009 Mar [cited 2022 Jan 4]; Available from: <https://journals.asm.org/doi/abs/10.1128/JCM.01228-08>
 152. Gong X, Hu M, Chen W, Yang H, Wang B, Yue J, et al. Reassortment Network of Influenza A Virus. *Frontiers in Microbiology*. 2021;12:3759.
 153. Worobey M, Han GZ, Rambaut A. A synchronized global sweep of the internal genes of modern avian influenza virus. *Nature*. 2014 Apr 10;508(7495):254–7.
 154. Lycett SJ, Duchatel F, Digard P. A brief history of bird flu. *Philos Trans R Soc Lond, B, Biol Sci*. 2019 Jun 24;374(1775):20180257.

155. Mayr J, Lau K, Lai JCC, Gagarinov IA, Shi Y, McAtamney S, et al. Unravelling the Role of O -glycans in Influenza A Virus Infection. *Scientific Reports*. 2018 Nov 6;8(1):1–12.
156. Benton DJ, Gamblin SJ, Rosenthal PB, Skehel JJ. Structural transitions in influenza haemagglutinin at membrane fusion pH. *Nature*. 2020 May 27;1–4.
157. Matlin KS, Reggio H, Helenius A, Simons K. Infectious entry pathway of influenza virus in a canine kidney cell line. *J Cell Biol*. 1981 Dec;91(3 Pt 1):601–13.
158. Byrd-Leotis L, Gao C, Jia N, Mehta A, Trost J, Cummings SF, et al. Antigenic pressure on H3N2 influenza drift strains imposes constraints on binding to sialylated receptors, but not phosphorylated glycans. *Journal of Virology*. 2019 Sep 4;JVI.01178-19.
159. Air GM. Influenza neuraminidase: Influenza neuraminidase. *Influenza and Other Respiratory Viruses*. 2012 Jul;6(4):245–56.
160. Yang X, Steukers L, Forier K, Xiong R, Braeckmans K, Reeth KV, et al. A Beneficiary Role for Neuraminidase in Influenza Virus Penetration through the Respiratory Mucus. *PLOS ONE*. 2014 Oct 15;9(10):e110026.
161. Matrosovich M, Tuzikov A, Bovin N, Gambaryan A, Klimov A, Castrucci MR, et al. Early alterations of the receptor-binding properties of H1, H2, and H3 avian influenza virus hemagglutinins after their introduction into mammals. *J Virol*. 2000 Sep;74(18):8502–12.
162. Pekosz A, Newby C, Bose PS, Lutz A. Sialic acid recognition is a key determinant of influenza A virus tropism in murine trachea epithelial cell cultures. *Virology*. 2009 Mar 30;386(1):61–7.
163. Vries E de, Du W, Guo H, Haan CAM de. Influenza A Virus Hemagglutinin–Neuraminidase–Receptor Balance: Preserving Virus Motility. *Trends in Microbiology*. 2020 Jan 1;28(1):57–67.
164. Kosik I, Yewdell JW. Influenza Hemagglutinin and Neuraminidase: Yin–Yang Proteins Coevolving to Thwart Immunity. *Viruses*. 2019 Apr;11(4):346.
165. Scull MA, Gillim-Ross L, Santos C, Roberts KL, Bordonali E, Subbarao K, et al. Avian Influenza Virus Glycoproteins Restrict Virus Replication and Spread through Human Airway Epithelium at Temperatures of the Proximal Airways. Fouchier RAM, editor. *PLoS Pathogens*. 2009 May 15;5(5):e1000424.
166. Webster RG, Darlington RW. Disruption of Myxoviruses with Tween 20 and Isolation of Biologically Active Hemagglutinin and Neuraminidase Subunits. *J VIROL*. 1969;4:6.
167. Bouvier NM, Palese P. THE BIOLOGY OF INFLUENZA VIRUSES. *Vaccine*. 2008 Sep 12;26(Suppl 4):D49–53.

168. Vahey MD, Fletcher DA. Low-Fidelity Assembly of Influenza A Virus Promotes Escape from Host Cells. *Cell* [Internet]. 2018 Nov 29 [cited 2018 Dec 4]; Available from: <http://www.sciencedirect.com/science/article/pii/S0092867418314557>
169. Lamb RA, Choppin PW. Identification of a second protein (M2) encoded by RNA segment 7 of influenza virus. *Virology*. 1981 Jul 30;112(2):729–37.
170. Mosley VM, Wyckoff RWG. Electron micrography of the virus of influenza. *Nature*. 1946 Mar 2;157:263.
171. Chu CM, Dawson IM, Elford WJ. Filamentous forms associated with newly isolated influenza virus. *Lancet*. 1949 Apr 9;1(6554):602.
172. Sugita Y, Noda T, Sagara H, Kawaoka Y. Ultracentrifugation deforms unfixed influenza A virions. *J Gen Virol*. 2011 Nov;92(Pt 11):2485–93.
173. Hayase Y, Uno F, Nii S. Ultrahigh-resolution scanning electron microscopy of MDCK cells infected with influenza viruses. *J Electron Microsc (Tokyo)*. 1995 Oct;44(5):281–8.
174. Halldorsson S, Sader K, Turner J, Calder LJ, Rosenthal PB. In situ structure and organization of the influenza C virus surface glycoprotein. *Nat Commun*. 2021 Mar 16;12(1):1694.
175. Dadonaite B, Vijayakrishnan S, Fodor E, Bhella D, Hutchinson EC. Filamentous influenza viruses. *Journal of General Virology*. 2016 Aug 1;97(8):1755–64.
176. Calder LJ, Wasilewski S, Berriman JA, Rosenthal PB. Structural organization of a filamentous influenza A virus. *PNAS*. 2010 Jun 8;107(23):10685–90.
177. Harris A, Cardone G, Winkler DC, Heymann JB, Brecher M, White JM, et al. Influenza virus pleiomorphy characterized by cryoelectron tomography. *Proc Natl Acad Sci USA*. 2006 Dec 12;103(50):19123–7.
178. Wang D, Harmon A, Jin J, Francis DH, Christopher-Hennings J, Nelson E, et al. The Lack of an Inherent Membrane Targeting Signal Is Responsible for the Failure of the Matrix (M1) Protein of Influenza A Virus To Bud into Virus-Like Particles. *Journal of Virology* [Internet]. 2010 May [cited 2022 Feb 21]; Available from: <https://journals.asm.org/doi/abs/10.1128/JVI.02306-09>
179. Leser GP, Lamb RA. Lateral Organization of Influenza Virus Proteins in the Budozone Region of the Plasma Membrane. *Journal of Virology*. 2017;91(9):e02104-16.
180. Leser GP, Lamb RA. Influenza virus assembly and budding in raft-derived microdomains: A quantitative analysis of the surface distribution of HA, NA and M2 proteins. *Virology*. 2005 Nov 25;342(2):215–27.
181. McCown MF, Pekosz A. Distinct Domains of the Influenza A Virus M2 Protein Cytoplasmic Tail Mediate Binding to the M1 Protein and Facilitate Infectious Virus Production. *J Virol*. 2006 Aug 15;80(16):8178–89.

182. Chen BJ, Leser GP, Jackson D, Lamb RA. The Influenza Virus M2 Protein Cytoplasmic Tail Interacts with the M1 Protein and Influences Virus Assembly at the Site of Virus Budding. *J Virol*. 2008 Oct;82(20):10059–70.
183. Fan H, Walker AP, Carrique L, Keown JR, Martin IS, Karia D, et al. Structures of influenza A virus RNA polymerase offer insight into viral genome replication. *Nature*. 2019 Sep 4;1–4.
184. Fodor E, te Velthuis AJW. Structure and Function of the Influenza Virus Transcription and Replication Machinery. *Cold Spring Harb Perspect Med*. 2019 Dec 23;a038398.
185. Carrique L, Fan H, Walker AP, Keown JR, Sharps J, Staller E, et al. Host ANP32A mediates the assembly of the influenza virus replicase. *Nature*. 2020 Nov;587(7835):638–43.
186. Noda T. Native Morphology of Influenza Virions. *Front Microbiol* [Internet]. 2012 Jan 3 [cited 2018 Apr 12];2. Available from: <https://www.ncbi.nlm.nih.gov/pmc/articles/PMC3249889/>
187. Noda T, Sugita Y, Aoyama K, Hirase A, Kawakami E, Miyazawa A, et al. Three-dimensional analysis of ribonucleoprotein complexes in influenza A virus. *Nature Communications*. 2012 Jan 24;3:639.
188. Noda T, Murakami S, Nakatsu S, Imai H, Muramoto Y, Shindo K, et al. Importance of the 1+7 configuration of ribonucleoprotein complexes for influenza A virus genome packaging. *Nature Communications*. 2018 Jan 4;9(1):54.
189. Nakatsu S, Murakami S, Shindo K, Horimoto T, Sagara H, Noda T, et al. Influenza C and D viruses package eight organized ribonucleoprotein complexes. *J Virol*. 2018 Jan 10;JVI.02084-17.
190. Goto H, Muramoto Y, Noda T, Kawaoka Y. The Genome-Packaging Signal of the Influenza A Virus Genome Comprises a Genome Incorporation Signal and a Genome-Bundling Signal. *Journal of Virology*. 2013 Nov;87(21):11316–22.
191. Einfeld AJ, Neumann G, Kawaoka Y. At the centre: influenza A virus ribonucleoproteins. *Nature Reviews Microbiology*. 2014 Nov 24;13(1):28–41.
192. Chou Y y., Vafabakhsh R, Doganay S, Gao Q, Ha T, Palese P. One influenza virus particle packages eight unique viral RNAs as shown by FISH analysis. *Proceedings of the National Academy of Sciences*. 2012 Jun 5;109(23):9101–6.
193. Noda T, Sagara H, Yen A, Takada A, Kida H, Cheng RH, et al. Architecture of ribonucleoprotein complexes in influenza A virus particles. *Nature*. 2006 Jan 26;439(7075):490–2.
194. Suzuki Y, Ito T, Suzuki T, Holland RE, Chambers TM, Kiso M, et al. Sialic Acid Species as a Determinant of the Host Range of Influenza A Viruses. *Journal of Virology*. 2000 Dec 15;74(24):11825–31.

195. Nicholls JM, Bourne AJ, Chen H, Guan Y, Peiris JM. Sialic acid receptor detection in the human respiratory tract: evidence for widespread distribution of potential binding sites for human and avian influenza viruses. *Respir Res.* 2007;8(1):73.
196. Tumpey TM, Maines TR, Hoeven NV, Glaser L, Solórzano A, Pappas C, et al. A Two-Amino Acid Change in the Hemagglutinin of the 1918 Influenza Virus Abolishes Transmission. *Science.* 2007 Feb 2;315(5812):655–9.
197. Pappas C, Viswanathan K, Chandrasekaran A, Raman R, Katz JM, Sasisekharan R, et al. Receptor Specificity and Transmission of H2N2 Subtype Viruses Isolated from the Pandemic of 1957. *PLOS ONE.* 2010 Jun 21;5(6):e11158.
198. Zhang W, Shi Y, Qi J, Gao F, Li Q, Fan Z, et al. Molecular Basis of the Receptor Binding Specificity Switch of the Hemagglutinins from both the 1918 and 2009 Pandemic Influenza A Viruses by a D225G Substitution. *J Virol.* 2013 May;87(10):5949–58.
199. Corfield AP. Mucins: a biologically relevant glycan barrier in mucosal protection. *Biochim Biophys Acta.* 2015 Jan;1850(1):236–52.
200. Cohen M, Zhang XQ, Senaati HP, Chen HW, Varki NM, Schooley RT, et al. Influenza A penetrates host mucus by cleaving sialic acids with neuraminidase. *Virology Journal.* 2013;10(1):321.
201. Matrosovich MN, Matrosovich TY, Gray T, Roberts NA, Klenk HD. Neuraminidase Is Important for the Initiation of Influenza Virus Infection in Human Airway Epithelium. *J Virol.* 2004 Nov 15;78(22):12665–7.
202. Sakai T, Nishimura SI, Naito T, Saito M. Influenza A virus hemagglutinin and neuraminidase act as novel motile machinery. *Sci Rep [Internet].* 2017 Mar 27;7. Available from: <https://www.ncbi.nlm.nih.gov/pmc/articles/PMC5366856/>
203. Ohuchi M, Asaoka N, Sakai T, Ohuchi R. Roles of neuraminidase in the initial stage of influenza virus infection. *Microbes and Infection.* 2006 Apr;8(5):1287–93.
204. Reiter-Scherer V, Cuellar-Camacho JL, Bhatia S, Haag R, Herrmann A, Lauster D, et al. Force Spectroscopy Shows Dynamic Binding of Influenza Hemagglutinin and Neuraminidase to Sialic Acid. *Biophysical Journal.* 2019 Mar 19;116(6):1037–48.
205. Vahey MD, Fletcher DA. Influenza A virus surface proteins are organized to help penetrate host mucus. Chakraborty AK, Neher RA, Neher RA, Zanin M, editors. *eLife.* 2019 May 14;8:e43764.
206. Zhou X, Zhao M, Liu Y, Chen Q, Shen L. Statistical Binding Matching between Influenza A Virus and Dynamic Glycan Clusters Determines Its Adhesion onto Lipid Membranes. *Langmuir.* 2020 Dec 12;acs.langmuir.0c02047.

207. Rust MJ, Lakadamyali M, Zhang F, Zhuang X. Assembly of endocytic machinery around individual influenza viruses during viral entry. *Nat Struct Mol Biol.* 2004 Jun;11(6):567–73.
208. Eierhoff T, Hrinčius ER, Rescher U, Ludwig S, Ehrhardt C. The epidermal growth factor receptor (EGFR) promotes uptake of influenza A viruses (IAV) into host cells. *PLoS Pathog.* 2010 Sep 9;6(9):e1001099.
209. Honigfort DJ, Altman MO, Gagneux P, Godula K. Glycocalyx crowding with mucin mimetics strengthens binding of soluble and virus-associated lectins to host cell glycan receptors. *PNAS* [Internet]. 2021 Oct 5 [cited 2021 Sep 29];118(40). Available from: <https://www.pnas.org/content/118/40/e2107896118>
210. Rossman JS, Leser GP, Lamb RA. Filamentous Influenza Virus Enters Cells via Macropinocytosis. *Journal of Virology.* 2012 Oct 15;86(20):10950–60.
211. de Vries E, Tscherne DM, Wienholts MJ, Cobos-Jiménez V, Scholte F, García-Sastre A, et al. Dissection of the Influenza A Virus Endocytic Routes Reveals Macropinocytosis as an Alternative Entry Pathway. Pekosz A, editor. *PLoS Pathogens.* 2011 Mar 31;7(3):e1001329.
212. Mercer J, Helenius A. Virus entry by macropinocytosis. *Nat Cell Biol.* 2009 May;11(5):510–20.
213. Banerjee I, Yamauchi Y, Helenius A, Horvath P. High-Content Analysis of Sequential Events during the Early Phase of Influenza A Virus Infection. *PLOS ONE.* 2013 Jul 12;8(7):e68450.
214. Ivanovic T, Harrison SC. Distinct functional determinants of influenza hemagglutinin-mediated membrane fusion. *eLife* [Internet]. [cited 2018 Sep 5];4. Available from: <https://www.ncbi.nlm.nih.gov/pmc/articles/PMC4755761/>
215. Ivanovic T, Choi JL, Whelan SP, van Oijen AM, Harrison SC. Influenza-virus membrane fusion by cooperative fold-back of stochastically induced hemagglutinin intermediates. *eLife* [Internet]. 2013 Feb 19 [cited 2017 Sep 5];2. Available from: <http://elifesciences.org/lookup/doi/10.7554/eLife.00333>
216. Desai TM, Marin M, Chin CR, Savidis G, Brass AL, Melikyan GB. IFITM3 Restricts Influenza A Virus Entry by Blocking the Formation of Fusion Pores following Virus-Endosome Hemifusion. Basler CF, editor. *PLoS Pathogens.* 2014 Apr 3;10(4):e1004048.
217. Calder LJ, Rosenthal PB. Cryomicroscopy provides structural snapshots of influenza virus membrane fusion. *Nat Struct Mol Biol.* 2016 Sep;23(9):853–8.
218. Lee KK. Architecture of a nascent viral fusion pore. *EMBO J.* 2010 Apr 7;29(7):1299–311.
219. Manzoor R, Igarashi M, Takada A. Influenza A Virus M2 Protein: Roles from Ingress to Egress. *International Journal of Molecular Sciences.* 2017 Dec 7;18(12):2649.

220. Li S, Sieben C, Ludwig K, Höfer CT, Chiantia S, Herrmann A, et al. pH-Controlled Two-Step Uncoating of Influenza Virus. *Biophys J*. 2014 Apr 1;106(7):1447–56.
221. Larson GP, Tran V, Yú S, Cai Y, Higgins CA, Smith DM, et al. EPS8 facilitates uncoating of influenza A virus. *bioRxiv*. 2019 Mar 28;592485.
222. Banerjee I, Miyake Y, Nobs SP, Schneider C, Horvath P, Kopf M, et al. Influenza A virus uses the aggresome processing machinery for host cell entry. *Science*. 2014 Oct 24;346(6208):473–7.
223. Qin C, Li W, Li Q, Yin W, Zhang X, Zhang Z, et al. Real-time dissection of dynamic uncoating of individual influenza viruses. *Proceedings of the National Academy of Sciences*. 2019 Feb 12;116(7):2577–82.
224. Chou Y ying, Heaton NS, Gao Q, Palese P, Singer R, Lionnet T. Colocalization of Different Influenza Viral RNA Segments in the Cytoplasm before Viral Budding as Shown by Single-molecule Sensitivity FISH Analysis. *PLOS Pathogens*. 2013 May 9;9(5):e1003358.
225. Lukarska M, Fournier G, Pflug A, Resa-Infante P, Reich S, Naffakh N, et al. Structural basis of an essential interaction between influenza polymerase and Pol II CTD. *Nature*. 2017 Jan;541(7635):117–21.
226. Gu W, Gallagher GR, Dai W, Liu P, Li R, Trombly MI, et al. Influenza A virus preferentially snatches noncoding RNA caps. *RNA*. 2015 Dec;21(12):2067–75.
227. Koppstein D, Ashour J, Bartel DP. Sequencing the cap-snatching repertoire of H1N1 influenza provides insight into the mechanism of viral transcription initiation. *Nucleic Acids Res*. 2015 May 26;43(10):5052–64.
228. de Rozières CM, Pequeno A, Shahabi S, Lucas TM, Godula K, Ghosh G, et al. PABP1 Drives the Selective Translation of Influenza A Virus mRNA. *Journal of Molecular Biology*. 2022 Mar 15;434(5):167460.
229. Panthu B, Terrier O, Carron C, Traversier A, Corbin A, Balvay L, et al. The NS1 Protein from Influenza Virus Stimulates Translation Initiation by Enhancing Ribosome Recruitment to mRNAs. *Journal of Molecular Biology*. 2017 Oct 27;429(21):3334–52.
230. Arias-Mireles BH, de Rozieres CM, Ly K, Joseph S. RNA Modulates the Interaction Between Influenza A Virus NS1 and Human PABP1. *Biochemistry*. 2018 Jul 3;57(26):3590–8.
231. Tran V, Ledwith MP, Thamamongood T, Higgins CA, Tripathi S, Chang MW, et al. Influenza virus repurposes the antiviral protein IFIT2 to promote translation of viral mRNAs. *Nat Microbiol*. 2020 Dec;5(12):1490–503.
232. Courtney DG, Kennedy EM, Dumm RE, Bogerd HP, Tsai K, Heaton NS, et al. Epitranscriptomic Enhancement of Influenza A Virus Gene Expression and Replication. *Cell Host & Microbe*. 2017 Sep;22(3):377-386.e5.

233. Chaimayo C, Dunagan M, Hayashi T, Santoso N, Takimoto T. Specificity and functional interplay between influenza virus PA-X and NS1 shutoff activity. *PLOS Pathogens*. 2018 Nov 29;14(11):e1007465.
234. Khapersky DA, Schmaling S, Larkins-Ford J, McCormick C, Gaglia MM. Selective Degradation of Host RNA Polymerase II Transcripts by Influenza A Virus PA-X Host Shutoff Protein. *PLoS Pathog* [Internet]. 2016 Feb 5;12(2). Available from: <https://www.ncbi.nlm.nih.gov/pmc/articles/PMC4744033/>
235. Ohkura T, Momose F, Ichikawa R, Takeuchi K, Morikawa Y. Influenza A Virus Hemagglutinin and Neuraminidase Mutually Accelerate Their Apical Targeting through Clustering of Lipid Rafts. *Journal of Virology*. 2014 Sep 1;88(17):10039–55.
236. Hughey PG, Compans RW, Zebedee SL, Lamb RA. Expression of the influenza A virus M2 protein is restricted to apical surfaces of polarized epithelial cells. *J Virol*. 1992 Sep;66(9):5542–52.
237. Neumann G. Influenza A virus NS2 protein mediates vRNP nuclear export through NES-independent interaction with hCRM1. *The EMBO Journal*. 2000 Dec 15;19(24):6751–8.
238. Alenquer M, Vale-Costa S, Etibor TA, Ferreira F, Sousa AL, Amorim MJ. Influenza A virus ribonucleoproteins form liquid organelles at endoplasmic reticulum exit sites. *Nat Commun* [Internet]. 2019 Apr 9 [cited 2019 Apr 13];10. Available from: <https://www.ncbi.nlm.nih.gov/pmc/articles/PMC6456594/>
239. Bhagwat AR, Sage VL, Nturi E, Kulej K, Jones J, Guo M, et al. Quantitative live cell imaging reveals influenza virus manipulation of Rab11A transport through reduced dynein association. *Nat Commun*. 2020 Jan 7;11(1):1–14.
240. Eisfeld AJ, Kawakami E, Watanabe T, Neumann G, Kawaoka Y. RAB11A Is Essential for Transport of the Influenza Virus Genome to the Plasma Membrane. *Journal of Virology* [Internet]. 2011 Jul 1 [cited 2022 Feb 23]; Available from: <https://journals.asm.org/doi/abs/10.1128/JVI.00378-11>
241. de Castro Martin IF, Fournier G, Sachse M, Pizarro-Cerda J, Risco C, Naffakh N. Influenza virus genome reaches the plasma membrane via a modified endoplasmic reticulum and Rab11-dependent vesicles. *Nature Communications* [Internet]. 2017 Dec [cited 2017 Nov 15];8(1). Available from: <http://www.nature.com/articles/s41467-017-01557-6>
242. Dadonaite B, Gilbertson B, Knight ML, Trifkovic S, Rockman S, Laederach A, et al. The structure of the influenza A virus genome. *Nat Microbiol*. 2019 Nov;4(11):1781–9.
243. Le Sage V, Kanarek JP, Snyder DJ, Cooper VS, Lakdawala SS, Lee N. Mapping of Influenza Virus RNA-RNA Interactions Reveals a Flexible Network. *Cell Reports*. 2020 Jun;31(13):107823.

244. Nakatsu S, Sagara H, Sakai-Tagawa Y, Sugaya N, Noda T, Kawaoka Y. Complete and Incomplete Genome Packaging of Influenza A and B Viruses. *mBio*. 7(5):e01248-16.
245. Farheen N, Thattai M. Frustration and fidelity in influenza genome assembly. *Journal of The Royal Society Interface*. 2019 Nov 29;16(160):20190411.
246. Lakdawala SS, Fodor E, Subbarao K. Moving On Out: Transport and Packaging of Influenza Viral RNA into Virions. *Annu Rev Virol*. 2016 Sep 29;3(1):411–27.
247. Simpson-Holley M, Ellis D, Fisher D, Elton D, McCauley J, Digard P. A functional link between the actin cytoskeleton and lipid rafts during budding of filamentous influenza virions. *Virology*. 2002 Sep 30;301(2):212–25.
248. Kumakura M, Kawaguchi A, Nagata K. Actin-myosin network is required for proper assembly of influenza virus particles. *Virology*. 2015 Feb 1;476:141–50.
249. Bruce EA, Digard P, Stuart AD. The Rab11 Pathway Is Required for Influenza A Virus Budding and Filament Formation. *J Virol*. 2010 Jun 15;84(12):5848–59.
250. Rossman JS, Jing X, Leser GP, Lamb RA. Influenza Virus M2 Protein Mediates ESCRT-Independent Membrane Scission. *Cell*. 2010 Sep;142(6):902–13.
251. Rossman JS, Jing X, Leser GP, Balannik V, Pinto LH, Lamb RA. Influenza Virus M2 Ion Channel Protein Is Necessary for Filamentous Virion Formation. *J Virol*. 2010 May 15;84(10):5078–88.
252. Martínez-Sobrido L, García-Sastre A. Generation of Recombinant Influenza Virus from Plasmid DNA. *JoVE*. 2010 Aug 3;(42):2057.
253. Hutchinson EC, Charles PD, Hester SS, Thomas B, Trudgian D, Martínez-Alonso M, et al. Conserved and host-specific features of influenza virion architecture. *Nature Communications*. 2014 Sep 16;5:4816.
254. Duncan GA, Jung J, Joseph A, Thaxton AL, West NE, Boyle MP, et al. Microstructural alterations of sputum in cystic fibrosis lung disease. *JCI Insight*. 2016 Nov 3;1(18):e88198.
255. Joyner K, Song D, Hawkins RF, Silcott RD, Duncan GA. A rational approach to form disulfide linked mucin hydrogels. *Soft Matter*. 2019 Dec 4;15(47):9632–9.
256. Joyner K, Yang S, Duncan GA. Microrheology for biomaterial design. *APL Bioeng*. 2020 Dec;4(4):041508.
257. Schuster BS, Ensign LM, Allan DB, Suk JS, Hanes J. Particle tracking in drug and gene delivery research: State-of-the-art applications and methods. *Adv Drug Deliv Rev*. 2015 Aug 30;91:70–91.
258. Crocker JC, Grier DG. Methods of Digital Video Microscopy for Colloidal Studies. *Journal of Colloid and Interface Science*. 1996 Apr 15;179(1):298–310.

259. Mason null, Weitz null. Optical measurements of frequency-dependent linear viscoelastic moduli of complex fluids. *Phys Rev Lett*. 1995 Feb 13;74(7):1250–3.
260. Huck BC, Hartwig O, Biehl A, Schwarzkopf K, Wagner C, Loretz B, et al. Macro- and Microrheological Properties of Mucus Surrogates in Comparison to Native Intestinal and Pulmonary Mucus. *Biomacromolecules*. 2019 Sep 9;20(9):3504–12.
261. Newby JM, Seim I, Lysy M, Ling Y, Huckaby J, Lai SK, et al. Technological strategies to estimate and control diffusive passage times through the mucus barrier in mucosal drug delivery. *Adv Drug Deliv Rev*. 2018 Jan 15;124:64–81.
262. Lee JM, Huddleston J, Doud MB, Hooper KA, Wu NC, Bedford T, et al. Deep mutational scanning of hemagglutinin helps predict evolutionary fates of human H3N2 influenza variants. *PNAS*. 2018 Aug 28;115(35):E8276–85.
263. Hoffmann E, Stech J, Guan Y, Webster RG, Perez DR. Universal primer set for the full-length amplification of all influenza A viruses. *Archives of Virology*. 2001 Dec 1;146(12):2275–89.
264. Barclay WS, Jones IM, Osborn HMI, Phillipson L, Ren J, Talevera GA, et al. Probing the receptor interactions of an H5 avian influenza virus using a baculovirus expression system and functionalised poly(acrylic acid) ligands. *Bioorganic & Medicinal Chemistry*. 2007 Jun 15;15(12):4038–47.
265. Sanjana NE, Shalem O, Zhang F. Improved vectors and genome-wide libraries for CRISPR screening. *Nat Methods*. 2014 Aug;11(8):783–4.
266. Altschul SF, Madden TL, Schäffer AA, Zhang J, Zhang Z, Miller W, et al. Gapped BLAST and PSI-BLAST: a new generation of protein database search programs. *Nucleic Acids Research*. 1997 Sep 1;25(17):3389–402.
267. Stewart SA, Dykxhoorn DM, Palliser D, Mizuno H, Yu EY, An DS, et al. Lentivirus-delivered stable gene silencing by RNAi in primary cells. *RNA*. 2003 Apr;9(4):493–501.
268. Schindelin J, Arganda-Carreras I, Frise E, Kaynig V, Longair M, Pietzsch T, et al. Fiji: an open-source platform for biological-image analysis. *Nat Methods*. 2012 Jul;9(7):676–82.
269. Zilionis R, Nainys J, Veres A, Savova V, Zemmour D, Klein AM, et al. Single-cell barcoding and sequencing using droplet microfluidics. *Nat Protoc*. 2017 Jan;12(1):44–73.
270. Klein AM, Mazutis L, Akartuna I, Tallapragada N, Veres A, Li V, et al. Droplet Barcoding for Single-Cell Transcriptomics Applied to Embryonic Stem Cells. *Cell*. 2015 May 21;161(5):1187–201.
271. Hao Y, Hao S, Andersen-Nissen E, Mauck WM, Zheng S, Butler A, et al. Integrated analysis of multimodal single-cell data. *Cell*. 2021 Jun 24;184(13):3573-3587.e29.

272. Stuart T, Butler A, Hoffman P, Hafemeister C, Papalexi E, Mauck WM, et al. Comprehensive Integration of Single-Cell Data. *Cell*. 2019 Jun 13;177(7):1888-1902.e21.
273. McGinnis CS, Murrow LM, Gartner ZJ. DoubletFinder: Doublet Detection in Single-Cell RNA Sequencing Data Using Artificial Nearest Neighbors. *cells*. 2019 Apr 24;8(4):329-337.e4.
274. Travaglini KJ, Nabhan AN, Penland L, Sinha R, Gillich A, Sit RV, et al. A molecular cell atlas of the human lung from single-cell RNA sequencing. *Nature*. 2020 Nov;587(7835):619–25.
275. O’Flanagan CH, Campbell KR, Zhang AW, Kabeer F, Lim JLP, Biele J, et al. Dissociation of solid tumor tissues with cold active protease for single-cell RNA-seq minimizes conserved collagenase-associated stress responses. *Genome Biology*. 2019 Oct 17;20(1):210.
276. Robinson MD, McCarthy DJ, Smyth GK. edgeR: a Bioconductor package for differential expression analysis of digital gene expression data. *Bioinformatics*. 2010 Jan 1;26(1):139–40.
277. Sonesson C, Robinson MD. Bias, robustness and scalability in single-cell differential expression analysis. *Nat Methods*. 2018 Apr;15(4):255–61.
278. Kaler L, Iverson E, Bader S, Song D, Scull MA, Duncan GA. Influenza A virus diffusion through mucus gel networks. *Commun Biol*. 2022 Mar 22;5(1):1–9.
279. Zanin M, Baviskar P, Webster R, Webby R. The interaction between respiratory pathogens and mucus. *Cell Host Microbe*. 2016 Feb 10;19(2):159–68.
280. Ehre C, Worthington EN, Liesman RM, Grubb BR, Barbier D, O’Neal WK, et al. Overexpressing mouse model demonstrates the protective role of Muc5ac in the lungs. *PNAS*. 2012 Oct 9;109(41):16528–33.
281. Lakdawala SS, Jayaraman A, Halpin RA, Lamirande EW, Shih AR, Stockwell TB, et al. The soft palate is an important site of adaptation for transmissible influenza viruses. *Nature*. 2015 Oct;526(7571):122.
282. Xie C, Su W, Sia SF, Choy KT, Morrell S, Zhou J, et al. A(H1N1)pdm09 influenza viruses replicating in ferret upper or lower respiratory tract differed in onward transmission potential by air. *The Journal of Infectious Diseases* [Internet]. 2021 May 24 [cited 2021 Jun 1];(jiab286). Available from: <https://doi.org/10.1093/infdis/jiab286>
283. Weber TP, Stilianakis NI. Inactivation of influenza A viruses in the environment and modes of transmission: A critical review. *Journal of Infection*. 2008 Nov 1;57(5):361–73.
284. Hirose R, Nakaya T, Naito Y, Daidoji T, Bandou R, Inoue K, et al. Situations Leading to Reduced Effectiveness of Current Hand Hygiene against Infectious Mucus from Influenza Virus-Infected Patients. *mSphere*. 2019 Oct 30;4(5):e00474-19.

285. Thomas Y, Vogel G, Wunderli W, Suter P, Witschi M, Koch D, et al. Survival of Influenza Virus on Banknotes. *Appl Environ Microbiol*. 2008 May 15;74(10):3002–7.
286. Kormuth KA, Lin K, Prussin AJ, Vejerano EP, Tiwari AJ, Cox SS, et al. Influenza Virus Infectivity Is Retained in Aerosols and Droplets Independent of Relative Humidity. *J Infect Dis* [Internet]. [cited 2018 Jun 8]; Available from: <https://academic.oup.com/jid/advance-article/doi/10.1093/infdis/jiy221/5025997>
287. Zanin M, Marathe B, Wong SS, Yoon SW, Collin E, Oshansky C, et al. Pandemic Swine H1N1 Influenza Viruses with Almost Undetectable Neuraminidase Activity Are Not Transmitted via Aerosols in Ferrets and Are Inhibited by Human Mucus but Not Swine Mucus. Perlman S, editor. *J Virol*. 2015 Jun 1;89(11):5935–48.
288. Kim N, Duncan GA, Hanes J, Suk JS. Barriers to inhaled gene therapy of obstructive lung diseases: A review. *J Control Release*. 2016 28;240:465–88.
289. Yuan S, Hollinger M, Lachowicz-Scroggins ME, Kerr SC, Dunican EM, Daniel BM, et al. Oxidation increases mucin polymer cross-links to stiffen airway mucus gels. *Sci Transl Med*. 2015 Feb 25;7(276):276ra27.
290. Schiller JL, Lai SK. Tuning Barrier Properties of Biological Hydrogels. *ACS Appl Bio Mater*. 2020 May 18;3(5):2875–90.
291. Wang YY, Harit D, Subramani DB, Arora H, Kumar PA, Lai SK. Influenza-binding antibodies immobilise influenza viruses in fresh human airway mucus. *European Respiratory Journal*. 2017 Jan 1;49(1):1601709.
292. Bao C, Liu B, Li B, Chai J, Zhang L, Jiao L, et al. Enhanced Transport of Shape and Rigidity-Tuned α -Lactalbumin Nanotubes across Intestinal Mucus and Cellular Barriers. *Nano Lett*. 2020 Feb 12;20(2):1352–61.
293. Yu M, Song W, Tian F, Dai Z, Zhu Q, Ahmad E, et al. Temperature- and rigidity-mediated rapid transport of lipid nanovesicles in hydrogels. *Proceedings of the National Academy of Sciences*. 2019 Mar 19;116(12):5362–9.
294. Schaap IAT, Eghiaian F, des Georges A, Veigel C. Effect of envelope proteins on the mechanical properties of influenza virus. *J Biol Chem*. 2012 Nov 30;287(49):41078–88.
295. Guo H, Rabouw H, Slomp A, Dai M, van der Vegt F, van Lent JWM, et al. Kinetic analysis of the influenza A virus HA/NA balance reveals contribution of NA to virus-receptor binding and NA-dependent rolling on receptor-containing surfaces. *PLoS Pathog*. 2018 Aug;14(8):e1007233.
296. Smirnov YuA, Kuznetsova MA, Kaverin NV. The genetic aspects of influenza virus filamentous particle formation. *Arch Virol*. 1991;118(3–4):279–84.
297. Elleman CJ, Barclay WS. The M1 matrix protein controls the filamentous phenotype of influenza A virus. *Virology*. 2004 Mar 30;321(1):144–53.

298. Zebedee SL, Lamb RA. Growth restriction of influenza A virus by M2 protein antibody is genetically linked to the M1 protein. *Proc Natl Acad Sci U S A*. 1989 Feb;86(3):1061–5.
299. Mileva M. Oxidative Stress as a Target for Medication of Influenza Virus Infection. *Acta Microbiol Bulg*. 2016;32(3):52.
300. Luettich K, Talikka M, Lowe FJ, Haswell LE, Park J, Gaca MD, et al. The Adverse Outcome Pathway for Oxidative Stress-Mediated EGFR Activation Leading to Decreased Lung Function. *Applied In Vitro Toxicology*. 2017 Mar;3(1):99–109.
301. Boucher RC. Muco-Obstructive Lung Diseases. *N Engl J Med*. 2019 May 16;380(20):1941–53.
302. Olmsted SS, Padgett JL, Yudin AI, Whaley KJ, Moench TR, Cone RA. Diffusion of macromolecules and virus-like particles in human cervical mucus. *Biophys J*. 2001 Oct;81(4):1930–7.
303. Hansing J, Duke JR, Fryman EB, DeRouchey JE, Netz RR. Particle Diffusion in Polymeric Hydrogels with Mixed Attractive and Repulsive Interactions. *Nano Lett*. 2018 Aug 8;18(8):5248–56.
304. Fatin-Rouge N, Starchev K, Buffle J. Size Effects on Diffusion Processes within Agarose Gels. *Biophys J*. 2004 May;86(5):2710–9.
305. Spero RC, Sircar RK, Schubert R, Taylor RM, Wolberg AS, Superfine R. Nanoparticle Diffusion Measures Bulk Clot Permeability. *Biophys J*. 2011 Aug 17;101(4):943–50.
306. Iverson E, Griswold K, Song D, Gagliardi TB, Hamidzadeh K, Kesimer M, et al. Membrane-Tethered Mucin 1 is Stimulated by Interferon in Multiple Cell Types and Antagonizes Influenza A Virus Infection in Human Airway Epithelium. *bioRxiv*. 2021 Mar 11;2021.03.11.434997.
307. Kato K, Lillehoj EP, Park YS, Umehara T, Hoffman NE, Madesh M, et al. Membrane-Tethered MUC1 Mucin Is Phosphorylated by Epidermal Growth Factor Receptor in Airway Epithelial Cells and Associates with TLR5 To Inhibit Recruitment of MyD88. *The Journal of Immunology*. 2012 Feb 15;188(4):2014–22.
308. Singh PK, Wen Y, Swanson BJ, Shanmugam K, Kazlauskas A, Cerny RL, et al. Platelet-Derived Growth Factor Receptor β -Mediated Phosphorylation of MUC1 Enhances Invasiveness in Pancreatic Adenocarcinoma Cells. *Cancer Res*. 2007 Jun 1;67(11):5201–10.
309. Dhar P, Ng GZ, Dunne EM, Sutton P. Mucin 1 protects against severe *Streptococcus pneumoniae* infection. *Virulence*. 2017 Jul 13;8(8):1631–42.
310. Nguyen Y, Procario MC, Ashley SL, O'Neal WK, Pickles RJ, Weinberg JB. Limited effects of Muc1 deficiency on mouse adenovirus type 1 respiratory infection. *Virus Research*. 2011 Sep;160(1–2):351–9.

311. Arcasoy SM, Latoche J, Gondor M, Watkins SC, Henderson RA, Hughey R, et al. MUC1 and Other Sialoglycoconjugates Inhibit Adenovirus-mediated Gene Transfer to Epithelial Cells. *Am J Respir Cell Mol Biol*. 1997 Oct 1;17(4):422–35.
312. Costa NR. Relevance of MUC1 mucin variable number of tandem repeats polymorphism in H pylori adhesion to gastric epithelial cells. *World Journal of Gastroenterology*. 2008;14(9):1411.
313. Li X, Bleumink-Pluym NMC, Luijckx YMCA, Wubbolts RW, Putten JPM van, Strijbis K. MUC1 is a receptor for the Salmonella SiiE adhesin that enables apical invasion into enterocytes. *PLOS Pathogens*. 2019 Feb 4;15(2):e1007566.
314. Saeland E, de Jong MAWP, Nabatov AA, Kalay H, Geijtenbeek TBH, van Kooyk Y. MUC1 in human milk blocks transmission of human immunodeficiency virus from dendritic cells to T cells. *Molecular Immunology*. 2009 Jul 1;46(11):2309–16.
315. Li Y, Dinwiddie DL, Harrod KS, Jiang Y, Kim KC. Anti-inflammatory effect of MUC1 during respiratory syncytial virus infection of lung epithelial cells in vitro. *Am J Physiol Lung Cell Mol Physiol*. 2010 Apr;298(4):L558–63.
316. Dhar P, McAuley J. The Role of the Cell Surface Mucin MUC1 as a Barrier to Infection and Regulator of Inflammation. *Front Cell Infect Microbiol*. 2019 Apr 24;9:117.
317. Lagow EL, Carson DD. Synergistic stimulation of MUC1 expression in normal breast epithelia and breast cancer cells by interferon- γ and tumor necrosis factor- α . *Journal of Cellular Biochemistry*. 2002;86(4):759–72.
318. Koga T, Kuwahara I, Lillehoj EP, Lu W, Miyata T, Isohama Y, et al. TNF- α induces MUC1 gene transcription in lung epithelial cells: its signaling pathway and biological implication. *American Journal of Physiology-Lung Cellular and Molecular Physiology*. 2007 Sep 1;293(3):L693–701.
319. Lloren KKS, Lee T, Kwon JJ, Song MS. Molecular Markers for Interspecies Transmission of Avian Influenza Viruses in Mammalian Hosts. *Int J Mol Sci*. 2017 Dec 13;18(12).
320. Lakadamyali M, Rust MJ, Zhuang X. Endocytosis of influenza viruses. *Microbes and Infection*. 2004 Aug;6(10):929–36.
321. McAuley JL, Corcilius L, Tan HX, Payne RJ, McGuckin MA, Brown LE. The cell surface mucin MUC1 limits the severity of influenza A virus infection. *Mucosal Immunology*. 2017 Nov;10(6):1581–93.
322. Kesimer M, Scull M, Brighton B, DeMaria G, Burns K, O'Neal W, et al. Characterization of exosome-like vesicles released from human tracheobronchial ciliated epithelium: a possible role in innate defense. *The FASEB Journal*. 2009 Jun 1;23(6):1858–68.

323. Kato K, Uchino R, Lillehoj EP, Knox K, Lin Y, Kim KC. Membrane-Tethered MUC1 Mucin Counter-Regulates the Phagocytic Activity of Macrophages. *Am J Respir Cell Mol Biol*. 2015 Sep 22;54(4):515–23.
324. Shirasaki H, Kanaizumi E, Watanabe K, Konno N, Sato J, Narita S ichirou, et al. Tumor Necrosis Factor Increases MUC1 mRNA in Cultured Human Nasal Epithelial Cells. *Acta Oto-Laryngologica*. 2003 Apr 1;123(4):524–31.
325. Konowalchuk JD, Agrawal B. MUC1 mucin is expressed on human T-regulatory cells: Function in both co-stimulation and co-inhibition. *Cellular Immunology*. 2012 Jan 1;272(2):193–9.
326. Wykes M, MacDonald KPA, Tran M, Quin RJ, Xing PX, Gendler SJ, et al. MUC1 epithelial mucin (CD227) is expressed by activated dendritic cells. *Journal of Leukocyte Biology*. 2002;72(4):692–701.
327. Leong CF, Raudhawati O, Cheong SK, Sivagengei K, Hamidah HN. Epithelial membrane antigen (EMA) or MUC1 expression in monocytes and monoblasts. *Pathology*. 2003 Oct 1;35(5):422–7.
328. Tumpey TM, García-Sastre A, Taubenberger JK, Palese P, Swayne DE, Pantin-Jackwood MJ, et al. Pathogenicity of Influenza Viruses with Genes from the 1918 Pandemic Virus: Functional Roles of Alveolar Macrophages and Neutrophils in Limiting Virus Replication and Mortality in Mice. *J Virol*. 2005 Dec 15;79(23):14933–44.
329. McGill J, Heusel JW, Legge KL. Innate immune control and regulation of influenza virus infections. *J Leukoc Biol*. 2009 Oct;86(4):803–12.
330. Komuro I, Keicho N, Iwamoto A, Akagawa KS. Human alveolar macrophages and granulocyte-macrophage colony-stimulating factor-induced monocyte-derived macrophages are resistant to H₂O₂ via their high basal and inducible levels of catalase activity. *J Biol Chem*. 2001 Jun 29;276(26):24360–4.
331. Lescoat A, Ballerie A, Augagneur Y, Morzadec C, Vernhet L, Fardel O, et al. Distinct Properties of Human M-CSF and GM-CSF Monocyte-Derived Macrophages to Simulate Pathological Lung Conditions In Vitro: Application to Systemic and Inflammatory Disorders with Pulmonary Involvement. *Int J Mol Sci*. 2018 Mar 17;19(3).
332. Winkler AR, Nocka KH, Sulahian TH, Kobzik L, Williams CMM. In Vitro Modeling of Human Alveolar Macrophage Smoke Exposure: Enhanced Inflammation and Impaired Function. *Experimental Lung Research*. 2008 Jan 1;34(9):599–629.
333. Thompson CI, Barclay WS, Zambon MC, Pickles RJ. Infection of Human Airway Epithelium by Human and Avian Strains of Influenza A Virus. *Journal of Virology*. 2006 Aug 15;80(16):8060–8.
334. Conant D, Hsiao T, Rossi N, Oki J, Maures T, Waite K, et al. Inference of CRISPR Edits from Sanger Trace Data. *CRISPR J*. 2022 Feb;5(1):123–30.

335. Kato K, Lillehoj EP, Lu W, Kim KC. MUC1: The First Respiratory Mucin with an Anti-Inflammatory Function. *J Clin Med*. 2017 Nov 29;6(12).
336. Kato K, Lillehoj EP, Kim KC. MUC1 Regulates Epithelial Inflammation and Apoptosis by PolyI:C through Inhibition of Toll/IL-1 Receptor-Domain-Containing Adapter-Inducing IFN- β (TRIF) Recruitment to Toll-like Receptor 3. *Am J Respir Cell Mol Biol*. 2014 Apr 2;51(3):446–54.
337. Zhang H, Ji J, Liu Q, Xu S. MUC1 downregulation promotes TNF- α -induced necroptosis in human bronchial epithelial cells via regulation of the RIPK1/RIPK3 pathway. *J Cell Physiol*. 2019 Jan 21;
338. Nath S, Mukherjee P. Muc1: a multifaceted oncoprotein with a key role in cancer progression. *Trends Mol Med*. 2014 Jun;20(6):332–42.
339. Kim KC, Wasano K, Niles RM, Schuster JE, Stone PJ, Brody JS. Human neutrophil elastase releases cell surface mucins from primary cultures of hamster tracheal epithelial cells. *Proceedings of the National Academy of Sciences*. 1987 Dec 1;84(24):9304–8.
340. Mahanta S, Fessler SP, Park J, Bamdad C. A minimal fragment of MUC1 mediates growth of cancer cells. *PLoS One*. 2008 Apr 30;3(4):e2054.
341. Read SA, Wijaya R, Ramezani-Moghadam M, Tay E, Schibeci S, Liddle C, et al. Macrophage Coordination of the Interferon Lambda Immune Response. *Front Immunol*. 2019 Nov 19;10:2674.
342. Liu BS, Janssen HLA, Boonstra A. IL-29 and IFN α differ in their ability to modulate IL-12 production by TLR-activated human macrophages and exhibit differential regulation of the IFN γ receptor expression. *Blood*. 2011 Feb 24;117(8):2385–95.
343. Hillyer P, Mane VP, Schramm LM, Puig M, Verthelyi D, Chen A, et al. Expression profiles of human interferon-alpha and interferon-lambda subtypes are ligand- and cell-dependent. *Immunol Cell Biol*. 2012 Sep;90(8):774–83.
344. Altschuler Y, Kinlough CL, Poland PA, Bruns JB, Apodaca G, Weisz OA, et al. Clathrin-mediated Endocytosis of MUC1 Is Modulated by Its Glycosylation State. *MBoC*. 2000 Mar 1;11(3):819–31.
345. Dou D, Hernández-Neuta I, Wang H, Östbye H, Qian X, Thiele S, et al. Analysis of IAV Replication and Co-infection Dynamics by a Versatile RNA Viral Genome Labeling Method. *Cell Reports*. 2017 Jul 5;20(1):251–63.
346. Delaveris CS, Webster ER, Banik SM, Boxer SG, Bertozzi CR. Membrane-tethered mucin-like polypeptides sterically inhibit binding and slow fusion kinetics of influenza A virus. *Proc Natl Acad Sci USA*. 2020 Jun 9;117(23):12643–50.
347. Li K, Cao P, McCaw JM. Modelling the Effect of MUC1 on Influenza Virus Infection Kinetics and Macrophage Dynamics. *Viruses*. 2021 May;13(5):850.

348. Wu NC, Thompson AJ, Xie J, Lin CW, Nycholat CM, Zhu X, et al. A complex epistatic network limits the mutational reversibility in the influenza hemagglutinin receptor-binding site. *Nat Commun*. 2018 Mar 28;9(1):1264.
349. Gambaryan AS, Balish A, Klimov AI, Tuzikov AB, Chinarev AA, Pazynina GV, et al. Changes in the Receptor-Binding Properties of H3N2 Viruses during Long-Term Circulation in Humans. *Biochemistry Moscow*. 2019 Oct;84(10):1177–85.
350. Lozano R, Naghavi M, Foreman K, Lim S, Shibuya K, Aboyans V, et al. Global and regional mortality from 235 causes of death for 20 age groups in 1990 and 2010: a systematic analysis for the Global Burden of Disease Study 2010. *The Lancet*. 2012 Dec 15;380(9859):2095–128.
351. Williams BG, Gouws E, Boschi-Pinto C, Bryce J, Dye C. Estimates of world-wide distribution of child deaths from acute respiratory infections. *The Lancet Infectious Diseases*. 2002 Jan 1;2(1):25–32.
352. Iyer S, Yadav R, Agarwal S, Tripathi S, Agarwal R. Bioengineering Strategies for Developing Vaccines against Respiratory Viral Diseases. *Clinical Microbiology Reviews*. 2021;35(1):e00123-21.
353. Broadbent AJ, Boonnak K, Subbarao K. Respiratory Virus Vaccines. *Mucosal Immunology*. 2015;1129–70.
354. Clercq ED, Li G. Approved Antiviral Drugs over the Past 50 Years. *Clinical Microbiology Reviews*. 2016;29(3):53.
355. Sheahan TP, Sims AC, Zhou S, Graham RL, Pruijssers AJ, Agostini ML, et al. An orally bioavailable broad-spectrum antiviral inhibits SARS-CoV-2 in human airway epithelial cell cultures and multiple coronaviruses in mice. *Science Translational Medicine*. 2020 Apr 29;12(541):eabb5883.
356. Bennett AL, Smith DW, Cummins MJ, Jacoby PA, Cummins JM, Beilharz MW. Low-dose oral interferon alpha as prophylaxis against viral respiratory illness: a double-blind, parallel controlled trial during an influenza pandemic year. *Influenza Other Respir Viruses*. 2013 Sep;7(5):854–62.
357. Mesev EV, LeDesma RA, Ploss A. Decoding type I and III interferon signalling during viral infection. *Nat Microbiol*. 2019 Jun;4(6):914–24.
358. Schreiber G. The Role of Type I Interferons in the Pathogenesis and Treatment of COVID-19. *Front Immunol*. 2020 Sep 30;11:595739.
359. Park A, Iwasaki A. Type I and Type III Interferons - Induction, Signaling, Evasion, and Application to Combat COVID-19. *Cell Host Microbe*. 2020 Jun 10;27(6):870–8.
360. Lazear HM, Schoggins JW, Diamond MS. Shared and Distinct Functions of Type I and Type III Interferons. *Immunity*. 2019 Apr 16;50(4):907–23.
361. Schaap-Nutt A, Liesman R, Bartlett EJ, Scull MA, Collins PL, Pickles RJ, et al. Human parainfluenza virus serotypes differ in their kinetics of replication and

- cytokine secretion in human tracheobronchial airway epithelium. *Virology*. 2012 Nov 25;433(2):320–8.
362. Monk PD, Marsden RJ, Tear VJ, Brookes J, Batten TN, Mankowski M, et al. Safety and efficacy of inhaled nebulised interferon beta-1a (SNG001) for treatment of SARS-CoV-2 infection: a randomised, double-blind, placebo-controlled, phase 2 trial. *The Lancet Respiratory Medicine*. 2021 Feb 1;9(2):196–206.
363. Ciencewicky JM, Brighton LE, Jaspers I. Localization of Type I Interferon Receptor Limits Interferon-Induced TLR3 in Epithelial Cells. *J Interferon Cytokine Res*. 2009 May;29(5):289–97.
364. Heaton NS, Langlois RA, Sachs D, Lim JK, Palese P, tenOever BR. Long-term survival of influenza virus infected club cells drives immunopathology. *J Exp Med*. 2014 Aug 25;211(9):1707–14.
365. Dumm RE, Fiege JK, Waring BM, Kuo CT, Langlois RA, Heaton NS. Non-lytic clearance of influenza B virus from infected cells preserves epithelial barrier function. *Nature Communications*. 2019 Feb 15;10(1):779.
366. Pezzulo AA, Starner TD, Scheetz TE, Traver GL, Tilley AE, Harvey BG, et al. The air-liquid interface and use of primary cell cultures are important to recapitulate the transcriptional profile of in vivo airway epithelia. *American Journal of Physiology Lung Cellular and Molecular Physiology*. 2011 Jan;300(1):L25-31.
367. Lokugamage KG, Hage A, de Vries M, Valero-Jimenez AM, Schindewolf C, Dittmann M, et al. Type I Interferon Susceptibility Distinguishes SARS-CoV-2 from SARS-CoV. *Journal of Virology*. 94(23):e01410-20.
368. Ziegler CGK, Allon SJ, Nyquist SK, Mbanjo IM, Miao VN, Tzouanas CN, et al. SARS-CoV-2 Receptor ACE2 Is an Interferon-Stimulated Gene in Human Airway Epithelial Cells and Is Detected in Specific Cell Subsets across Tissues. *Cell*. 2020 May;181(5):1016-1035.e19.
369. Yu M, Wang J, Yang Y, Zhu C, Su Q, Guo S, et al. Rotation-Facilitated Rapid Transport of Nanorods in Mucosal Tissues. *Nano Lett*. 2016 Nov 9;16(11):7176–82.
370. Choi J, Cargnello M, Murray CB, Clarke N, Winey KI, Composto RJ. Fast Nanorod Diffusion through Entangled Polymer Melts. *ACS Macro Letters*. 2015 Sep 15;4(9):952–6.